Theoretical and Experimental Study of Low-Finesse Extrinsic Fabry-Perot Interferometric Fiber Optic Sensors

Ming Han

Dissertation submitted to the committee members of Ming Han
in partial fulfillment of the requirements for the degree of

Doctor of Philosophy
in
Electrical and Computer Engineering

Dr. Anbo Wang, Chair
Dr. Ira Jacobs
Dr. Roger H. Stolen
Dr. William H. Tranter
Dr. Guy Indebetouw

May, 2006
Blacksburg, Virginia

Keywords: Fiber Optics, Fiber Optic Sensors, Fabry-Perot, White-light Interferometry

Theoretical and Experimental Study of Low-Finesse Extrinsic Fabry-Perot Interferometric Fiber Optic Sensors

Ming Han

(ABSTRACT)

In this dissertation, detailed and systematic theoretical and experimental study of low-finesse extrinsic Fabry-Perot interferometric (EFPI) fiber optic sensors together with their signal processing methods for white-light systems are presented. The work aims to provide a better understanding of the operational principle of EFPI fiber optic sensors, and is useful and important in the design, optimization, fabrication and application of single mode fiber(SMF) EFPI (SMF-EFPI) and multimode fiber (MMF) EFPI (MMF-EFPI) sensor systems. The cases for SMF-EFPI and MMF-EFPI sensors are separately considered.

In the analysis of SMF-EFPI sensors, the light transmitted in the fiber is approximated by a Gaussian beam and the obtained spectral transfer function of the sensors includes an extra phase shift due to the light coupling in the fiber end-face. This extra phase shift has not been addressed by previous researchers and is of great importance for high accuracy and high resolution signal processing of white-light SMF-EFPI systems. Fringe visibility degradation due to gap-length increase and sensor imperfections is studied. The results indicate that the fringe visibility of a SMF-EFPI sensor is relatively insensitive to the gap-length change and sensor imperfections.

Based on the spectral fringe pattern predicated by the theory of SMF-EFPI sensors, a novel curve fitting signal processing method (Type 1 curve-fitting method) is presented for white-light SMF-EFPI sensor systems. Other spectral domain signal processing methods including the wavelength-tracking, the Type 2-3 curve fitting, Fourier transform, and two-point interrogation methods are reviewed and systematically analyzed. Experiments were carried out to compare the performances of these signal processing methods. The results have shown that the Type 1 curve fitting method achieves high accuracy, high resolution, large dynamic range, and the capability of absolute measurement at the same time, while others either have less resolution, or are not capable of absolute measurement.

Previous mathematical models for MMF-EFPI sensors are all based on geometric optics; therefore their applications have many limitations. In this dissertation, a modal theory is developed that can be used in any situations and is more accurate. The mathematical description of the spectral fringes of MMF-EFPI sensors is obtained by the modal theory. Effect on the fringe visibility of system parameters, including the sensor head structure, the fiber parameters, and the mode power distribution in the MMF of the MMF-EFPI sensors, is analyzed. Experiments were carried out to validate the theory. Fundamental mechanism that causes the degradation of the fringe visibility in MMF-EFPI sensors are revealed. It is shown that, in some situations at which the fringe visibility is important and difficult to achieve, a simple method of launching the light into the MMF-EFPI sensor system from the output of a SMF could be used to improve the fringe visibility and to ease the fabrication difficulties of MMF-EFPI sensors.

Signal processing methods that are well-understood in white-light SMF-EFPI sensor systems may exhibit new aspects when they are applied to white-light MMF-EFPI sensor systems. This dissertation reveals that the variations of mode power distribution (MPD) in the MMF could cause phase variations of the spectral fringes from a MMF-EFPI sensor and introduce measurement errors for a signal processing method in which the phase information is used. This MPD effect on the wavelength-tracking method in white-light MMF-EFPI sensors is theoretically analyzed. The fringe phases changes caused by MPD variations were experimentally observed and thus the MFD effect is validated.

To my wonderful family

for the amazing support you have always provided

Acknowledgments

I would first like to to express my deepest gratitude to my adviser, Dr. Anbo Wang, for his continuous guidance, support, trust, and encouragement throughout my study and research at Virginia Tech. Not only has his influence been critical to my development as a research scientist, but he has afforded me other wonderful opportunities to grow in the areas of communication, administration, and leadership. I thank him for being the most influential person in my professional life. I also thank him for being a wonderful professor, mentor, role model, and friend.

I would also like to thank the other committee members, Dr. Jacobs, Dr. Stolen, Dr. Indebetouw, and Dr. Tranter for their help throughout this project.

I would like to thank the group members, past and present, that I have worked with during my stay at Center for Photonics Technology (CPT). I would like to give special thanks to Yizheng Zhu for his help, and most importantly, for the friendship of more than 13 years. Thanks also go to Yongxin Wang, Bo Dong, Xiaopei Chen, Xingwei Wang and Daewoong Kim for your tremendous contributions in many projects we have worked on together. I would like to thank Dr. Juncheng Xu and Dr. Yan Zhang for many good trips we have shared in the past. I also want to thank Dr. Wei Peng and Dr. Bing Yu for their aid both in and outside work.

A big thank you goes to Debbie Collins and other staff members at CPT who make our life easier on a daily basis. I would also like to thank Dr. Gary Pickrell, Dr. Kristie Cooper, and Dr. Ting-Chung Poon for their aid in my research.

I would like to extend my acknowledgment to all of my friends in Blacksburg, many of whom are also my colleagues at CPT. They were always available and ready to help when I needed it. Specially, I would like to thank Jian Fang, Kun Liu, Dr. Chao Shang, Dr. Yihua Zhang, and Dr. Zhanming Qin for their help. I also like to thank the wonderful couples of Glenn & Becky, Johnny & Nancy, and Vern & Rebecca for many things I have learned from every one of you, from language to culture.

Finally, I would like to thank my family for their support throughout this process and in very other endeavor for which I have partaken. I would like to show my sincerest gratitude to my parents, Lianzuo Han & Shuying Fang. My brother and I have been very fortunate to grow up in a family like the one we have, and I only hope I can provide similarly for my children. I want to say thank you to my brother, Dong Han, for the support he has provided to our family in China. I am deeply grateful to my wife, Yan Xi, for her great patience, encouragement, and dedication, for being the most important person in my life, and for being a wonderful mother of our lovely daughter, Stephanie.

Contents

List of Figures

List of Tables

Chapter 1

Introduction

1.1 Research background

The past three decades have seen a great deal of progress in the fiber optic sensor technology. A fiber optic sensor may be defined as a means through which the physical, chemical or biological parameters being measured interact with light in or guided by a fiber to produce signals that are related to the parameters [1]. The optical fiber could be the sensing element through which the interaction happens. In this case, the sensors are referred to "intrinsic" fiber optic sensors. On the other hand, the optical fiber could simply function only as a transmission medium that guides the light to (and/or back from) the interaction region which is outside the fiber. The sensors of this kind are referred to "extrinsic" fiber optic sensors. Through the 1980s to present time, numerous fiber optic sensors that are capable of measuring a wide variety of measurands have emerged from laboratories worldwide. Many of them have been successfully transformed to commercial devices during the past 10 years. The driving force behind this work is the many advantages of fiber optic sensors over their electronic counterpart, such as the immunity to electromagnetic interference (EMI), small size, light weight, high measurement accuracy and resolution, resistance to harsh environments, and capability of high capacity multiplexing.

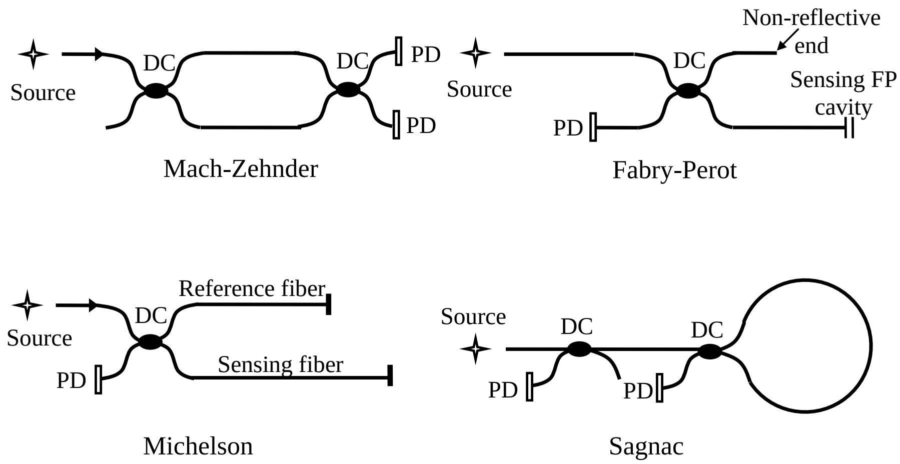

Figure 1.1: Several configurations of Fiber optic interferometers. DC, directional coupler; PD, photodetector.

Among the fiber optic sensors, interferometer has become widely accepted as the configuration which can provide the ultimate sensitivity to a range of weak physical fields. These sensors usually employ an interferometer as the sensing element through which two beams or multi-beams of light interfere with each other to form spectral or intensity fringe patterns. The phase of the fringe patterns is directly related to the parameters being measured. Almost all configurations of the conventional interferometers, such as Mach-Zehnder, Sagnac, Michelson and Fabry-Perot (FP) interferometers, shown in Figure 1.1, have found their applications in fiber optic sensors [2] [3]. Among them, FP interferometer (FPI) has drawn a great deal of research interest because the FPI-based fiber optic sensors provide many operational benefits compared to other configurations. For example, a serious issue in the implementation of Mach-Zehnder and Michelson interferometers is the polarization-induced fading (PIF) in low-birefringence fiber interferometers which was first identified as early as 1980 by Stowe *et al.* [4]. This problem is rooted in the fact that as the light is split into two separate paths in Michelson and Mach-Zehnder configurations, the evolution of the state of polarization (SOP) of light guided in these fibers varies independently in a random and unpredictable manner. Consequently, the SOPs of the recombined optical components from the two interferometer arms vary independently, and this leads to a reduction of the interferometric optical mixing efficiency and a loss (“fading”) of the interference signal [5]. Sagnac interferometer is not immune to this problem either because SOP of light evolves differently as the light propagating in different directions in a Sagnac interferometer, although along the same fiber. However, this problem usually is not present in FPI-based fiber optic sensors in which the FP cavities where the light interference occurs consist either of optical components with very short length in which the SOP variations are negligible, or simply of air (vacuum) in which there is no polarization effect. Another advantage of the FPI-based fiber optic sensors is their small size. Different from the other three sensor interferometric configurations in which one of the whole arms functions as the sensing element, a FPI-based fiber optic sensor uses the FP cavity as the sensing element which could be made very small, so it can provide a much better spatial measurement resolution and is capable of point measurement. Moreover, multimode fibers (MMFs) could be implemented in an extrinsic-FPI (EFPI) fiber optic sensors in which the light is guided to and back from the FP cavity through a MMF, A MMF-based fiber sensor system could be much less costly than a SMF-based system because MMF imposes less stringent constraints to the light source and optical components that are compatible to MMFs (such as MMF connectors and MMF couplers) usually requires less fabrication accuracy and control and consequently are potentially cheaper. This cost-efficiency is very important for the commercialization and wide spread use of fiber optic sensors considering that they have to compete with many other well-established and less-costly measurement approaches in the market. However, the implementation of MMF in other three interferometric configurations is difficult because the optical-path-length (OPL) experienced by different modes in the MMF is different and is difficult to predict. Therefore depending on their OPL difference, lights belonging to the same mode group but from two different paths interfere either constructively or destructively when they combine, which causes a significant reduction of the interference signal.

The early work on the FPI-based fiber optic sensors includes introducing “internal” mirrors in a SMF to form intrinsic FPI (IFPI) sensors by splicing two SMFs with one metal-coated at the fiber end [6]. However, one of the most widely reported FPI-based sensors has been the EFPI fiber optic sensors developed at Virginia Polytechnic Institute and State University [7]. In one of their most popular forms, the sensors are simply fabricated by inserting two fibers into an alignment tube to form a FP cavity, with one as the lead-in/out fiber to carry the light and the other as the sensing fiber. The fiber ends are cleaved to function as the reflectors of the FP cavity. Various types of EFPI fiber optic sensors have been designed and implemented in the measurement of a variety of measurands, such as temperature [8], pressure [9] [10], strain [11][12], magnetic field [13], flow [14], acoustic waves [15], and chemical and biological parameters [16][17].

In spite of the recent significant progress in EFPI fiber sensors, this technology is far from being mature and in many cases, our understanding of sensor operational mechanisms is still not adequate. This is true especially for MMF-EFPI sensors which have received only few research efforts. Even for SMF-EFPI sensors, some issues in the signal processing remain to be resolved. Theoretical analysis is always important in the development of an EFPI fiber optic sensor system, because it not only is a powerful tool in the design and optimization of the system, but also provides a solid base for the development of signal processing methods. Most of the EFPI sensors either under research at laboratories or commercialized in industry are SMF-based. Consequently, theoretical works on EFPI sensors focus most on these sensors, or more specifically, on the fringe visibility of these sensors. Fringe visibility is one of the most important parameters that characterize the performance of an EFPI sensor, because it largely determines the ultimate signal-to-noise ration(SNR) of the system. The light transmitted in the SMF is often modeled as a point source [18], or more accurately, as a Gaussian beam [19]. However, in these models, the predicated spectral pattern is not accurate.

As mentioned above, most EFPI fiber optic sensors that are currently commercially available or under research are SMF-based in spite of the great potential cost efficiency of the MMF-EFPI sensor systems. The fabrication difficulty might be partially responsible for the unpopularity of MMF-EFPI sensors. Generally speaking, it is much more difficult to fabricate a MMF-EFPI sensor with decent fringe visibility than a SMF-EFPI sensor.

Previously available analysis is based on geometric optics and has revealed that the stringent requirement on the gap-length and FP cavity thickness variations may be responsible for the fabrication difficulty of a MMF-EFPI sensor [20]. In this analysis, the output of the propagation modes in a multimode fiber is modeled as incoherent rays outputting the fiber end-face with different angles. The geometric-optics is an approximate method to describe the light propagation and interference and is adequate only when the fiber characteristic dimension is much larger than the optical wavelength. This condition may not be satisfied for strongly guiding fibers, in which the refractive index difference between the core and cladding is large, such as a sapphire fiber, or for MMFs with only a few modes; Moreover geometric-optics theory is not capable of predicting the exact fringe pattern of a MMF-EFPI sensor system from the fiber specifications, sensor structures, and system operation conditions, therefore signal processing with both high-accuracy and absolute measurement is difficult for a white-light MMF-EFPI sensor system.

EFPI fiber optic sensor systems can also be classified as intensity-based in which a laser is used as the light source [21], and white-light based in which, as its name suggests, a white-light (low-coherence) source is used. White-light EFPI sensors have many advantages over their intensity-based counterpart, such as the possibility of absolute measurements, a significant reduction in the noise level, an insensitivity to optical power fluctuations, the possibility of multiplexing a large number of sensors in a measuring system, and ultra-high measurement resolution. However, it is a challenging task to simultaneously achieve the absolute measurement and ultra-high resolution in the same system. Absolute measurement is easily achieved by calculating the spectral fringe period, either directly [24] from the spectrum, or at the domain of its Fourier Transform [35], because the gap-length is unambiguously determined by the spectral fringe period, and vice versa, from the simple relationship

$$d = \lambda_1 \lambda_2 / 2(\lambda_1 - \lambda_2), \tag{1.1}$$

where d is the gap-length, and λ_1 and λ_2 are the wavelengths of two neighboring fringe peaks or valleys. Ultra-high resolution measurement could be achieved by methods such as wavelength-tracking [36], however these methods are usually not capable of absolute measurement and the operation range is limited to $\pm\lambda/2$ because of the ambiguity of the output from the sensor system. Qi [37] *et al.* proposed a method that was intended to combine these two methods together and achieve both absolute measurement and high measurement resolution in a same system. In this method, the gap-length of the sensor was determined by finding the exact fringe peak integer number K of a particular spectral fringe peak. However, we have found that K obtained by the reported algorithm is not necessarily an integer in practice; and the rounding process could induce a measurement error of half the optical wavelength. For example, a half-wavelength "jump" of the gap-length measurement could occur during the measurement of an essentially unchanged gap-length cavity.

Nearly all the work on signal processing of white-light EFPI fiber optic sensor systems are demonstrated on SMF-EFPI sensor systems. Although a few signal processing methods have been directly carried over to white-light MMF-EFPI sensor systems [22] [23], their performance might be significantly different from the one in SMF-EFPI sensor systems. Moreover, many are not valid any more for MMF-EFPI sensor systems owing to some new aspects of the spectral pattern that are unique to MMF-EFPI sensors. The signal processing of white-light MMF-EFPI sensor systems is basically an untouched research area.

1.2 Scope of the dissertation

From the discussion in Section 1.1, it is clear that, in spite of the great progress recently made in EFPI sensor technology, many problems still remain unresolved. Therefore, it is the goal of this dissertation to present a detailed and systematic analysis on EFPI fiber optic sensors that could provide a better understanding of the fundamental principles of the sensor operation and lead to solutions to many problems we have been facing.

The rest of the dissertation is constructed as follows: In Chapter 2, a more accurate theoretical analysis of SMF-EFPI sensor is presented. The coupling-induced phase shift of the output spectral fringes is predicted. Chapter 3 deals with the spectral domain signal processing of white-light SMF-EFPI sensors. In this chapter, currently available spectral signal processing methods are reviewed and analyzed. A new signal processing method is developed and its performance is experimentally compared with other signal processing methods. Chapter 4 deals with the theoretical analysis of MMF-EFPI sensors. A modal theory based on Maxwell's equations is presented. The fringe visibility of MMF-EFPI sensors is analyzed and the fundamental mechanisms that determine the sensor's fringe visibility are revealed. In Chapter 5, it is shown that the mode power distribution (MPD) variations in the MMF could cause phase changes of the spectral fringes from a MMF-EFPI sensor. This MPD effect is theoretically analyzed and experimentally verified. Finally a summary of the dissertation and recommendations of future works are given in Chapter 6.

Chapter 2

Low-finesse SMF-EFPI sensors

As discussed in Chapter 1, most EFPI fiber optic sensors under research or available in industry are SMF-based. Besides all the advantages of fiber optic sensors, SMF-EFPI sensors also possess other advantages such as ease of fabrication, high resolution and compatibility with many components used in the well-established optical fiber communications. The analysis on the fringe visibility of a SMF-EFPI sensor is important because it is helpful in the design, optimization and fabrication of such a sensor. Moreover, the analysis on the fringe pattern output from a SMF-EFPI sensor system in the frequency domain is essential for signal processing of a white-light SMF-EFPI sensor system which can achieve high-accuracy, high resolution, and absolute measurement at the same time. Previous theoretical work is still not adequate to accurately predict the fringe pattern. In this chapter, first the analysis of SMF-EFPI sensors is reviewed in Section 2.1. Then a more accurate analysis is presented in Section 2.2. The obtained fringe pattern includes the coupling-induced phase-shift which has not been previously addressed and is of great importance in the signal processing of a white-light SMF-EFPI sensor system. In Section 2.3, the fringe visibility of a SMF-EFPI sensor is analyzed with the consideration of an imperfect sensor head. Finally, conclusions are given in Section 2.4.

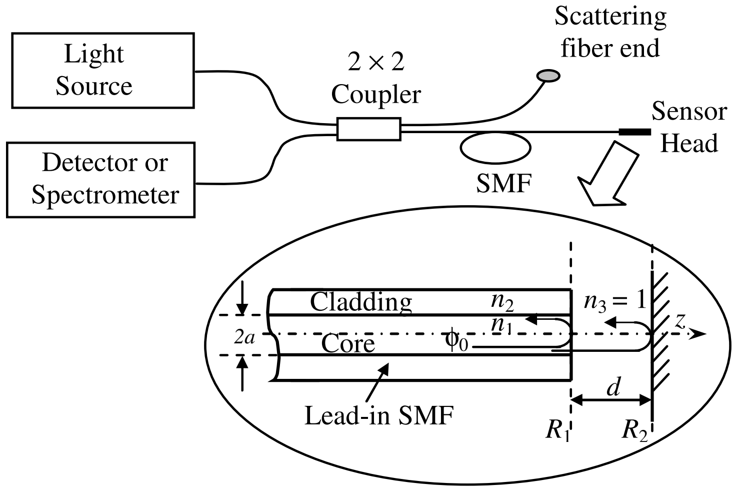

Figure 2.1: Schematic of a SMF-EFPI sensor system. Inset, schematic of a SMF-EFPI sensor head.

2.1 Review of low-finesse SMF-EFPI theory

A typical SMF-EFPI sensor configuration is shown in Figure 2.1. Light from a light source propagates along a lead-in/out SMF to the sensor head which is a FP cavity formed by the end-faces of the lead-in/out and the target fibers. A fraction of this incident light is reflected at the output end-face of the lead-in/out fiber and returns directly back to the fiber. The light transmitted out of the lead-in/out fiber projects onto the fiber end-face of the target fiber. This reflected light from the target fiber is partially recoupled into the lead-in/out fiber. Interference between the two reflections then gives rise to the interferometric output of the sensor. Although the reflection from the air-glass interface of the lead-in/out fiber is independent of the gap length between the two fibers, the intensity contributed by the reflection from the target fiber is strongly dependent on the gap-length, which causes the fringe contrast (fringe visibility) of the sensor output to decrease with an increase in the gap length.

A simple analysis was presented by Murphy *et al* [18]. In his analysis, the two beams received by the lead-in/out fiber from the reflection of the air-glass interfaces of lead-in/out and target fibers were approximated by two plane waves E_1 and E_2 respectively, and their electrical fields are given by

$$E_i = A_i \exp(j\phi_i), \ (i = 1, 2). \tag{2.1}$$

Assuming the amplitude of the light field E_1 reflected from the lead-in/out fiber end-face is $A_1 = A$, then the amplitude of the light field E_2 which is reflected by the target fiber end-face can be simplified to

$$A_2 = A \left\{ \frac{ta}{a_2 d \tan[\sin^{-1}(\mathtt{NA})]} \right\}, \tag{2.2}$$

where a is the fiber core radius, t is the transmission coefficient of the air-glass interface (≈ 0.98), d is the end separation, and $\mathtt{NA}$ is the numerical aperture of the SMF fiber, given by $\mathtt{NA} = (n_1^2 - n_2^2)^{1/2}$. n_1 and n_2 are the refractive indices of the core and the cladding of the lead-in/out fiber, respectively. The intensity of the interferometric light in the input/output fiber is given by

$$\begin{aligned} I &= |E_1 + E_2|^2 \\ &= A_1^2 + A_2^2 + 2A_1A_2\cos(\phi_1 - \phi_2), \end{aligned} \tag{2.3}$$

which can be rewritten as

$$I = A^2 \left(1 + \frac{2ta}{a + 2d \tan[\sin^{-1}(\mathtt{NA})]} \cos\left(\frac{4\pi d}{\lambda}\right) + \left\{ \frac{ta}{2d \tan[\sin^{-1}(\mathtt{NA})]} \right\}^2 \right), \tag{2.4}$$

where $\phi_1 = 0$ and $\phi_2 = 2d(2\pi/\lambda)$ have been assumed and λ is the wavelength of operation in free space.

Arya, *et al*, performed a more accurate analysis in which the light propagating in the SMF was approximated as a Gaussian beam [19],

$$E_1 = A \exp(-r^2/\omega_0^2) \exp(-j\beta z), \tag{2.5}$$

where ω_0 is the mode field diameter and r and z are cylindrical coordinates. The electrical field at any point P outside the lead-in/out fiber end-face and reflected from the target fiber

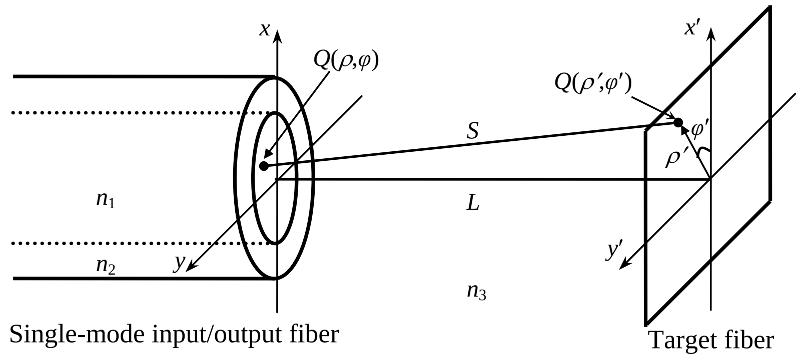

Figure 2.2: Coordinate system for the analysis. L: gap length.

is given by the Kirchhoff diffraction formalism [25],

$$E(P) = \frac{1}{4\pi} \int \int \left[E_1 \frac{\partial}{\partial z} \left(\frac{\exp(jkS)}{S} \right) - \frac{\exp(jkS)}{S} \frac{\partial E_1}{\partial z} \right] ds. \tag{2.6}$$

In the above equation, $k = 2\pi/\lambda$ is the free-space propagation constant, and the integral is evaluated over the lead-in/out fiber end-face region. The factor S is the vector distance between a point Q at the lead-in/out fiber end-face and the point P, as shown in Fig. 2.2. Using Eq. (2.5), Eq. (2.6) can be simplified to

$$E(P) = \frac{1}{4\pi} \int \int E_1 \left(\frac{\exp(jkS)}{S} \right) \left[\frac{2L}{S} \left(jk - \frac{1}{S} \right) + jk \right] ds. \tag{2.7}$$

where L is the gap-length of FP cavity. The electrical field contributed by the reflection from the target fiber is then given by

$$E_2 = E_1 \frac{\int \int E(P) E_1 ds}{\left[\int \int E(P) E^*(P) ds \right]^{1/2} \left[\int \int E_1 E_1^* ds \right]^{1/2}} \tag{2.8}$$

Once E_1 and E_2 are obtained, Arya used Eq. (2.3) to model the spectral fringes output from the SMF-EFPI sensor.

Compared to the analysis by Murphy, the calculation of the electrical field contributed by the reflection of the target fiber is more accurate in the analysis by Arya. However, in both analysis, the phase shift between E_1 and E_2 has been assumed to be $\phi_2 - \phi_2 = 4\pi d/\lambda$, which was assumed to be only dependent on the gap-length of the FP cavity and the wavelength of the light source. However, from Eq. (2.8), a phase-shift could occur when the electrical field reflected from the target fiber is coupled back to the lead-in/out fiber because the integral in Eq. (2.8) is not necessarily a real number. Moreover, both analysis have assumed a perfect fiber sensor head, with the all fiber end faces parallel to each other and perpendicular to the fiber axis. In practice, this is not the case owing to the limited fabrication accuracy. And fringe visibility degradation caused by the sensor imperfections has not been analyzed.

2.2 Modal analysis of SMF-EFPI sensors

The schematic of the SMF-EFPI sensor used in our analysis is the same as shown in Figure (2.1). Our analysis starts from the Gaussian beam approximation of light propagating in a SMF. It is well known that for a weakly guiding, step-index, circular-core optical SMF, the scalar field of the fundamental LP_{01} mode may be assumed to be approximately Gaussian in shape given in Eq. (2.5) with an error of only a few percent. With this assumption, the complex envelope of the field that emanates from the lead-in/out fiber and is reflected back to the lead-in/out fiber end-face R_1 after propagating a length of $2d$ in the free space inside the FP cavity may be expressed as [26]

$$E_2' = A(jk\omega_0^2/2q)\exp(-jkr^2/2q), \tag{2.9}$$

where $q = 2d + jk\omega_0^2/2$ is the q parameter of the Gaussian beam. In Eq. (2.9), the phase shift of $\exp(-jk2d) = \exp(-j4\pi d/\lambda)$ which is simply related to the distance of $2d$ the light beam has traveled is omitted. Note that we have assumed that the zero point of the z axis is on the fiber endface ($z = 0$ in Eq. 2.5 when the light is emitted from the fiber endface). Strictly, Eq. (2.9) is only valid for $2d >> \lambda$, which is satisfied by most practical SMF-EFPI sensors in which the gap-length d is at least tens of micrometers. Eq. (2.9) indicates that beam maintains its Gaussian shape and the diameter of the mode field spreads as it propagates in the free-space, as show in Figure 2.3, in which the mode profile of a standard SMF and after it propagates a distance of $2d$ in free space are plotted. Eq. (2.9) also shows that

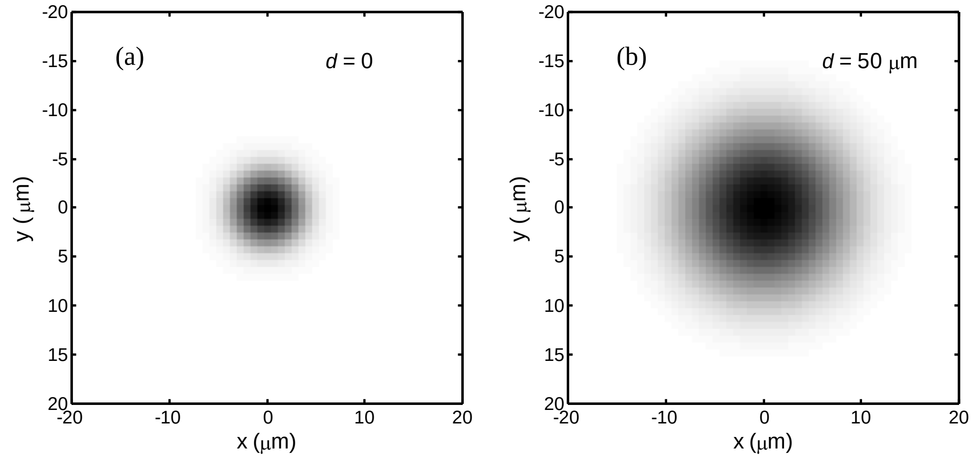

Figure 2.3: The mode intensity distribution, E_1, of a standard SMF, (a); and E_2' for gap-length d, (b).

free-space propagation also causes an extra phase shift to the field in addition to the omitted phase-shift of $-4\pi d/\lambda$. Furthermore, the phase plane is deformed by free-space propagation as the phase shift is also a function of the radius r. Field E_2' is then coupled to E_2, which may be expressed as

$$\begin{aligned} E_2 &= \eta E_2' \exp(-jk2d - j\pi) \\ &= |\eta| E_2' \exp(-j4\pi d/\lambda - j\pi + j\theta), \end{aligned} \tag{2.10}$$

where η is the mode-coupling coefficient from E_2' to E_2, which one may obtain by performing the overlap integral of E_2 and E_2' over surface R_1 (Ref. [30]):

$$\eta = |\eta| \exp(j\theta) = \frac{\int\int E_1^* E_2' ds}{\left(\int\int E_1^* E_1 ds \int\int E_2'^* E_2' ds\right)^{1/2}}. \tag{2.11}$$

Substituting Eqs. (2.5) and (2.9) into Eq. (2.11) gives the analytical result

$$\eta = \frac{k\omega_0^4 (k\omega_0^2 + j4d)}{8d^2 + k^2\omega_0^4}. \tag{2.12}$$

Therefore the amplitude and the phase of the mode-coupling coefficient are given by

$$|\eta| = k\omega_0^4 (k^2\omega_0^4 + 16d^2)^{1/2} / (8d^2 + k^2\omega_0^4) \tag{2.13}$$

and

$$\theta = \arctan(4d/k\omega_0^2), \tag{2.14}$$

respectively. In Eq. (2.10), the phase-shift π arises from the reflection at R_2 of light incident from a medium that is optically less dense to a medium that is optically denser and phase shift θ arises from the light coupling from E_2' to E_2 at surface R_1 as E_2' has extra phase-shift and phase-plane deformations from the free space propagation. Note that θ is dependent on the wavelength, mode field radius, and gap-length of the FP cavity. For a fixed fiber, mode field radius can be determined by wavelength of operation, and θ is only dependent on the wavelength and the gap-length of FP cavity. Therefore the interference signal can be expressed as

$$\begin{aligned} I'(\lambda, d) &= (E_1 + E_2)(E_1 + E_2)^* \\ &= |A^2| \left[1 + |\eta| \exp(-j4\pi d/\lambda - j\pi + j\theta)\right] \\ &\quad \times \left[1 + |\eta| \exp(j4\pi d/\lambda + j\pi - j\theta)\right] \\ &= I_0(\lambda) R\{1 + |\eta| \cos[4\pi d/\lambda + \pi - \theta(\lambda, d)]\}, \end{aligned} \tag{2.15}$$

where $I_0(\lambda)$ is the light source's power spectrum, which is assumed to be known, and R is a constant associated with the transmission loss of the fiber and reflection loss at the two fiber ends. The spectrum is then normalized by $I_0(\lambda)$ and the result is (the constant R is dropped)

$$I(\lambda, d) = 1 + |\eta| \cos[4\pi d/\lambda + \pi - \theta(\lambda, d)]. \tag{2.16}$$

Eq. (2.16) reveals that the phasor of the interferometric signal could be influenced not only by the light propagation length in free space, but also by the light coupling from free space back to lead-in/out fiber. Figure 2.4 shows the calculated coupling-induced phase shift θ as a function of gap-length d for a standard SMF (Corning SMF-28) with $a = 4.5$ μm, $n_1 = 1.448$, and $n_2 = 1.444$ at wavelength $\lambda = 1550$ nm. The phase shift θ increases from 0 to 0.358π when the gap-length is changed from 0 to 100 μm. For comparison, the free-space transmission induced phase-shift ($4\pi d/\lambda$) is also included in Figure 2.4. Although the phase shift owing to light coupling ($\theta(\lambda, d)$) is usually much smaller than the phase shift owing to

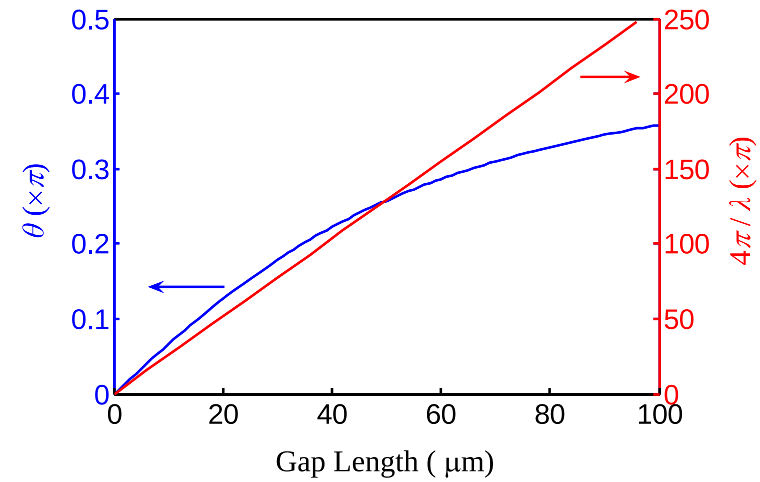

Figure 2.4: Calculated coupling phase shift θ and free-space propagation phase shift $4\pi d/\lambda$ as a function of gap-length d.

free space transmission ($4\pi d/\lambda$) for a sensor with gap-lengths of tens of micrometers, phase shift $\theta(\lambda, d)$ is of great importance in the high accuracy and high resolution signal processing of a white-light low-finesse SMF-EFPI sensor system and can not be simply ignored. The applicaton of this coupling-induced phase shift in the signal processing of white-light SMF-EFPI sensor systems will be investigated in Chapter 3.

So far, all the analysis has assumed a perfect fiber sensor head. As discussed in Section 2.1, this is not the case in practice. Imperfections such as uneven fiber end-faces, unparallelism between two reflection surfaces of the FP cavity and tilt angles between the fiber end-faces and fiber axis could always happen during the fiber cleaving and other fabrication processes of SMF-EFPI sensors. Especially when a fabrication process includes laser fusion [22] in which good controls of the outcome from laser heating are difficult. Fibers inside the sensor head could be significantly deformed owing to the extremely high temperature, which could introduce most of the imperfections of the fabricated sensor. Among all these imperfections, the unparallelism between two fiber end-faces perhaps has the most significant influence on the fringe visibility of the sensor. In this case, the cavity geometry therefore becomes that of a wedge, introducing variations in the cavity thickness of the inter-

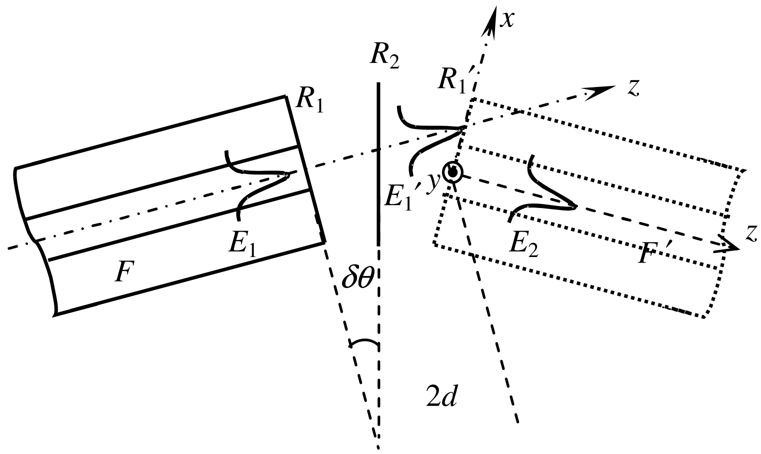

Figure 2.5: Illustration of a SMF-EFPI with a wedge between the two reflection surfaces R_1 and R_2. Fiber F is the mirror image of fiber F' with respect to surface plane R_2.

ferometer. In the analysis, it is assumed that the reflection surface plane R_1 is perpendicular to the fiber axis z, while reflection surface R_2 is tilted from its original position, forming a wedge angle of $\delta\theta$ with respect to R_1, as shown in Fig. 2.5. The effect of the angular and lateral misalignment between the lead-in/out fiber F and its mirror image fiber F' caused by the wedge must be considered when Eq. (2.11) is used to calculate the mode coupling coefficient η. The effect of the wedge is to produce a linear phase change across the beam [27] and a spatial displacement between fields E_1 and E_2' at the coupling plane R_1'. For two fibers that are misaligned by a wedge angle of $\delta\theta$, the field E_2' becomes

$$E_{2,\Delta\alpha}{}' = E_2'\left(x - 2d\tan(\theta)\right)\exp[jkx\tan(2\delta\theta)] \tag{2.17}$$

at the coupling surface R_1'. Therefore mode coupling coefficient η is obtained by substituting Eq. (2.17) into Eq. (2.11) and the interferometric signal can be obtained with the help of Eq. (2.16).

2.3 Fringe visibility of a SMF-EFPI sensor

In this section, Eq. (2.16) is used to analyze the fringe visibility of a SMF-EFPI sensor. In the analysis, the standard Corning SMF-28 is chosen as the lead-in/out fiber. The parameters of such a fiber are as following: $a = 4.5$ μm, $n_1 = 1.448$, and $n_2 = 1.444$ at wavelength $\lambda = 1550$ nm. The effects of FP cavity gap-lengths and the wedge angles between the two fiber end-faces on the fringe visibility are considered separately in the following subsections.

2.3.1 Definition of fringe visibility

Fringe visibility (also called fringe contrast) of an EFPI sensor is defined by

$$V_b = (I_{max} - I_{min})/(I_{max} + I_{min}), \tag{2.18}$$

where I_{max} and I_{min} are the maximum and minimum spectral intensities in the spectral fringes from the EFPI sensor. In practice, the visibility can be measured by two distinctive ways depending on the light source used. In a white-light EFPI sensor system, the spectral fringes can be directly measured in the wavelength domain by a spectrometer and the maximum and minimum spectral intensity are readily found. In the laser-based EFPI sensor systems, the light wavelength is fixed and the fringes are a function of the gap-length. The visibility has to be measured by slightly tuning the gap-length of the FP cavity and observing the maximum and minimum output. From Eq. (2.16), both measurements give the same fringe visibility of

$$V_b = |\eta| \tag{2.19}$$

provided that the slight dependence of $|\eta|$ on wavelength $|\lambda|$ is negligible.

2.3.2 Fringe visibility vs. gap-length

Figure 2.6 shows the fringe visibility as a function of gap-length of the above SMF-EFPI sensor at different wedge angles. For all the wedge angles, the fringe visibility decreases as

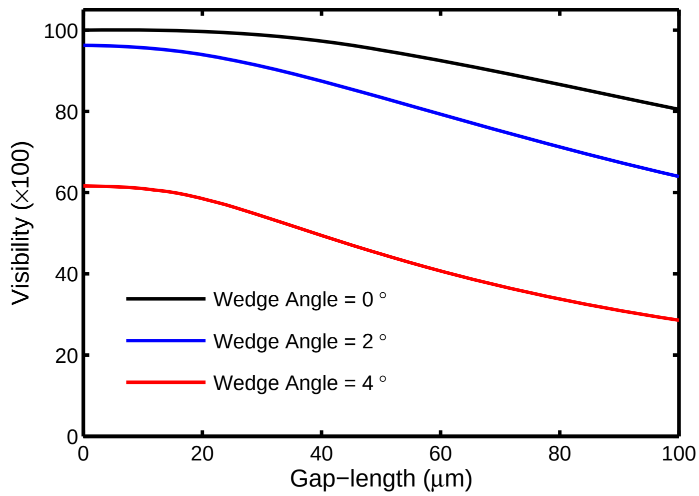

Figure 2.6: Visibility as a function of gap-length for a SMF-EFPI sensor.

the gap-length increases. When the gap-length increases from 0 to 100 μm, the visibility drops by 20% (from 100% to around 80%) for a perfect sensor (wedge angle = 0), 32.3%(from 96.3% to 64.0%) for a sensor with wedge angle = 2°, and 33.1% (from 61.7% to 28.6%) for sensor with wedge angle = 4°. Moreover, the fringe visibility decrease more quickly as the gap-length increases for a specific sensor. The fringe visilbity of a perfect sensor decreases from 100% to around 80% when the gap-length increases from 0 to 100 μm. However, its fringe visibility only drops by 2.8% (from 100% to 97.2%) when the gap-length increases from 0 to 40 μm. In practice, a SMF-EFPI sensor usually has a gap-length less than 100 μm. The visibility degradation owing to the gap-length is acceptable in most practical applications.

2.3.3 Fringe visibility vs. wedge angle

Figure 2.7 shows the fringe visibility as a function of the wedge angle for a SMF-EFPI sensor with different gap-lengths. The wedge angle is changed from 0 up to 5°. As expected, the fringe visibility decreases as the wedge angle increases. It is also seen that the fringe visibility decreases more quickly as the wedge angle becomes larger. For a sensor with a gap-length

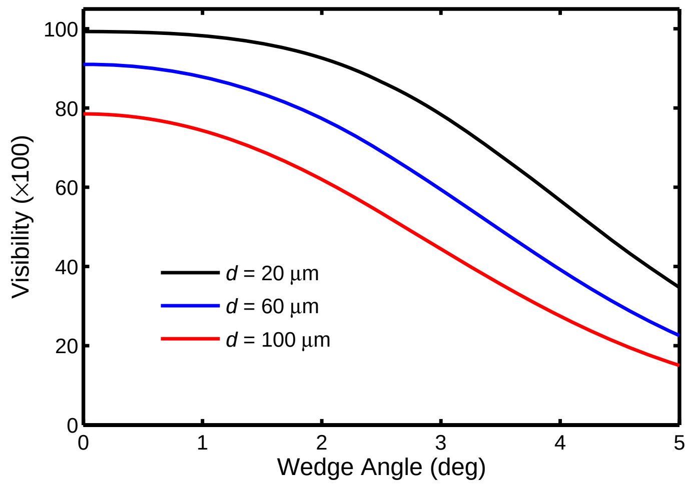

Figure 2.7: Visibility as a function of gap-length for a SMF-EFPI sensor.

of 20 μm, the fringe visibility still maintains better than 90% for wedge angles as large as 2°. The fringe visibility variation as a function of the wedge angle shows similar trend for all gap-lengths used in the analysis, which indicates that effect of the wedge angle is of little dependence on the gap-length of the sensor. In practice, the fiber end-faces functioning as the reflectors of a SMF-EFPI sensor are usually obained by cleaving the fiber using a fiber cleaver. A comercially available high-precision fiber cleaver is usually capable of achiving an average end angle better than 1°. Therefor the fringe visibility degradation owing to this small wedge angle is of no concern in most of the pratical applications. However, when laser-fusion is involved in the fabrication of the SMF-EFPI sensor, in many cases the high power laser light is applied only to a small area of the sensor head, which could introduce large temperature gradient on the fiber. Significant random deformations to the fiber could occur and large wedge angles that could significantly decrease the fringe visibility might be formed. In this case, special care must to taken during the application of the laser light in order to obtain a sensor with an acceptable fringe visibility.

2.4 Conclusions

A modal theory is presented for SMF-EFPI sensors, in which the mode supported by the fiber is assumed to have a Gaussian profile. Our analysis shows that the spectral fringe from a SMF-EFPI sensor contains an extral phase shift introduced as the light reflected from the second surface of the FP cavity is coupled into the lead-in/out fiber. This extra-phase shift has not been addressed by previous research.

Based on the modal theory, the fringe visibility variations as a function of the gap-length of the FP cavity are analyzed. The sensitivity of fringe visibility to the wedge angles between the two reflection surfaces of the FP cavity, which is one of the most common imperfections of a FP sensor, is also analyzed. The results show that, in general, the fringe visibility of a SMF-EFPI sensor is not sensitive to the gap-lengths and the wedge angles of the sensor.

Chapter 3

Signal processing for white-light SMF-EFPI sensor systems

3.1 Motivation

As described in Chapter 1, the possibility of absolute measurement and high measurement resolution are two main advantages of white-light EFPI sensor systems. It is also known that many efforts have been made trying to achieve these two advantages in the same system, however, with few success. The challenge actually lies in the limited number of spectral fringes available in the obtained fringes, which is limited by the bandwidth of the white-light source. A low-finesse white-light SMF-EFPI sensor system is shown in Figure 3.1 (The inset shows the enlarged view of the sensor head). The system configuration is similar to that shown in Figure 2.1 except that a white light source and a spectrometer are specified as the light source and the detector. The spectral fringes as a function of wave number ($1/\lambda$) for a SMF-EFPI sensor with gap-length $d = 30$ μm is shown in Figure 3.2. Assuming the bandwidth of the light source is 60 nm (1520−1580nm), the corresponding wave number range (gray area) only covers a small portion of its absolute wave number value. In order to achieve high resolution, high accuracy, absolute measurement, and large linear range at

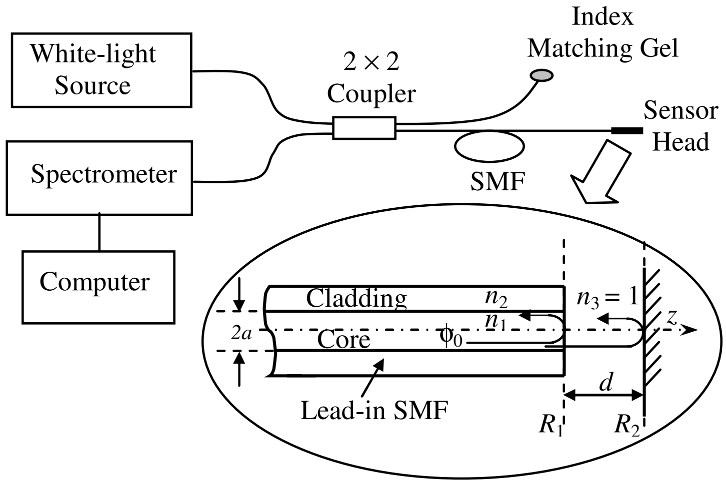

Figure 3.1: Schematic of a white-light SMF-EFPI sensor system. Inset, schematic of a SMF-EFPI sensor head.

the same time, the system must have a very good signal-to-noise ratio (SNR). Most of the spectrometers used in white-light sensor systems are charge-coupled device (CCD)-based, because they are usually compact and low-cost, and thus can provide convenient measurement of the spectrum from a white-light sensor system. However, the resolution (on the order of 1 nm) and accuracy of these CCD-based spectrometers are still too low to generate the desired SNR of the fringes. Fortunately, with the technology advances in narrow-linewidth scanning lasers and absolute wavelength calibration, spectrometers with extremely high resolution and accuracy are becoming available in today's market, which makes the goal of achieving high resolution, high accuracy, absolute measurement, and large linear range measurement at the same time possible. Curve fitting method has been shown to be successful in unambiguously determining the gap-length without sacrificing the high measurement resolution in an interferometric profilometer [38], in which available wave number was also limited. The light in the profilometer propagates through bulk materials as plane waves; Therefore the spectral fringe pattern is well-defined by the cosine function of $\cos(4\pi/\lambda + \pi)$. However, this method can not be directly transferred to a white-light SMF-EFPI sensor system owing to the extra coupling-induced phase-shift which is a function of gap-length. Without the

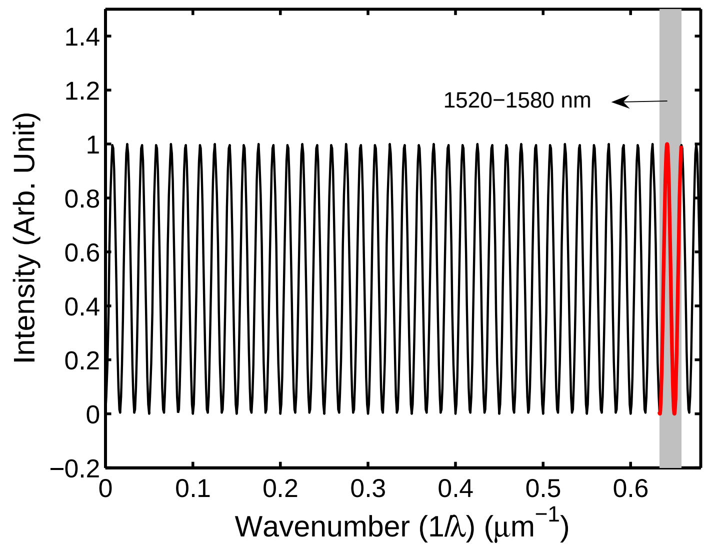

Figure 3.2: Fringe pattern from a white-light SMF-EFPI sensor system.

knowledge of the phasor of the spectral fringe pattern, the simultaneous high resolution and absolute measurement is difficult.

In this chapter,the currently available spectral domain signal processing methods for white-light SMF-EFPI sensor systems are analyzed. Based on the modal theory presented in Section 2.2 which is able to accurately predict the spectral fringe pattern of SMF-EFPI sensor systems, a signal processing method characterized by improved accuracy, ultra-high measurement resolution, and absolute measurement is reported. The performance of this novel signal processing method is compared with all other methods through experimental results. The rest of the chapter is constructed as follows: In Section 3.2, Some spectral domain signal processing methods are introduced and analyzed; The detail of the novel algorithm is presented in Section 3.3 together with the other two similar methods. Section 3.4 present the experimental verification of the proposed algorithm and comparisons of different methods. Finally some comments and conclusions are given in Section 3.5.

3.2 Signal processing in spectral domain

In this section, the signal processing methods of two-point interrogation, peak wavelength-tracking, and Fourier transform are reviewed and analyzed. As discussed in Section 2.2, the spectral fringes after normalization by the spectrum of light source is given by Eq. (2.16), which is rewritten here:

$$I(\lambda, d) = 1 + |\eta| \cos[4\pi d/\lambda + \pi - \theta(d)]. \tag{3.1}$$

All the spectral-domain signal processing methods are based on Eq. (3.1), which relates the spectral fringes from a spectrometer to the gap-length of the SMF-EFPI sensor.

3.2.1 Wavelength-tracking method

In this method, the wavelength shift of one fringe peak (or valley) caused by the gap-length variations is employed to detect the small gap-length perturbation induced by the measured parameters [36]. For example, assuming the wavelength λ_m is a peak point in the interference spectrum that satisfies

$$4\pi d/\lambda_m + \pi - \theta(d) = 2m\pi, \tag{3.2}$$

where m is a nonnegative integer denoting the order number of the chosen fringe peak, the gap-length is then readily obtained by

$$d = [m/2 - 1/4 + \theta(d)/4\pi]\lambda_m. \tag{3.3}$$

The relative error of the gap-length determined by Eq. (3.3) is

$$|\Delta d/d| = |\Delta\lambda_m/\lambda_m|, \tag{3.4}$$

where $\Delta\lambda_m$ is the error of the peak position. The resolution of this demodulation is high. However it is not capable of absolute measurement. Note that the absolute value of d can not be determined by this method because the order number m is unknown. Thus calibration is required every time a sensor system is switched on. Furthermore, the measurement range is also limited as the gap-length variations must be small enough so that the tracked peak is located inside the wavelength window throughout the measurement. These two disadvantages have greatly limited the usefulness of this method.

3.2.2 Two-point interrogation

Another straightforward way to extract the gap-length from fringes described by Eq. (3.1) is to use two special points in the fringes. Suppose λ_1 and λ_2 ($\lambda_1 > \lambda_2$) are the wavelengths of two adjacent peak points in the interferometric spectrum, and their interference orders are m and $m+1$. From Eq. (3.1), λ_1 and λ_2 satisfies

$$4\pi d/\lambda_1 + \pi - \theta(d) = 2m\pi \tag{3.5}$$

and

$$4\pi d/\lambda_2 + \pi - \theta(d) = 2(m+1)\pi, \tag{3.6}$$

respectively. The unknown integer of m can be canceled out by subtracting Eq. (3.5) from Eq. (3.6), and the gap-length d is then given by

$$d = \lambda_1\lambda_2/2(\lambda_1 - \lambda_2). \tag{3.7}$$

Obviously, this method is simple, is capable of absolute measurement, and has a large linear range. However, the resolution and accuracy are rather limited owing to the fact that the difference between the two wavelengths in the denominator of Eq. (3.7) is much smaller than the the wavelengths in the numerator. Thus a small error in the determination of λ_1 and λ_2 causes a large error of gap-length d. For example, Eq. (3.7) gives the relative error of gap-length d caused by the error in determining wavelength λ_1 as

$$|\Delta d/d| = \sqrt{2}|\lambda_2/(\lambda_1 - \lambda_2)||\Delta\lambda_1/\lambda_1|. \tag{3.8}$$

Comparing Eq. (3.4), the relative error is enlarged by a factor of $\sqrt{2}|\lambda_2/(\lambda_1 - \lambda_2)|$. Using illustrative, yet typical numbers of $\lambda_1 = 1520$ and $\lambda_1 = 1580$, the factor is 36.

3.2.3 Fourier tranform method

Replacing wavelength λ in Eq. (3.1) with wave number k which is defined by $k = 1/\lambda$ and using a rectangular function to model the limited measurement range of the spectrometer, Eq. (3.1) can be written as a more general form of

$$I(k,d) = \{a + \cos\left[4\pi kd + \pi - \theta(d)\right]\}\Pi\left(\frac{k-k_0}{k_b}\right). \tag{3.9}$$

where a represents the direct current (DC) component of the signal, k_0 and k_b are the central wave number and the available wave number range, respectively, and $\Pi((k-k_0)/k_b)$ is the rectangle function defined as

$$\Pi\left(\frac{k-k_0}{k_b}\right) = \begin{cases} 1, & |k-k_0| \leq k_b/2 \\ 0, & |k-k_0| > k_b/2 \end{cases} \tag{3.10}$$

Eq. (3.9) shows that the spectral fringe from a SMF-EFPI sensor is a truncated cosine function of wave number k. The period of the cosine function is determined by gap-length d, which can be obtained by finding the peak position at its Fourier transform domain [35]. Obviously, the measurement of this so-called "Fourier transform method" is absolute and has a large linear range. In addition, one might expect that high measurement resolution and accuracy can be obtained considering that this method makes use of all data points obtained by the spectrometer. However, it is found that the measurement accuracy is significantly reduced by the rectangle function, especially in the cases that the gap-lengths of the FP cavity are small. Define the Fourier transform of Eq. (3.10) as

$$\Pi_{FFT}(q) = \frac{1}{2\pi}\int \Pi\left(\frac{k-k_0}{k_b}\right)\exp(-j2\pi qk)dk \tag{3.11}$$

Then the Fourier transform of Eq. (3.9) is given by

$$\begin{aligned} I_{FFT}(q) &= \frac{1}{2\pi}\int I(k,d)\exp(-j2\pi qk)dk \\ &= a\Pi_{FFT}(q) - \frac{1}{2}\Pi_{FFT}(q-2d)\exp[-j\theta(d)] \\ &\quad -\frac{1}{2}\Pi_{FFT}(q+2d)\exp[j\theta(d)]. \end{aligned} \tag{3.12}$$

The right side of Eq. (3.12) comprises of three terms. The first term is related to the DC component of the fringe signal; The second and third terms are related to the cosine function in Eq. (3.9) and have their peaks at $q = 2d$ and $q = -2d$, respectively. However, the peak positions of the total Fourier spectrum described by Eq. (3.12) might deviate from $q = 2d$ and $q = -2d$ owing to the interactions among the sidelobes of these three components. This deviation may in turn cause the measurement error of gap-lengths obtained by the peak position of the Fourier spectrum. In practice, the DC component can be removed before doing the Fourier transform, so that $a = 0$ and the sidelobe effect could be reduced. Furthermore, by increasing the "frequency" of the fringe in the measurement range, the sidelobe effect could also be reduced as the three components move away from each other in the Fourier transform domain. However the measurement accuracy is still rather limited because gap-lengths of practical SMF-EFPI sensors are at most several hundred micrometers to retain a useful fringe visibility which are still too small to sufficiently suppress the sidelobe effect.

The accuracy limitations owing to the sidelobe effect are studied through computer simulations. In the simulations, the fringes are noise-free cosine waves and the wavelength range is from 1520 to 1570 nm, which is the typical measurement range of currently available scanning-laser-based spectrometers. The measurement error, $d_{FT} - d$, where d_{FT} and d are the measured and true values of the gap-lengths, respectively, as a function of d is shown in Figure 3.3(a). The gap-lengths vary from 50 to 180 μm, which covers the gap-lengths of most practical SMF-EFPI sensors. The simulation results show that the measured gap-length oscillate rapidly around the true value. Since the cosine wave used here is noise-free, the errors are solely caused by the sidelobes of the Fourier spectrum of the rectangle function. Figure 3.3(b) shows the detail of the oscillation structure at the gap-length range between 60 and 64 μm in Figure 3.3(b). As expected, the envelop of the oscillations decreases as the gap-length increases. However the measurement error is not tolerable in most applications even at large gap-lengths. For example, the peak-to-peak variation of the measurement error at $d = 180$ μm can be as large as 1 μm. By using other window functions which have larger

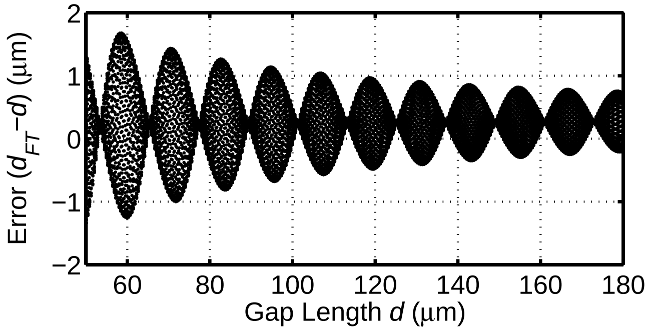

(a)

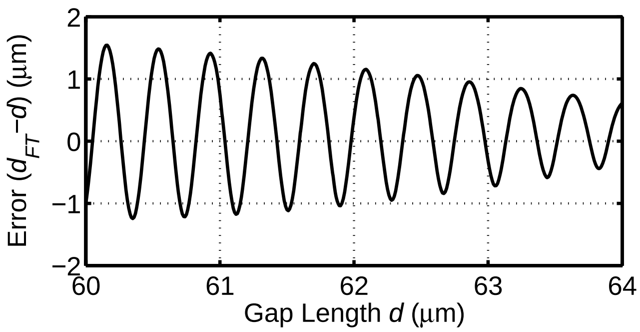

(b)

Figure 3.3: (a): The gap-length measurement error using Fourier transform method, and (b), an enlarged view of (a) in the gap-length span of $60-64$ μm.

sidelobe extinction ratios in the signal processing, for example, the Hanning window, the measurement error might be reduced, however it is expected that the reduction is only to a limited degree.

3.3 Curve fitting method

As the output of the white-light SMF-EFPI sensor system is a cosine function of wave number, the period of the cosine wave which is determined by the gap-length, can be obtained by finding the period of a cosine wave that best fits the measured fringes. Actually this method has been studied in interferometric profilometers and other interferometric sensors to achieve absolute distance measurement. However, the difficulty of this method arises from the fact that the cosine wave fitting process is sensitive to the SNR of the target fringes. Also, the envelop of the cosine wave is required to be highly uniform as the fringes cover only a few cycles. Otherwise, the cosine wave fitting process could converge to a wrong value of the period. In a white-light SMF-EFPI sensor system in which an LED and CCD-based spectrometer are used, owing to the limited measurement accuracy of the spectrometer, the SNR of the normalized fringes is usually not adequate for the curve-fitting method to be effective. As mentioned in Section 3.1, the scanning-laser based sensor interrogation system together with the absolute wavelength calibration capability has significantly improved the SNR of the sensor output signal and thus make the curve-fitting method more useful. In this section various fitting functions and a curve-fitting algorithm that can be used in the curve-fitting method are introduced.

3.3.1 Fitting functions

For convenience, Eq. (3.1) is modified to

$$I(\lambda, d) = c + h\cos[4\pi d/\lambda + \pi - \theta(d)]. \tag{3.13}$$

where c and h are two constants. From Eq. (3.13), the phasor of the fringe comprises three terms: the first term, $4\pi d/\lambda$, is the gap-length related phase shift; the second is the π phase-shift arising from the reflection at R_2; and the third term, $\theta(d)$ is the coupling-induced phase-shift. Figure 3.4 shows the calculated coupling-induced phase-shift $\theta(d)$ as a function of the gap-length d for a SMF with $a = 4.5$ μm, $n_1 = 1.448$, and $n_2 = 1.444$ at operation wavelength $\lambda = 1550$ nm. Sensor head imperfection of wedge angles between the two reflectors of the sensor is also considered. The phase shift increases from 0 to 0.358π when the gap-length is changed from 0 to 100 μm for a perfect sensor head (wedge angle = 0). As shown in Figure 3.4, wedge angles could, but only slightly, decrease the coupling-induced phase-shift. Provided that the spectrometer is calibrated, the obtained normalized fringe spectrum $I'(\lambda, d)$ as a function of wavelength λ is known. The gap-length d can be obtained

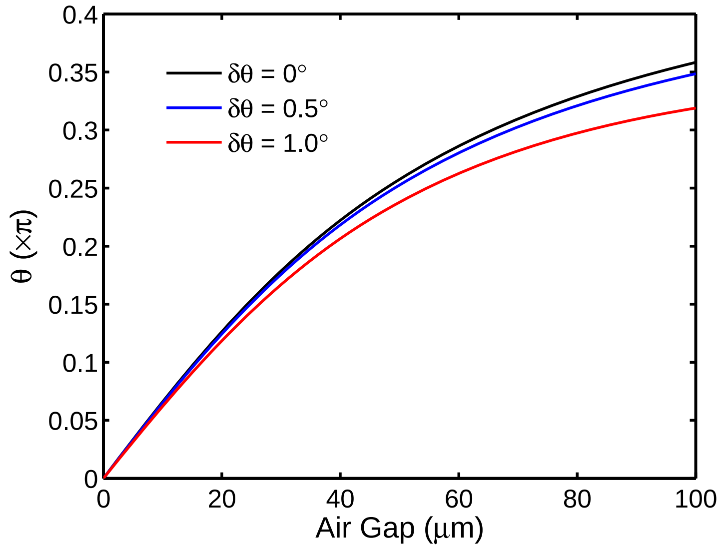

Figure 3.4: Coupling-induced phase-shift as a function of gap-length of the SMF-EFPI sensor.

by fitting Eq. (3.13) to the obtained $I'(\lambda, d)$ using fitting parameters c, h and d. However, in practice, the perturbations of environment and the fabrication process of a SMF-EFPI sensor could introduce bendings to the fiber, i.e., when the lead-in fiber is welded to the glass tube by thermal fusion [22]; and it is well known that the bending loss of a single mode fiber is a function of optical wavelength [39] [40]. Furthermore, the predicted coupling phase shift θ may slightly depart from its true value due to the imperfections of the sensor head (as shown in Figure 3.4) and the calculation errors. Instead of Eq. (3.13),

$$I = c + h\cos[4\pi d/\lambda + \pi - \theta(d)](b/\lambda + g). \tag{3.14}$$

is used as the fitting function, in which constants c, h, b, and g, and gap-length d are the fitting parameters. The linear function of wave number $1/\lambda$, $b/\lambda + g$, is used to model the bending losses of the fiber as a function of wave number. Furthermore, by adding the linear function in Eq. (3.15), the phase of the fitted curve can be adjusted to its theoretical result in the fitting process when the theoretical phase-shift is close to its true value. After straightforward algebra, Eq. (3.14) leads to

$$I = A\cos[4\pi d/\lambda + \pi - \theta(d)]/\lambda + B\cos[4\pi d/\lambda + \pi + \theta(d)] + C/\lambda + D, \tag{3.15}$$

Table 3.1: Tree types of curving-fitting methods

Type	Fitting Function	Fitting Parameters
1	$A\cos[4\pi d/\lambda+\pi-\theta(d)]/\lambda+D+$ $B\cos[4\pi d/\lambda+\pi-\theta(d)]+C/\lambda$	A, B, C, D, d
2	$A+B\cos(4\pi d/\lambda)+C\sin(4\pi d/\lambda)$	A, B, C, d
3	$A+B\cos(4\pi d/\lambda)+C\sin(4\pi d/\lambda)$ $+D\cos(8\pi d/\lambda)+E\sin(8\pi d/\lambda)$	A, B, C, D, E, d

where $A = bh$, $B = gh$, $C = cb$, and $D = cg$. In practice, Eq. (3.15) is used to fit the obtained $I_{norm}(\lambda, d)$. The curve-fitting method using fitting function of Eq. (3.15) is called the " Type 1" fitting method. For comparison, two other different fitting functions that do not take the knowledge of the coupling-induced phase-shift and do not include the linear modification to the fringe envelop are also used. The first is

$$I = A + B\cos(4\pi d/\lambda) + C\sin(4\pi d/\lambda), \tag{3.16}$$

in which A, B, C, and gap-length d are the fitting parameters. The second fitting function takes into account of the multi-reflections inside the FP cavity of the sensor by including the sine and cosine terms that are related to optical path length difference of $4d$, as shown in

$$I = A + B\cos(4\pi d/\lambda) + C\sin(4\pi d/\lambda) + D\cos(8\pi d/\lambda) + E\sin(8\pi d/\lambda), \tag{3.17}$$

in which A, B, C, D, E and air gap d are the fitting parameters. The curve-fitting methods using fitting functions of Eqs. (3.16) and (3.17) are referred to the "Type2" and "Type 3" curve-fitting methods, respectively. A summary of these three types of curve fitting methods is shown in Table (3.1).

3.3.2 Cosine wave fitting algorithm

Many algorithms are available and well investigated for least-square-error (LSE) fitting of cosine waves [41] [42] and algorithms have been standardized in IEEE Standard 1057 [43]. The fitting function used in these algorithms is Eq. (3.16), therefore they can be directly used for the " Type 2" curve-fitting method . However, these algorithms require modifications when applied to the " Type 1" and "Type 3" curve-fitting methods which use different fitting functions. In this subsection, the algorithm used here is illustrated by taking the " Type 3" curve-fitting method as an example.

Assume that the data recorded by a spectrometer from a white-light SMF-EFPI sensor system are normalized and contain the sequence of samples

$$I_1, \cdots, I_N \tag{3.18}$$

taken at wavelengths $\lambda_1, \cdots, \lambda_N$, respectively. It is further assumed that the data can be modeled by Eq. (3.17), so that

$$\begin{aligned} I_m &= A\cos[4\pi d/\lambda_m + \pi - \theta(d)]/\lambda_m + B\cos[4\pi d/\lambda_m + \pi - \theta(d)] \\ &\quad + C/\lambda_m + D, \qquad m = 1, \cdots, N. \end{aligned} \tag{3.19}$$

Before getting any further, the fitting process when d is known is first considered. Define the following vectors

$$\begin{aligned} \mathbf{x} &= (A, B, C, D)^T \\ \mathbf{I} &= (I_1, \cdots, I_N)^T, \end{aligned} \tag{3.20}$$

where T denotes the transpose. Then $\mathbf{I}$ obeys the linear set of equations

$$\mathbf{I} = \mathbf{Dx} \tag{3.21}$$

where $\mathbf{D}$ is a $N \times 4$ matrix expressed as

$$\mathbf{D} = \begin{pmatrix} \cos[4\pi d/\lambda_1 + \pi - \theta(d)]/\lambda_1 & \cos[4\pi d/\lambda_1 + \pi - \theta(d)] & 1/\lambda_1 & 1 \\ \cos[4\pi d/\lambda_2 + \pi - \theta(d)]/\lambda_2 & \cos[4\pi d/\lambda_2 + \pi - \theta(d)] & 1/\lambda_2 & 1 \\ \vdots & \vdots & \vdots & \vdots \\ \cos[4\pi d/\lambda_N + \pi - \theta(d)]/\lambda_N & \cos[4\pi d/\lambda_N + \pi - \theta(d)] & 1/\lambda_N & 1 \end{pmatrix} \tag{3.22}$$

Eq. (3.21) is an overdetermined set of linear equations when $N > 4$, with the LSE solution $\hat{\mathbf{x}}$ (in general, $\hat{}$ denotes an estimate) given by

$$\hat{\mathbf{x}} = (\mathbf{D}^T\mathbf{D})^{-\mathbf{1}}\mathbf{D}^T\mathbf{I}. \tag{3.23}$$

In reverse, the estimated fringes intensity, $\hat{\mathbf{I}}$, can be obtained by replacing $\mathbf{x}$ in Eq. (3.21) into $\hat{\mathbf{x}}$, so that

$$\hat{\mathbf{I}} = \mathbf{D}\hat{\mathbf{x}} \tag{3.24}$$

The final goal of the algorithm is to find the gap-length d that minimizes the sum squared estimated error S, which is defined by

$$S = \sum_{m=1}^{N}(I_m - \hat{I}_m)^2 = (\mathbf{I} - \mathbf{D}\hat{\mathbf{x}})^T(\mathbf{I} - \mathbf{D}\hat{\mathbf{x}}). \tag{3.25}$$

where $\hat{I}_m$ is the m^{th} element of vector $\hat{\mathbf{I}}$. The criterion of minimizing Eq. (3.25) is equivalent to finding the d that maximizes $s(d)$, which is defined as

$$s(d) = \mathbf{I}^T\mathbf{D}(\mathbf{D}^T\mathbf{D})^{-\mathbf{1}}\mathbf{D}^T\mathbf{I}. \tag{3.26}$$

A simple method to find gap-length d is through one-dimensional (1-D) grid search, in which $s(d)$ is calculated for a series of gap-lengths and the gap-length that gives the maximum value of $s(d)$ is picked as the fitting result. The process of this 1-D grid search method is presented in Table 3.2

Table 3.2: Least square fit by grid search

a)	gap-length grid $d_i, i = 1, \cdots, M$
b)	for $i = 1$ to M
c)	create $\mathbf{D}$ from d_i using Eq. (3.22)
d)	$s_i = \mathbf{I}^T\mathbf{D}(\mathbf{D}^T\mathbf{D})^{-\mathbf{1}}\mathbf{D}^T\mathbf{I}$
e)	end
f)	$d = d_k$, where $s_k = \max(s_i \vert i = 1, \cdots, M)$

3.4 Experimental Results

Experiments were carried out to test and compare the performance of the signal processing methods abovementioned. The spectral fringes were recorded by a high-accuracy and high resolution spectrometer for a range of gap-lengths. The signal processing methods of Type 1-3 curve-fitting, Fourier transform, two-point interrogation, and wavelength-tracking were implemented to derive the gap-lengths from the obtained spectral fringes. In this section, the experimental setup is first described. The measurement results obtained by Type 1 curve fitting method are then presented and are used to compare the results from other signal processing methods. The analysis of the signal processing methods focuses on their performances of measurement resolution and accuracy.

3.4.1 Experimental setup

The experimental setup to record the spectral fringes for a range of gap-lengths is the same as that shown in Figure 3.1 and the configuration of the optical sensor used in the setup is shown in Figure 3.5. The sensor was fabricated by inserting two 125 μm diameter Corning SMF-28 SMFs (the lead-in/out fiber and the target fiber) with cleaved ends into a hollow glass tube to which the target fiber was bonded with epoxy. The lead-in fiber was bonded

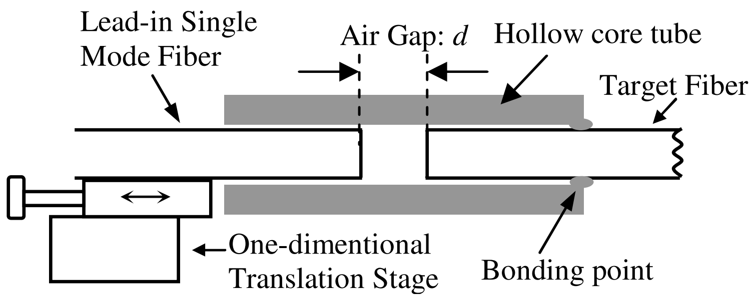

Figure 3.5: Construction of SMF-EFPI sensor used in the test.

to a 1-D translation stage by which the gap-length of the F-P cavity could be adjusted over a large spatial range. The hollow tube with inner diameter of 132 μm facilitated alignment of the two fiber tips and protected the FP cavity from environmental perturbations. A High Resolution Swept Laser Interrogator (HR-SLI) (V5.1, MicroOptics, Inc.) was used to function both as a white light source and as a spectrometer. HR-SLI is characterized by an ultra-high wavelength repeatability of 0.05 pm and an ultra-high wavelength accuracy of 1 pm. The spectral intensity was sampled from 1520 to 1570 nm with a total number of samples $N = 2000$ at an equal wavelength interval of 0.025 nm. During the measurement, the gap-length was increased approximately from 55.0 to 62.3 μm for 10 steps by manually adjusting the translation stage, and at each step the spectrum was sampled for roughly 2 minutes at a sample rate of 0.5 Hz and recorded by a computer for further processing.

The spectral fringes obtained from the HR-SLI are in logarithmic scale. They are first transformed into a linear scale and then normalized by the maximum intensity of each of the spectral fringes. A typical spectral fringe after normalization is shown in Figure 3.6(a), in which no visible noises and distortions from pure cosine waves were observed. In order to estimate the SNR of the obtained signal, an enlarged view of the spectral fringe from 1539 to 1540 nm is shown in Figure 3.6(b). This corresponds to the second peak of the spectral fringe in Figure 3.6(a). The small intensity fluctuations, that are caused by the light source power variations and detector noise of the HR-SLI, and the ambient perturbations to fiber operation conditions, are evident. The standard deviation of the fluctuations is estimated

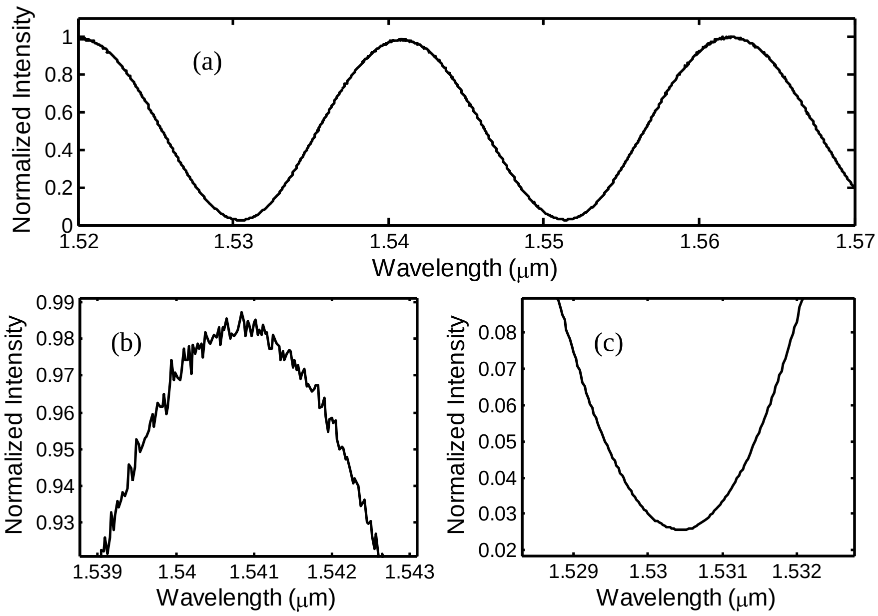

Figure 3.6: A typical fringe obtained by the HR-SLI (after normalization), (a); and enlarged view of a fringe peak, (b); and a fringe valley, (c).

to be 0.003, which is obtained by finding the standard deviation of the fitting errors when a small range of the fringes centering at the peak position is LSE fitted by a parabolic function. Considering the unit peak-to-peak value of the fringes, this leads to a SNR of 25 dB of the spectral fringe signal at fringe peaks. Note that the fluctuations of the fringe intensity is much smaller at fringe valleys, as shown in Figure 3.6(c), which is the enlarged view of the first fringe valley in Figure 3.6(a) and shows no evident fluctuation. The larger SNR at fringe valleys implies that the valley wavelength positions might be determined more accurately than the fringe peak positions. And fringe valleys instead of peaks should be used in those signal processing methods that only use part of the fringes, such as the wavelength-tracking method and the two-point interrogation method.

3.4.2 Type 1-3 curve-fitting methods

Type 1-3 curve fitting methods use Eqs. (3.15), (3.16) and (3.17), respectively, to fit the measured spectrum in order to obtain the gap-length d. The 1-D grid search processing shown in Table 3.2 was used in the fitting process. The gap-length grid interval $(d_i - d_{i-1})$, which set the upper limit of the measurement resolution, should be small enough to achieve the best measurement resolution. In this case it was set to 0.1 nm, which is adequate because gap-length grid interval of 0.1 nm is smaller than the measurement resolution limited by the signal noise itself, which will be shown later in this subsection.

The major differences between Type 1-3 curve fitting methods are that (1) the coupling-induced phase shift is unknown in mathematic models used by Type 2 and Type 3 curve fitting methods; (2) the linear modification of the fringe envelop is partially compensated in Type 1 curve fitting method, while it is not considered in the other two methods; (3) Type 3 curve-fitting method takes into account the multi-reflections inside the FP cavity. The influences of these differences can be shown by comparing the fitting errors of these three methods, as shown in Figure 3.7(b), which plots the fitting errors of these three methods when they are used to fit the spectral fringes shown in Figure 3.7(a). It is evident that the fitting errors for Type 1 and Type 2 curve fitting methods are largely caused by ignoring multi-reflections between the two reflectors in Eqs. (3.15) and (3.16) as the fitting errors show apparent cosine wave patterns that are related to the optical-path-difference (OPD) of $4d$ caused by the multi-reflections. The cosine wave pattern of fitting errors is literally eliminated in Type 3 curve fitting method. It is further noticed that the envelops of the fitting errors or the long-term fluctuations of the fitting errors with wavelength from both Type 2 and Type 3 curve-fitting methods are less uniform than that from Type 1 curve-fitting method (Figure 3.7(b)). This is so because Type 1 curve-fitting method is able to partially compensate the linear change of the cosine wave envelop with wavelength by adding the term of $b/\lambda + g$ in Eq. (3.14).

The systematic fitting error caused by ignoring multi-reflections in the FP cavity did

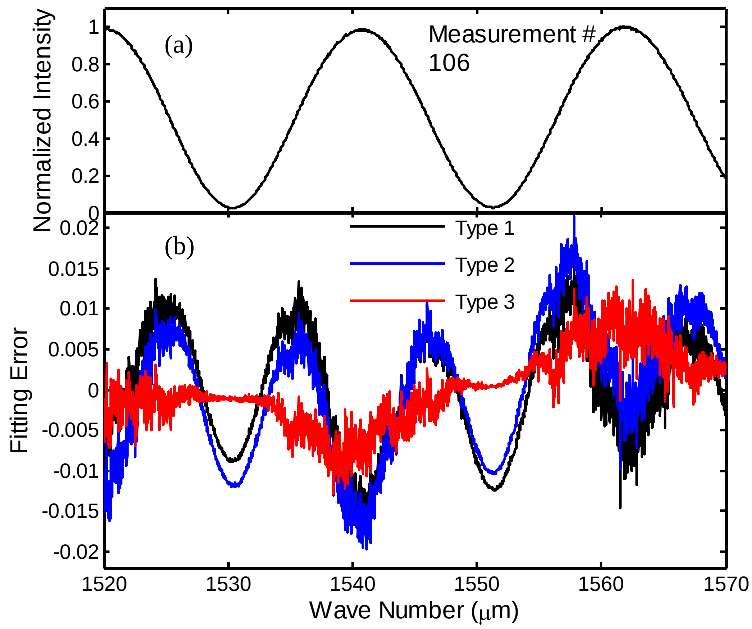

Figure 3.7: The normalized spectral fringes of measurement number 103, (a); and the fitting errors of Type 1, Type 2 and Type 3 curve-fitting methods when they are applied to fit the fringes in (a), (b).

not affect the measurement accuracy because the fitting parameter d is determined only by the fringe period and wavelength positions of the fringe valleys and peaks, which are not affected by ignoring the multi-reflections in Eqs. (3.15) and (3.16). The measured gap-lengths using Type 1-3 curve-fitting methods are shown in Figure 3.8(a). As indicated by the results from Type 1 curve-fitting method, the gap-length is increased from 55.0 to 62.4 nm through ten steps and the measured total gap-length change is approximately 7.4 μm. Virtually the three sets of results are almost overlapped with each other in Figure 3.8(a). However, the difference is clearly evident in Figure 3.8(b) which shows the enlarged view of the results from measurement number 103 to 156 that correspond to the third step level in Figure 3.8(a). Figure 3.8(b) also shows the three lines that represent the LSE linear fit of the measured gap-length as functions of the measurement number for the three methods. It is clear that the gap-length was slightly increased at this step of measurement. This is caused by the mechanical drift of the translation stage itself after the gap-length is adjusted. The

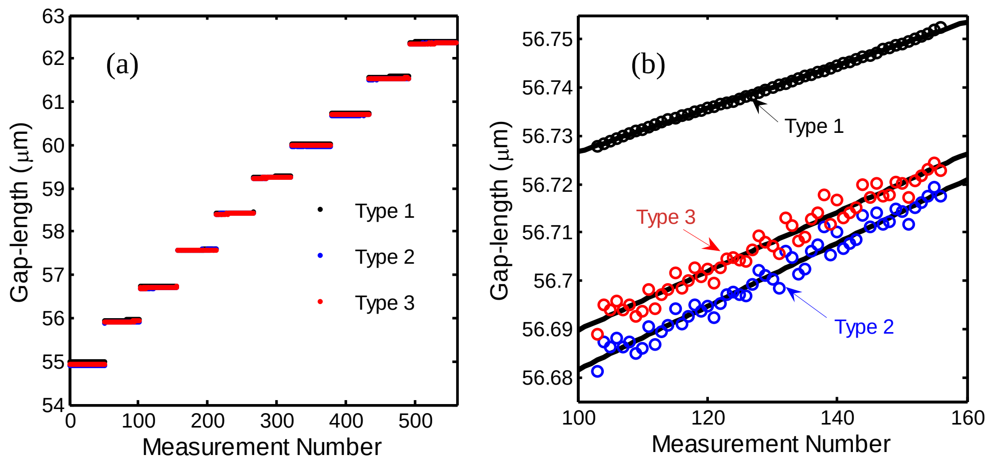

Figure 3.8: Comparison of results obtained by Type 1, Type 2 and Type 3 curve-fitting methods, (a); and the least-square linear fit of the gap-length as a function of measurement number, (b).

fluctuation of the measured points around the best-fit line through the data can be taken as a measure of the standard deviation of the algorithm. It is possible that some of the variation around the line is due to the mechanical translation stage as well. The standard deviation of the fitting error represents the variation due to all sources of error including the algorithm. Clearly, measurement results from Type 1 curve-fitting method have the least random fluctuations around their linear fit, which indicates that Type 1 method has the best performance in terms of measurement resolution among these three methods. The calculated standard deviations of the linear fitting errors are 0.22, 1.90 and 1.89 nm for Type 1, Type 2 and Type 3 curve-fitting methods, respectively. Therefore it is concluded that the measurement resolution of Type 1 curving-fitting method is approximately one order of magnitude better than Type 2 and Type 3 curving-fitting methods. Note that the measurement resolution values of all the three methods are larger than the gap-length grid interval (0.1 nm) used in the fitting process, which in turn verifies that the chosen grid interval is sufficiently small.

It is also worth noting that, in addition to the differences of the measurement resolution, there are systematic differences between the absolute gap-lengths measured by these three methods. For example, approximately the measured gap-lengths by Type 1 curve-fitting method are always 30-40 nm larger than the results from Type 2 curve-fitting method; while Type 2 curve-fitting method also gives the gap-lengths that are 6-8 nm larger than those given by Type 3 curve-fitting method. As shown in Figure 3.8(b), the measured gap-lengths from Type 2 and Type 3 curve-fitting methods are close, which indicates that the measurement accuracy is not significantly reduced by ignoring the multi-reflections in the FP cavity. In addition, it is found that the cosine wave fitting algorithm is sensitive to the long-term (on the order of fringe period) fluctuations of the spectral fringe envelop as a slight tilt of the measured spectral fringes (the linear modification of the fringe envelop as a function of wavelength) could cause relatively large changes in the fitting result. Therefore, it is anticipated that the Type 1 curve-fitting method gives best measurement accuracy among these three methods because the tilt of the measured spectrum is partially compensated. However it is difficult to experimentally verify.

3.4.3 Fourier transform method

As discussed in Section 3.2.3, in the Fourier transform method, the gap-length is obtained by finding the peak position in the Fourier transform domain of the spectral fringes. Before doing the Fourier transform, the DC component of the spectral fringes could be eliminated to reduce the sidelobe effect. Note that most spectrometers sample the spectrum being measured at discrete wavelengths with equal wavelength intervals. The sample intervals in wave number domain are not equal when the wavelengths are directly transformed to wave numbers as the wavelength and wave number relation is not linear. A set of data points with equal wave number intervals are required by the principle of the Fourier transform and can be achieved by data interpolation. Figure 3.9 shows the results from Fourier transform methods for two cases where the spectral fringes have DC (FT w/ DC) and have no DC components (FT w/o DC). The results from Type 1 curve-fitting method are also plotted for comparison.

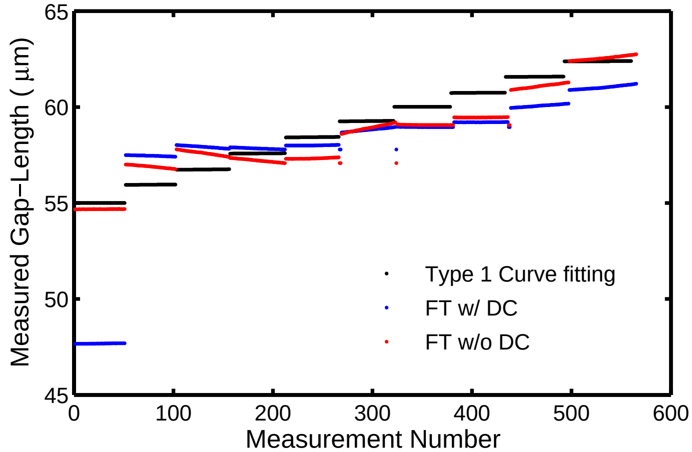

Figure 3.9: Comparison of results obtained by Type 1 curve-fitting, and Fourier transform methods. FT, Fourier transform.

The deviations of the Fourier transform results to the Type 1 curve-fitting results caused by the sidelobe effect are evident, random, and sometimes extreme. For example, "(FT w/ DC)" measures the gap-lengths of the first step to be around 48 μm, which is approximately 6 μm smaller than the results from Type 1 curve-fitting method. In addition, the Fourier transform results show that the measured gap-lengths slightly decreases in some step levels instead of the consistent slight increase from the results of the Type 1 curve-fitting method. Furthermore, the results from "FT w/o DC" indicate that the gap-lengths were reduced from step level 3 to step level 4, which is contrary to the experimental process where the 1-D translation stage was adjusted to consistently increase the gap-length for each step. Even the results from "FT w/ DC" and "FT w/o DC" are not consistent with each other, with one giving larger values of gap-lengths than the other in some levels and smaller values in other levels. In general, the 'FT w/o DC" results are closer to the Type 1 curve-fitting results as the sidelobe effect is smaller when the DC component is removed before the Fourier transform.

The results for step level 3 (Measurement number 103-156) together with the LSE linear fit as functions of the measurement number is plotted in Figure 3.10(a) for the methods

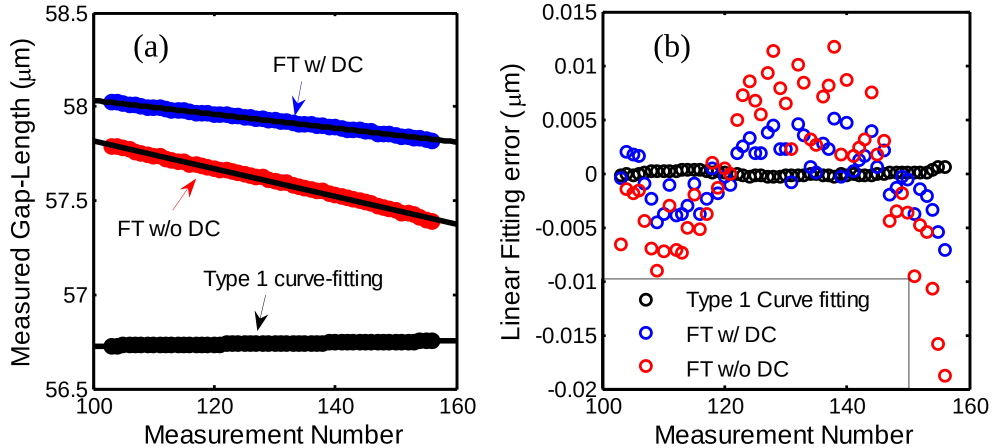

Figure 3.10: Least-square linear fit of the gap-length as a function of measurement number for Type 1 curve fitting and Fourier transform method, (a); and the linear fitting error, (b). FT, Fourier transform.

of Type 1 curve-fitting, "FT w/ DC", and "FT w/o DC". Similar to the discussion in Section 3.4.2, the measurement resolution of the Fourier transform method is also studied by calculating the standard deviation of the linear fitting errors as shown in Figure 3.10(b). Obviously, the fitting errors are much larger for Fourier transform method than for Type 1 curve-fitting method. The calculated standard deviations of the fitting errors are 2.83 and 6.89 nm for "FT w/ DC" and "FT w/o DC", respectively. Comparing the results from Section 3.4.2, the measurement resolution of Fourier transform method is on the same order of Type 2 and Type 3 curve-fitting methods and one order of magnitude worse than Type 1 curve-fitting method.

3.4.4 Two-point interrogation

The two-point interrogation is one of the most simple signal processing methods for white-light SMF-EFPI sensors. In this method, by finding the wavelength positions of two fringe peaks or valleys, the gap-length d can be calculated from Eq. (3.7). In order to achieve high accuracy and resolution, the determination of the peak and valley positions must be accurate

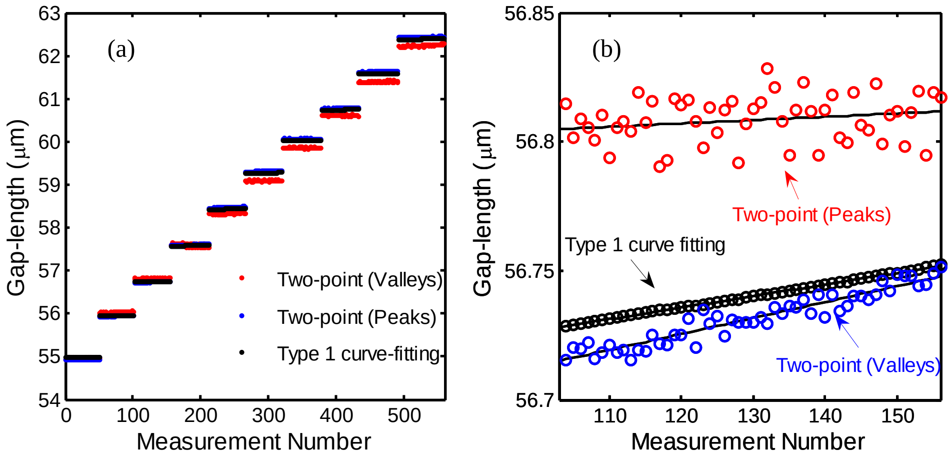

Figure 3.11: Comparison of results obtained by Type 1 curve-fitting method and two-point interrogation, (a); and the least-square linear fit of the gap-length as a function of measurement number, (b).

and have high resolution. As shown in Section 3.4.1, the spectral fringes obtained by the HR-SLI have better SNR at valleys than at peaks, therefore, it is expected the measurement results from two fringe valleys have better resolution performance. To find the wavelength position, first a rough wavelength position of a valley or peak, λ_i' is found. The accurate valley or peak position, λ_i, is then obtained by fitting a small range of the fringes centering at λ_i' using a parabolic function and finding the wavelength at which the maximum of the function occurs.

The measurement results using two-point interrogation are shown in Figure 3.11(a). Note that for each step, a set of two neighboring peaks or valleys with fixed order numbers is used. The results from Type 1 curve-fitting method are also plotted for comparison. Figure 3.11(b) is the enlarged view of the third step in Figure 3.11(a), together with their LSE linear fit function as the measurement number. The measurement resolutions, as approximated by the standard deviations of the fitting errors, are 3.12 and 9.25 nm for the two-point interrogation method using two neighboring valleys and peaks, respectively. As expected, the measurement resolution in case of Two-valley interrogation is three times better than the case of two-peak interrogation due to the smaller fluctuations in fringes valleys of the measured spectral fringes; however, it is still 20 times larger than the Type 1 curve-fitting method.

It is worth noting that there are systematic errors as well between results obtained from the two-peak and two-valley interrogations. The latter one gives a closer result to the Type 1 curve-fitting method. Even within the two-peak interrogation, the results obtained using one set of two neighboring peaks systematically deviated from the results obtained from another set of neighboring peaks with different order numbers. This is also true for the two-valley interrogation. Therefore, for the two-point interrogation, the measurement resolution could be significantly deteriorated if the order numbers of the two neighboring peaks or valleys are randomly picked. In our experiment, there are three valleys (V1, V2, V3) for each spectral fringe. This gives two choices of two neighboring-peaks in the calculation of gap-lengths, namely, (V1, V2) and (V2, V3). Figure 3.12 shows the measured gap-length results from the two-valley interrogation which randomly choses one of the above two sets. Obviously, the measurement resolution is significantly deteriorated. For each gap-length step, the standard deviation of the errors between the measured gap-length values and their LSE linear fit is on the order of several hundred nanometers, which is two orders of magnitude worse than the case where the order numbers of neighboring peaks are fixed, and three orders of magnitude worse than the Type 1 curve-fitting method. Therefore, the two-point interrogation has limited absolute measurement accuracy which in turn significantly deteriorates the performance of the measurement resolution of this method in cases where the gap-length changes are large and different sets of two peaks or valleys have to be used.

3.4.5 Wavelength-tracking method

Wavelength-tracking method uses the wavelength position of a particular fringe peak (or valley) to map the parameters being measured and is shown to have an ultra-high measurement resolution in a high-finesse white-light SMF-EFPI sensor system [36]. Even though this method has limited dynamic range and is not capable of absolute measurement, it

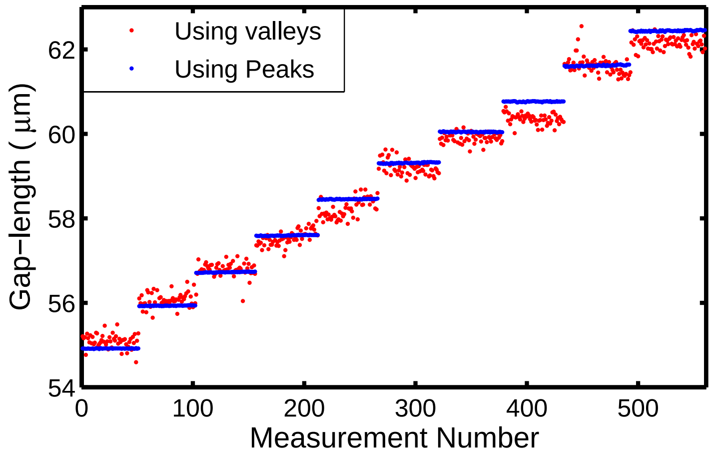

Figure 3.12: Comparison of the two-point interrogation results obtained by using fringe peaks (red dot) and fringe valleys (blue dot).

is still widely used in SMF-EFPI sensors especially in laboratories due to its advantages of signal processing simplicity and ultra-high measurement resolution. In this subsection, the gap-length results of the third-step (measurement number 103-156) obtained by the wavelength-tracking method is presented. The first peak and valley of each spectral fringe are used. The results from the peak-tracking and valley-tracking are compared. The wavelength positions of the peaks or valleys are obtained using the polynomial fitting method as shown in Section 3.4.4. Since absolute gap-length measurement is not possible for this method, it is assumed that the gap-length of the first measurement is $d_0 = 50\ \mu m$. Suppose λ_i is the wavelength of the first peak or valley of the i^{th} measured fringe, then the gap-length d_i is estimated by

$$d_i = d_0[1 + (\lambda_i - \lambda_{103})/\lambda_0], \quad i = 103, \cdots, 156 \tag{3.27}$$

where $\lambda_0 = 1550$ nm is the central wavelength of the fringe.

The gap-lengths obtained through Eq. (3.27) is shown in Figure 3.13(a). Results from both the peak-tracking and the valley-tracking are plotted together with their 10 order polynomial fit. The higher order fit is used so that the difference of the standard deviations between these two is more evident. The fitting errors are shown in Figure 3.13(b). The

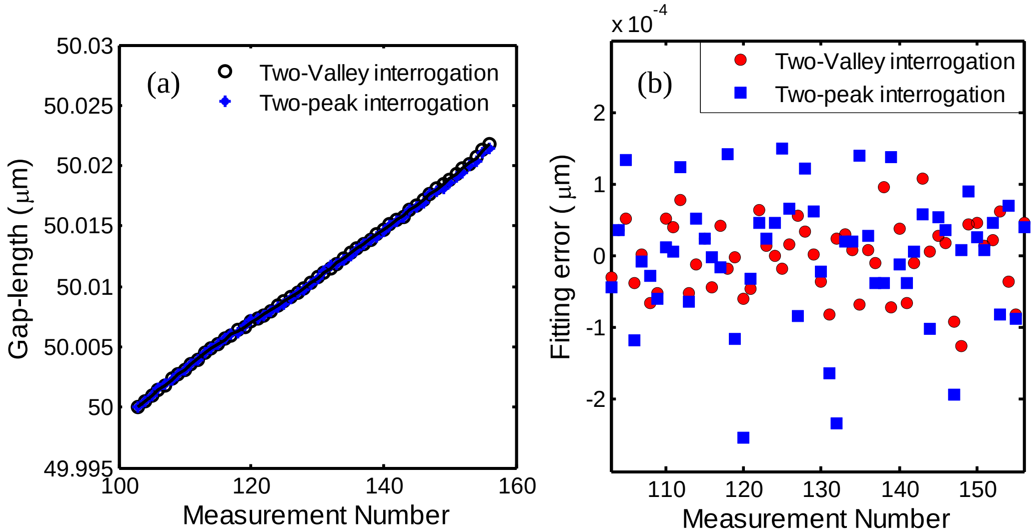

Figure 3.13: Estimated gap-lengths for step 3 from the wave-length record together with its 10 order polynomial fit, (a); and the fitting errors,(b).

standard deviations are 0.05 and 0.09 nm for the valley-tracking and the peak-tracking, respectively. The smaller standard deviation of the valley-tracking is expected as the fringes are less noisy in valleys. Note that the standard deviations of the fitting error are considerably smaller than the case of the Type 1 curve-fitting method. This is so only because a higher order polynomial fit is used here. For example, the standard deviations of the second order polynomial (parabolic) fitting are 0.2 nm for both the valley-tracking and the peak-tracking, which is the same as that of the Type 1 curve-fitting method.

3.5 Conclusions

This chapter studies the principle and performance of various spectral domain signal processing methods for white-light SMF-EFPI sensors, including the methods of two-point interrogation, Fourier transform, Type 1 - 3 curve-fitting, and wavelength-tracking. Except for the wavelength-tracking method, the other methods are featured by the the capabilities of absolute measurement of the air-gap and large dynamic measurement range.

The first is the Type 1 curve-fitting method. By obtaining the exact expressions of the fringe phase as a function of the gap-length from the model of the SMF-EFPI sensors, this method achieves the best measurement resolution (0.2 nm) among all the methods that are capable of absolute measurement. In addition to the SNR of the spectral fringes, the measurement accuracy of this method is also dependent on the accuracy of predicted coupling-induced phase-shift, which is obtained by the model of a perfect sensor head. Therefore, the errors might be introduced by various imperfections of the sensor such as the non-parallelism of the two fiber ends. The model assumes the spectral fringe is a cosine function with a linear amplitude modulation as a function of the wave number; however, more complex modulations of the fringe envelope due to bending losses of the single mode fiber may cause the fitting process to converge to an erroneous gap-length value. This could be compensated for by using a higher order polynomial to fit the envelope modulations. The accurate and absolute measurement of wavelength is important in the successful application of the proposed algorithm. Moreover, it is necessary for the source spectrum to be stable during the measurement process. Small errors in wavelength measurement, and/or small fluctuations in light source spectrum could also cause the fitting process to converge to an erroneous gap-length value. The stringent requirement on sensor systems is a price we have to pay to achieve high-resolution, high accuracy, and absolute measurement at the same time.

The Type 2 and Type 3 curve-fitting methods have the second best measurement resolution performance (approximately 2 nm for both of them). Different from the Type 1 curve-fitting method, the models used in these two methods assume an unknown coupling-induced phase-shift. Actually the phase-shift can be alternatively considered as a fitting parameter in the fitting models of Type 2 and Type 3 curve-fitting methods. It is the absence of this phase-shift information that causes the reduction of the measurement resolution compared to their Type 1 counterpart. Type 3 curve-fitting methods takes into account the multi-reflections in the FP cavity, therefore the model is more accurate in describing the spectral fringes, which is verified by the much smaller fitting errors. However no improvement in the measurement resolution was found. On the other hand, the consideration of multi-reflections

Table 3.3: Performances of signal processing methods for SMF-EFPI sensors

	T1	**T2**	**T3**	**FT**	**TPI**	**WT**
Resolution	0.22 nm	1.90 nm	1.89 nm	2.83 nm	4.5 nm	<0.2 nm
Accuracy	High	High	High	Low	High	NA
Speed	Low	Low	Low	High	High	High
Absolute?	Yes	Yes	Yes	Yes	Yes	No

Note: T1-T3, Type 1 -3; FT, Fourier transform; TPI, Tow-point interrogation; WT, wavelength-tracking. The FT method uses DC-removed fringes; and TPI used two neighboring fringe valleys.

dramatically increases the complexity of the models and the fitting algorithm, and consequently slows the signal processing speed. Therefore the Type 3 curve-fitting method is less desirable than the Type 2 method.

The Fourier transform method gives the poorest measurement accuracy performance because of the sidelobe effect. The computer simulations show that gap-length measured by the Fourier transform method oscillates around its true value as the gap-length increases. In addition to the accuracy, this oscillation could cause measurement ambiguities of the gap-lengths because the fringes of sensors with different gap-lengths could yield the same measured value. Thus this method is not suitable for measurement of large dynamic changes. The sidelobe effect can be reduced by increasing the gap-lengths. However, this is not an effective method for SMF-EFPI sensors in which the gap-lengths are at most several hundred micrometers to maintain a useful fringe visibility. The Fourier transform method might be effective for SMF intrinsic FP interferometric sensors in which the gap-length can be as long as centimeters without sacrificing the fringe visibility.

The next processing method is called the two-point interrogation. As its name suggests, the gap-length is obtained by the wavelength of two special points (fringe valleys or peaks) in the fringes. The accuracy of this method is directly related to the accuracy in determining the wavelengths of the fringe peaks or valleys. Different from all the other methods which use the whole fringes to find the gap-length, this method only uses two small portions of the fringes. Thus only the SNR of two local fringe portions being used matters for the measurement resolution. The measurement resolution of this method is less than 10 nm if the same orders of the set of two neighboring peaks or valleys are used through out the measurement. However, the results obtained from different sets of fringes or peaks are not consistent and this leads to a significantly reduced measurement resolution when changes of the gap-lengths are large.

The last signal processing method is the wavelength-tracking method. Different from the others, this method is not capable of absolute measurement. However, the big advantages of this method are its simplicity and high resolution. Our experimental results have shown that the measurement resolution is at least comparable with, if not better than, the Type 1 curve-fitting method.

Another important aspect in evaluating a signal processing method is the processing speed. The curve-fitting methods take longest time to obtain the gap-length from a fringe as the grid-search method used in the cosine wave fitting process requires a large number of iterations. The two-point interrogation and Fourier transform method are much faster due to their simplicity.

The test results of performances of these methods are summarized and compared in Table 3.3.

Chapter 4

Low-finesse MMF-EFPI sensors

As discussed in Chapter 1, previously available analysis on MMF-EFPI sensors is based on geometric-optics and is only valid in limited situations as geometric-optics is an approximate theory. In this chapter a modal theory that can, in principle, be used in any situation is presented. The modal theory is capable of accurately predicting the spectral fringes by a complete treatment on mode mixing and interference in the MMF-EFPI sensors and is used to analyze the fringe visibility of MMF-EFPI sensors with various fiber types and sensor configurations. To the best of our knowledge, this is the first time that a modal theory is developed to model the MMF-EFPI sensors.

This chapter is constructed as follows. In Section 4.1, the theory based on geometric-optics is reviewed. In Section 4.2 an exact analysis on the fringe visibility and fringe pattern of MMF-EFPI sensors based on the electromagnetic theory is presented. Even though a weakly guiding fiber is used in our analysis, the method is applicable for fibers of any kind. Then the numerical results of visibility analysis based on the theory are discussed in Section 4.3. First, the effect on fringe visibility of the sensor parameters including the fiber core size, NA of the fiber, the modal power distribution in the lead-in fiber, and the gap length of the F-P cavity, is studied. Next, the effect of one of the typical interferometer imperfections, in which the two reflection surfaces of the FP cavity are not perfectly parallel to each other and forms a wedge angle, is studied. The comparison between MMF-EFPI sensors and SMF-EFPI sensors is performed in Section 4.5 and the fundamental mechanisms responsible for the reduction of visibility of a MMF-EFPI sensor is reported in Section 4.6. The mode-lobe position effect in MMF-EFPI sensors is revealed and analyzed in Section 4.7. Section 4.8 analyzes the visibility variations caused by the mode-mixing that occurs in the sensor head. In Section 4.9, the modal theory for a more general MMF-EFPI sensor configuration is developed and used for visibility analysis. In Section 4.10, an experiment is carried out to study the visibility variations owing to wedge angle and the results are compared to theoretical results to validate the theory. Finally, some conclusions are given in Section 4.11.

4.1 Review of low-finesse MMF-EFPI theory

In this Section we follow the methodology reported by Pérennès [20], who used the geometric-optics to analyze the fringe visibility performance of a MMF low-finesse FP interferometer (FPI). A schematic of a FPI, illuminated by the output of a multimode optical fiber, is shown in Figure (4.1). The FPI is located at a distance z_0 from the fiber end face. The medium between the fiber and the FPI has a refractive index n_1, and the medium on the external side of the FPI has a refractive index n_2. The refractive index inside the FPI is n, and n_f is the refractive index of the fiber core. The reflection coefficients of the mirrors of the interferometer are defined by the weak Fresnel reflections arising from the refractive-index mismatches at the two surfaces of the interferometer and are therefore small. It is assumed that all the propagation modes in the optical fiber are equally excited. Thus the output light distribution at the distal end of the fiber is of uniform intensity and conforms to that of a top-hat profile. Under these conditions, the maximum angle of divergence θ_m depends on the $\mathtt{NA}$ of the fiber and, in air, is given by $\theta_m = \sin^{-1}(\mathtt{NA})$. The light emerging from the fiber can be represented by the sum of wave fronts of equal amplitude, leaving the fiber at different angles distributed between 0 and θ_{d1}. Angles θ_{d1} and θ_d are the angles of the most diverging wave fronts in the medium between the fiber and the FPI and inside the FPI, respectively.

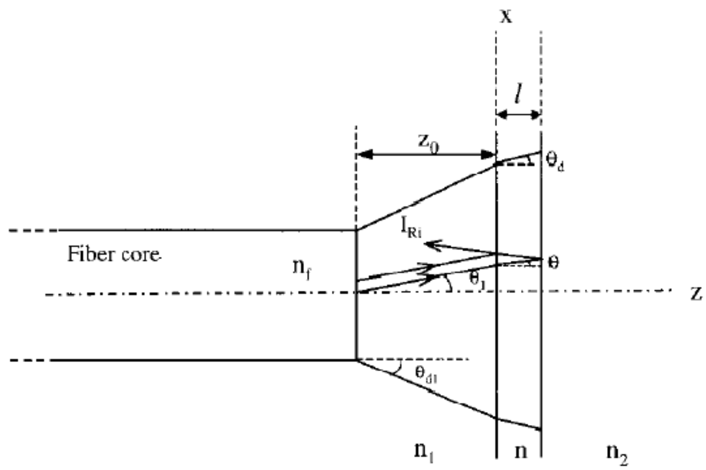

Figure 4.1: Schematic of a FPI illuminated by a MMF. θ_{d1} and θ_d are the angles of the most diverging rays in the media between the fiber and the FPI and in the FP cavity, respectively. θ_1 and θ are the angles of a particular ray in the media between the fiber and the FPI and in the FP cavity, respectively. Reprint from Ref. [20]

They obey Snell's law:

$$\sin\theta_{d1} = \sin(\theta_d)n/n_1. \tag{4.1}$$

Two parallel incident rays, corresponding to an internal angle θ within the FPI, are reflected on both sides of the cavity and interfere, as shown in Figure 4.1. Because of the low spatial coherence of the output of a multimode fiber (which is due to the different phases of individual modes), it is necessary that both the FPI thickness and the maximum angle of divergence are small. This ensures that the two interfering rays originate from nearly the same point on the optical fiber end-face and are therefore located within a region of spatial coherence and are correlated in phase. Under these conditions, uncorrelated random variations in the absolute phase across the fiber output that are due to external perturbations of the fiber do not affect the interference process. The net phase difference between the two reflections is given by [28]

$$\phi(\theta) = \cos(\theta)4\pi nl/\lambda, \tag{4.2}$$

where n is the refractive index in the FP cavity, l is the cavity thickness, and λ is the light-source wavelength. The weak Fresnel reflections at the interferometer surfaces allow to neglect the effect of multiple reflections inside the cavity [29]. Thus the cavity acts as a low-finesse FPI, and the intensity of the reflected light is simply due to the coherent superposition of the two Fresnel reflections. The reflected intensity resulting from the interference of two parallel rays for an internal angle θ is given by

$$I_{R_i}(\theta) = \frac{I_0}{\Delta\phi}[R_1 + (1-R_1)^2 R_2 + 2(R_1R_2)^{1/2}(1-R_1)\cos\phi(\theta)], \tag{4.3}$$

where I_0 is the total intensity of the light incident upon the FPI. R_1 and R_2 are the Fresnel reflection coefficients on each side of the interferometer. $\Delta\phi$ is the total phase dispersion and is a measure of the range of optical path lengths taken by interfering rays at different angles θ within the interferometer, as discussed below. When observed in a plane perpendicular to the fiber axis, the reflected light forms a pattern of concentric circular fringes of equal inclination. Dark fringes correspond to the interference of rays propagating at an angle of $\theta = \cos^{-1}\{[(2m+1)\lambda]/4nl\}$ inside the FP cavity and bright fringes to rays propagating at an angle $\theta = \cos^{-1}(2m\lambda/4nl)$, where m is an integer. The maximum phase difference occurs for a ray propagating along the fiber axis with $\theta = 0$, and the minimum phase difference occurs for the most divergent ray $\theta = \theta_d$ in the cavity. Thus the effect of divergence is to introduce dispersion into the phase difference. This phase dispersion can be expressed as

$$\Delta\phi = \phi_{max} - \phi_{min} = (1-\cos\theta_d)4\pi nl/\lambda = \phi_0(1-\cos\theta_d), \tag{4.4}$$

where ϕ_0 is the phase difference for a normally incident beam. The top-hat incident intensity profile yields a uniform distribution of phase difference in the interval defined by

$$\begin{cases} D(\phi) = 1, & \text{for } \phi_0 - \Delta\phi < \phi < \phi_0 \\ D(\phi) = 0, & \text{elsewhere} \end{cases} \tag{4.5}$$

To calculate the total reflected light I_R it is necessary to integrate the expression in Eq. (4.3) over the range of phase dispersion introduced by the divergence of light at the fiber output:

$$\begin{aligned} I_R &= \int_{\Delta\phi} D(\phi) I_{R_i}(\phi) d\phi \\ &= \left[R_1 + (1-R_1)^2 R_2 + \frac{2(R_1R_2)^{1/2}(1-R_1)}{\Delta\phi} \int_{\phi_0-\Delta\phi}^{\phi_0} \cos\phi d\phi \right] I_0. \end{aligned} \tag{4.6}$$

This expression can be evaluated analytically and gives

$$I_R = \left[R_1 + (1-R_1)^2 R_2 + 2(R_1R_2)^{1/2}(1-R_1) \frac{\sin(\Delta\phi/2)}{\Delta\phi/2} \cos\left(\phi_0 - \frac{\Delta\phi}{2}\right) \right], \tag{4.7}$$

where I_0 is the total incident light intensity in the FP plane. From Eq. (4.7) the maximum and the minimum values of the reflected intensity, I_{max} and I_{min}, occur when $\phi_0 - \Delta\phi/2 = 2k\pi$ and $\phi_0 - \Delta\phi/2 = (2k+1)\pi$, respectively, where k is an integer. The analytical solution for the fringe visibility $(I_{max} - I_{min})/(I_{max} + I_{min})$ is simply expressed as

$$\gamma = \frac{2(R_1R_2)^{1/2}(1-R_1)}{R_1 + (1-R_1)^2 R_2} \frac{|\sin(\Delta\phi/2)|}{\Delta\phi/2} = \gamma_0 \frac{|\sin(\Delta\phi/2)|}{\Delta\phi/2}, \tag{4.8}$$

where γ_0 is the visibility for a collimated incident beam. γ is zero for $\Delta\phi = 2k\pi$ (k is an integer).

Equation (4.7) predicts that the fringe pattern output from such a FP interferometer and Equation (4.8) describes the visibility of the fringes reflected from the interferometer before they enter the optical fiber. These two equations are the major results obtained by the theory.

The major advantage of the geometric-optics-based theory is that the analytical results are possible so that it is convenient to conceptually analyze the effect of different sensor parameters on the spectral fringes from a MMF-EFPI sensor. However, this theory also has many limitations. First, the analysis has assumed a "top-hat" light intensity profile of the MMF output. However, the intensity profile from a MMF could be much more complicated in practice and can only be accurately described by optical modes in the MMF. Secondly, the geometric-optics which it bases on is only valid for weakly-guiding MMFs. Moreover, the

MMFs must have sufficient number of modes propagating inside the fibers and the fiber core sizes much larger than the light wavelength. For example it can not be applied to MMFs with only a few modes, MMFs with small core sizes, and strongly-guiding MMFs, which are common in MMF-EFPI sensors. In the analysis it has been assumed that the cavity thickness and the internal divergence are sufficiently small that near-complete overlap occurs between the reflections on the two sides of the cavity, which could introduce significant errors to the results as this assumption is not always fulfilled. Most importantly, the theory is not capable of accurately predicting the spectral fringes which is important in the analysis and development of signal processing methods of MMF-EFPI sensors. All these limitations of the geometric-optics-based theory suggest that a more universal and accurate theory of MMF-EFPI sensors is necessary to provide a more powerful tool in the design and optimization of sensors.

4.2 Modal analysis of MMF-EFPI sensors

In this section, a model theory that accurately describes the spectral fringes output from a MMF-EDFA is presented. First the relationship between the spectral fringes and the modes in the MMF is developed in Section 4.2.1; Then the calculation of mode profiles of both step-index and graded-index MMFs is reviewed in Section 4.2.2. Finally, the calculation of the mode coupling coefficient, which is of great importance in understanding the performance of a MMF-EFPI sensor, is presented in Section 4.2.3.

4.2.1 Spectral fringes representation

A schematic of a low-finesse MMF-EFPI used in the modal theory is shown in Figure 4.2. The F-P cavity is formed by the end face R_1 of the lead-in multimode fiber and another reflection surface R_2. For an ideal EFPI, R_1 and R_2 are perfectly parallel to each other and are perpendicular to the fiber axis z. n_3 is the refractive index inside the F-P cavity. For

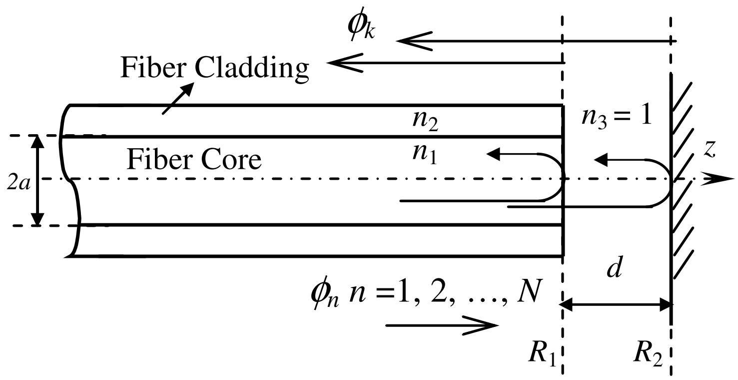

Figure 4.2: Schematic of a low finesse MMF-EFPI.

simplicity, it is assumed that the cavity is filled with air and thus, $n_3 = 1$. The gap length d is defined as the distance between R_1 and R_2. The reflection coefficient r_1 of surface R_1 and reflection coefficient r_2 of surface R_2 are defined by the weak Fresnel reflection arising from the refractive index mismatches at the two surfaces. In practice, the reflections at the interfaces are usually small. The light propagating along the lead-in/out MMF is partially reflected by R_1 and R_2, and the two reflections are coupled back into the lead-in MMF and interfere with each other to form interferometric fringes.

Assume the multimode fiber supports N orthogonal guided eigenmodes with the normalized field profile of the k^{th} mode ϕ_k $(k = 1, 2, ..., N)$. The total field of the light propagating along the $+z$ direction may be expressed as a superposition of all the guided modes, which can be written as [30]

$$\mathsf{E}_{total} = \sum_{k=1}^{N} p_k \phi_k \exp(-j\beta_k z)\hat{\mathsf{e}}_k, \tag{4.9}$$

where $\hat{\mathsf{e}}_k$ is a unit vector representing the polarization of the mode, so that

$$\hat{\mathsf{e}}_k \cdot \hat{\mathsf{e}}_k^* = 1, \tag{4.10}$$

and coefficient p_k is the complex magnitude of the k^{th} mode. The amplitude of $|p_k|$ is related to the mode power distribution (MPD) in the fiber. For example, if all the modes in the multimode fiber are equally excited, they all have the same intensity, so $|p_k| = p$ for $k = 1, 2, ..., N$, where p is a constant. The intensity of the reflected light can be expressed as the superposition of the intensities of all the modes since they are orthogonal:

$$\begin{aligned} I_{tot} &= \langle \mathtt{E}_{total} \cdot \mathtt{E}^*_{total} \rangle = \sum_{k=1}^{N} (p_k \phi_k)(p_k \phi_k)^* (\hat{\mathtt{e}}_k \cdot \hat{\mathtt{e}}^*_k) \\ &= \sum_{k=1}^{N} (p_k p^*_k) \end{aligned} \tag{4.11}$$

where the angle brackets, $\langle\ \rangle$, denotes the integral over the cross-section plane of the fiber. In deriving Eq. (4.11), I have used Eq. (4.10) and the orthogonality of the mode profiles described by

$$\langle \phi_l \phi^*_k \rangle = \begin{cases} 1, & l = k \\ 0, & l \neq k \end{cases} \tag{4.12}$$

Similarly, for the reflected light propagating along the $-z$ direction, the field can also be decomposed into a set of guided modes:

$$\mathtt{E} = \sum_{k=1}^{N} q_k \phi_k \exp(-j\beta_k z) \hat{\mathtt{e}}_k, \tag{4.13}$$

and the intensity of the reflected light is expressed as

$$I = \langle \mathtt{E} \cdot \mathtt{E}^* \rangle = \sum_{k=1}^{N} \langle q_k q^*_k \rangle = \sum_{k=1}^{N} I_k. \tag{4.14}$$

Now consider the field of a particular mode $q_k \phi_k$ of the reflected light. Since the Fresnel reflections at the reflection surfaces are low, the effect of the multiple reflections in the cavity is neglected. Thus, the reflected light comes from the two reflections at surface R_1 and surface R_2. Since surface R_1 is perpendicular to the fiber axis, the k^{th} mode propagating along $+z$ direction reflected by surface R_1 will be coupled back to the same k^{th} mode propagating along $-z$ direction. However, due to the lateral displacement d (gap-length) of surface R_2 to the fiber end face R_1, only part of the mode k propagating along $+z$ direction that is reflected by surface R_2 can be coupled back to mode k. Furthermore, modes with mode numbers different from k that are reflected by surface R_2 can also be coupled into mode k.

Thus, the reflected field profile of mode k can be expressed as the summation of two terms:

$$q_k\phi_k = rp_k\phi_k + r\sum_{l=1}^{N}\eta_{lk}p_l\phi_k\exp[-j(4\pi d/\lambda+\pi)]. \tag{4.15}$$

Note that it has been already assumed that $r_1 = r_2 = r$ and the light power loss due to the Fresnel reflection of surface R_1 when the reflected light from surface R_2 is coupled to the MMF is neglected. In Eq. (4.15), the first term $rp_k\phi_k$ is the reflection at surface R_1; the second term as a whole is the contribution from the reflections of the surface R_2, in which η_{lk} is defined as the coupling coefficient of the l^{th} mode that propagates along $+z$ direction and is reflected back by the surface R_2 to the k^{th} mode that propagates along $-z$ direction in the MMF. The light coupling occurs at surface plane R_1. In Eq. (4.15), phase shift $4\pi d/\lambda$ arises from the free-space transmission of a distance of $2d$, and the extra phase-shift of π arises from the light reflection from an optically less dense medium to an optically denser medium. For convenience, the reflection coefficient r which is common for all modes is ignored in the following analysis. Defining the following parameters

$$\eta_k = \eta_{kk} = |\eta_k|\exp(j\theta_k), \tag{4.16}$$

$$p_l = |p_l|\exp(j\varphi_l), \tag{4.17}$$

$$\varphi_0 = 4\pi/\lambda+\pi, \tag{4.18}$$

$$c_k = |c_k|\exp(j\theta_k') = \sum_{l=1,l\neq k}^{N}\eta_{lk}p_l, \tag{4.19}$$

the complex amplitude of mode ϕ_k can be expressed as

$$q_k = |p_k|\exp(j\varphi_k) + |\eta_k||p_k|\exp[-j(\varphi_0-\theta_k-\varphi_k)] + |c_k|\exp[-j(\varphi_0-\theta_k')]. \tag{4.20}$$

It is clear that the contributions to mode ϕ_k from the the reflections of the surface R_2 are divided into two terms in Eq.(4.20), namely the contributions from the same mode reflected by the surface R_2 and the contributions from all the other modes reflected by the surface

R_2. The reflected light intensity of mode k is then expressed as

$$\begin{aligned} I_k &= < q_k q_k^* > \\ &= < |p_k| \exp(j\varphi_k) + |\eta_k||p_k| \exp[-j(\varphi_0 - \theta_k - \varphi_k)] + |c_k| \exp[-j(\varphi_0 - \theta_k')] \\ &\quad \times |p_k| \exp(-j\varphi_k) + |\eta_k||p_k| \exp[j(\varphi_0 - \theta_k - \varphi_k)] + |c_k| \exp[j(\varphi_0 - \theta_k')] > \\ &= |p_k|^2 + |\eta_k|^2 |p_k|^2 + |c_k|^2 \\ &\quad + |p_k||c_k| \cos(\phi_0 - \theta_k' + \varphi_k) \\ &\quad + |\eta_k||p_k||c_k| \cos(\theta_k' - \theta_k - \varphi_k) \\ &\quad + |\eta_k||p_k|^2 \cos(\phi_0 - \theta_k) \end{aligned} \tag{4.21}$$

Substituting Eq. (4.21) into Eq. (4.14) yields the total reflected light intensity I:

$$\begin{aligned} I &= \sum_{k=1}^{N} I_k \\ &= \sum_{k=1}^{N} |p_k|^2 + |\eta_k|^2 |p_k|^2 + |c_k|^2 \\ &\quad + 2\sum_{k=1}^{N} |p_k||c_k| \cos(\phi_0 - \theta_k' + \varphi_k) \\ &\quad + 2\sum_{k=1}^{N} |\eta_k||p_k||c_k| \cos(\theta_k' - \theta_k - \varphi_k) \\ &\quad + 2\sum_{k=1}^{N} |\eta_k||p_k|^2 \cos(\phi_0 - \theta_k). \end{aligned} \tag{4.22}$$

Noting that all modes propagating along the MMF have random initial phase relationship when they are excited by the light source and individual modes with different propagation constants experience different phase-shift during propagation along the fiber, it is reasonable to assume that the phase of the coefficients p_l, φ_l, is a random variable uniformly distributed in the phase range $[-\pi, +\pi]$. Consequently, the phase of coefficients c_k, θ_k', which is related to coefficients p_l through Eq. 4.19, is also a random variable. Furthermore, it is assumed that the number of the modes excited in the fiber is sufficiently large so that the summation of the terms related to φ_l and θ_k' is averaged to zero in Eq. (4.22). This assumption is reasonable for a typical MMF which usually supports several hundred modes at wavelengths around 1550 nm. Thus, Eq. (4.22) is simplified to be of the form:

$$\begin{aligned} I &= \sum_{k=1}^{N}(|p_k|^2 + |\eta_k|^2|p_k|^2 + |c_k|^2) \\ &\quad + \sum_{k=1}^{N}|\eta_k||p_k|^2\cos(\phi_0 - \theta_k) \end{aligned} \tag{4.23}$$

For simplicity, the input power of the lead in fiber is normalized to be unity, namely

$$I_{tot} = \sum_{k=1}^{N}|p_k|^2 = 1. \tag{4.24}$$

and further define

$$\eta_{R_2} = \sum_{k=1}^{N}(|\eta_k|^2|p_k|^2 + |c_k|^2), \tag{4.25}$$

Eq. (4.23) is then simplified to

$$I = 1 + \eta_{R_2} + \sum_{k=1}^{N}|p_k|^2|\eta_k|\cos(4\pi d/\lambda + \pi - \theta_k). \tag{4.26}$$

η_{R_2} is actually the light power coupling coefficient between the fiber F and its mirror image F' with respect to surface plane R_2, as shown in Figure 4.3. When the gap-length is small, for convenience, the power coupling coefficient can be obtained from geometric optics without sacrifice of accuracy. For two step-index MMFs that have a longitudinal offset $2d$, the light power coupling coefficient has been shown to be [31]

$$\eta_{R_2} = a^2/(a + 2d\tan\theta_c)^2, \tag{4.27}$$

where $\theta_c = \sin^{-1}[(n_1^2 - n_2^2)^{1/2}/n_1]$ is the critical acceptance angle of the fiber. Eq. (4.26) describes the spectral fringes output from a MMF-EFPI sensor. It is clear that the spectral fringes are a superposition of N sinusoidal functions each of which corresponds to a mode that propagates along the $+z$ direction in the MMF.

Define the *effective coupling coefficient*, η_{eff}, as

$$\eta_{eff} = |\eta_{eff}|\exp(j\varphi_{eff}) = \sum_{k=1}^{N}|p_k|^2\eta_k, \tag{4.28}$$

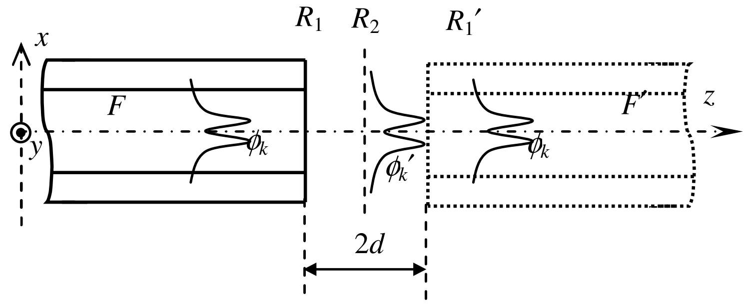

Figure 4.3: Schematic of calculating η_{R_2} and η_k. Fiber F' is the mirror image of the lead-in fiber F with respect to the reflection surface plane R_2.

where $|\eta_{eff}|$ and φ_{eff} are the amplitude and the phasor of the effective coupling coefficient, respectively. With the help of Eq. (4.28), the spectral fringe described by Eq. (4.26) can be further reduced to a single cosine function of

$$I(d, \lambda) = 1 + \frac{2}{1 + \eta_{R_2}} |\eta_{eff}| \cos(4\pi d/\lambda + \pi - \varphi_{eff}). \tag{4.29}$$

Eq. (4.29) is the major result of this chapter, which accurately describes the fringes output from a MMF-EFPI sensor system. Theoretically Eq. (4.29) which has overcome all the limitations imposed by geometric-optics is general. However, it is assumed in Eq. (4.29) that the mode number excited in the MMF must be large enough, so that the mode mixing effect can be ignored. For MMFs with arbitrary number of modes excited in the fiber, Eq. (4.22) must be used in the description of the spectral fringes.

4.2.2 Mode field profiles of MMFs

The knowledge of the mode field distribution of each mode present in the MMF is essential in the calculation of the spectral fringes from a MMF-EFPI sensor system by Eq. (4.29). Though the modal theory can be applied to any MMF, to keep the analysis as clear as possible and focused on the mode interactions rather than calculations of the modes themselves, this subsection only considers two types of weakly-guided MMFs, namely, the step-index MMF (SI-MMF) and the graded-index MMF (GI-MMF). The mathematical derivation of

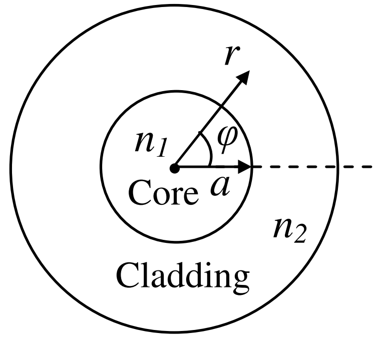

Figure 4.4: Diagram of a cross section of the fiber geometry considered here.

the mode field profiles from the fiber parameters for these two types of MMFs have been well-established and can be found in many textbooks. This subsection lists the results of mode field profiles of these fiber as they will be used in the simulation to analyze the fringe visibility of MMF-EFPI sensors.

SI-MMF

The structure of the SI-MMF is shown in Figure. 4.4. Since Δ is small, where $\Delta = (n_1 - n_2)/n_1$ is the normalized core-cladding index difference of the fiber, the linearly polarized (LP) mode approximation should be sufficient to describe the modes guided by the fiber [33]. With these assumptions, the characteristic equation in the fiber that can be solved to obtain the effective index, n_{eff}, of all possible modes with azimuthal number α is given by [33]

$$J_\alpha(u)/[uJ_{\alpha-1}(u)] + K_\alpha(w)/[wK_{\alpha-1}(w)] = 0, \tag{4.30}$$

where J is a Bessel function of the first kind, K is a modified Bessel function of the second kind, u and w are defined by $u = (2\pi a/\lambda)(n_1^2 - n_{eff}^2)^{1/2}$ and $w = (2\pi a/\lambda)(n_{eff}^2 - n_2^2)^{1/2}$ at wavelength λ, and the rest of the parameters are defined in Figure 4.4. Once Eq. (4.30) is solved, the field profile of an eigenmode in the fiber is readily obtained in terms of radial and azimuthal components as [33]:

$$\phi_k = A \begin{cases} [J_\alpha(ur/a)/J_\alpha(u)]\sin(\alpha\varphi + \varphi_0), \ r \le a \\ [K_\alpha(ur/a)/K_\alpha(u)]\sin(\alpha\varphi + \varphi_0), \ r > a \end{cases} \tag{4.31}$$

The number of guided modes that a fiber can support is determined by the normalized frequency V of the fiber, which is defined by $V = (2\pi a/\lambda)(n_1^2 - n_2^2)^{1/2}$. Provided $\alpha > 0$, the maximum value of α can be found by solving the inequalities:

$$\begin{cases} J_{\alpha-1}(V) < 0 \\ J_\alpha(V) \ge 0 \end{cases} \tag{4.32}$$

GI-MMF

The derivation of the mode profiles in a GI-MMF is much more complicated comparing to SI-MMF. Examples of approaches that have been investigated include the WKB approximation [44], the variational method [45][46][47], the finite element method [48], and the vector wave analysis [49]. Analytical solutions of the Maxwell Equations in GI-MMFs are only possible for a few special refractive profiles. Here without going into any detail, the result of the mode field profile for a parabolic-index MMF with infinite and homogeneous cladding is borrowed from a paper published by Garside [50] for later use in the analysis of fringe visibility of GI-MMF-EFPI sensors.

The refractive index profile of the GI-MMF considered here is given by

$$n(r) = \begin{cases} n_1 \left[1 - \delta(r/a)^2\right]^{1/2} & 0 \le r \le a \\ n_2 & r > a, \end{cases} \tag{4.33}$$

where $\delta << 1$ is a constant and $n_2 = n_1(1-\delta)^{1/2}$. With the weakly-guiding assumption, the LP approximation is applicable and the mode profile of an eigenmode in the fiber is given by

$$\phi_k = A \begin{cases} \Phi_\alpha(\xi)/\Phi_\alpha(\sigma)\sin(\alpha\varphi + \varphi_0), \ r \le a \\ K_\alpha(\omega r/a)K_l(\omega)\sin(\alpha\varphi + \varphi_0), \ r > a. \end{cases} \tag{4.34}$$

In Eq. (4.34), function $\Phi_\alpha(\xi)$ is defined by

$$\Phi_\alpha(\xi) = \xi^{\alpha/2}\exp(-\Phi/2)M(A,B,\xi), \tag{4.35}$$

where

$$\xi = (r/\omega_0)^2, \quad \omega_0^2 = a/n_1k_0\delta^{1/2}, \tag{4.36}$$

and $M(A,B,\xi)$ is the Kummer's function (also called Hypergeometric function) defined as

$$M(A,B,\xi) = \sum_{l=0}^{\infty}\frac{(A)_l\xi^l}{(B)_l l!}, \quad |\xi| < \infty, \ B \neq 0,-1,-2,\cdots, \tag{4.37}$$

with

$$\begin{aligned} A &= (1+\alpha)/2 - b/4, \\ B &= 1+\alpha, \\ b &= k_0 r_t n_1 \chi^{1/2}, \\ \chi &= \delta(r_t/a)^2 = 1 - \beta^2/n_1k_0^2. \end{aligned} \tag{4.38}$$

Here β is the longitudinal propagation constant and $k_0 = 2\pi/\lambda_0$ is the magnitude of the wave vector in free space. In Eq. (4.34), A is the field amplitude at $r = a$, K_α is the modified Hankel's function, and σ and ω are given by

$$\begin{aligned} \sigma &= \xi|_{r=a} = k_0 a n_1 \delta^{1/2} \\ \omega &= a(\beta^2 - n_2^2k_0^2)^{1/2}. \end{aligned} \tag{4.39}$$

The characteristic equation used for solving the propagaton constant β is given by

$$(u^2/b)N_\alpha(u) + 2\alpha = -(n_1/n_2)\omega K_{\alpha-1}(\omega)/K_\alpha(\omega), \tag{4.40}$$

where

$$u = (b\sigma)^{1/2} = a(n_1^2 j_0^2 - \beta^2)^{1/2} \tag{4.41}$$

and

$$N_\alpha(u) = \frac{2A}{B}\frac{M(A+1,B+1,u^2/b)}{M(A,B,u^2/b)}. \tag{4.42}$$

Note that Eq. (4.40) is the characteristic equation in the original paper(Ref. [50]) with the assumption that $n_1 \approx n_2$.

4.2.3 Mode coupling coefficient

Now consider the calculation of the mode coupling coefficient η_k. Assuming ϕ_k' is the eigenmode ϕ_k of fiber F, transmitted a distance of $2d$ to plane R_1' , the coupling coefficient is obtained by performing the overlap integral of ϕ_k' and ϕ_k over the surface R_1, which leads to [30]

$$\eta_k = \int \int_{R_1'} \phi_k' \phi_k^* dxdy. \tag{4.43}$$

The field profile of ϕ_k' is given by [32]:

$$\phi_k'(x, y) = \mathbf{F}_{xy}{}^{-1} \left\{ \mathbf{F}_{xy} \left[\phi_k(x, y) \right] H(k_x, k_y; z)|_{z=2d} \right\} \tag{4.44}$$

where $\mathbf{F}_{xy}$ and $\mathbf{F}_{xy}{}^{-1}$ denote the two-dimensional spatial Fourier transform and its inverse Fourier transform, respectively, with transform variables, k_x and k_y, known as spatial frequencies. $H(k_x, k_y; z)$ is called the spatial transfer function of propagation of light through a distance z in free space and is defined by [32]

$$H(k_x, k_y; z) = \exp\{-jkz[1 - (k_x^2 + k_y^2)/k^2]^{1/2}\} \exp(jkz) \tag{4.45}$$

An extra term of $\exp(jkz)$ is included in Eq. (4.45) to cancel the phase shift $\exp(jkz)$ which is induced solely by the free-space transmission of distance z. This phase shift has been considered separately and is not included in the calculation of mode $\phi_k'(x, y)$ in Eq. (4.44). If it is further assumed that

$$k_x^2 + k_y^2 << k^2, \tag{4.46}$$

which means that the x and y components o fthe propagation vector of a wave are relatively small, Eq. (4.45) is simplified to

$$H(k_x, k_y; z) = \exp[j(k_x^2 + k_y^2)z/2k]. \tag{4.47}$$

Assumption of Eq. (4.46) is satisfied by most weakly-guiding MMFs. Therefore, Eq. (4.47) is used throughout the dissertation in the calculation of mode profiles with Eq. (4.43).

Note that the mode profile of each mode is broadened by the free-space propagation. In addition, the phase of the mode profile is also changed and the change is dependent on

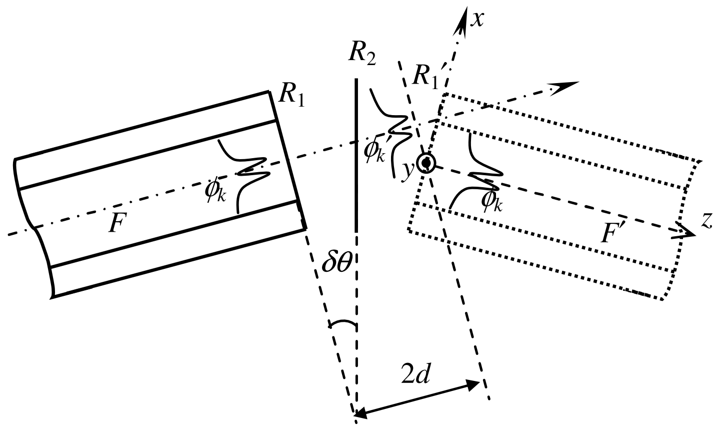

Figure 4.5: Illustration of a MMF-EFPI sensor with a wedge between the two reflection surfaces R_1 and R_2. Fiber F is the mirror image of fiber F' with respect to surface plane R_2.

the spacial parameters x and y, so that the phase-plane of ϕ_k' is deformed from ϕ_k by the free-space propagation. This free-space propagation-induced phase shift and phase plane deformation will introduce a non-zero phase in each of the mode coupling coefficients. As shown later, both the amplitude and phase of the mode coupling coefficients are of great importance in the performance of a MMF-EFPI sensor.

Here I have considered the calculation of mode coupling coefficients for a sensor head in which the two reflection surfaces are perfectly parallel with each other. Same as SMF-EFPI sensors, in practice the two reflection surfaces always show some degree of unparallelism due to the limited fabrication accuracy. The wedge angles between the two reflectors can significantly influence the mode coupling coefficient. Similar to the analysis in Section 2.3.3, it is assumed that reflection surface plane R_1 is perpendicular to the fiber axis z, while reflection surface R_2 is tilted from its original position, forming a wedge angle of $\delta\theta$ with respect to R_1, as shown in Figure 4.2.3. The effect of the angular and lateral misalignment between the lead-in/out fiber F and its mirror image fiber F' caused by the wedge must be considered when we use Eq. (4.43) to calculate the mode coupling coefficient η_k. The effect of the wedge is to produce a linear phase change across the beam and a spatial displacement

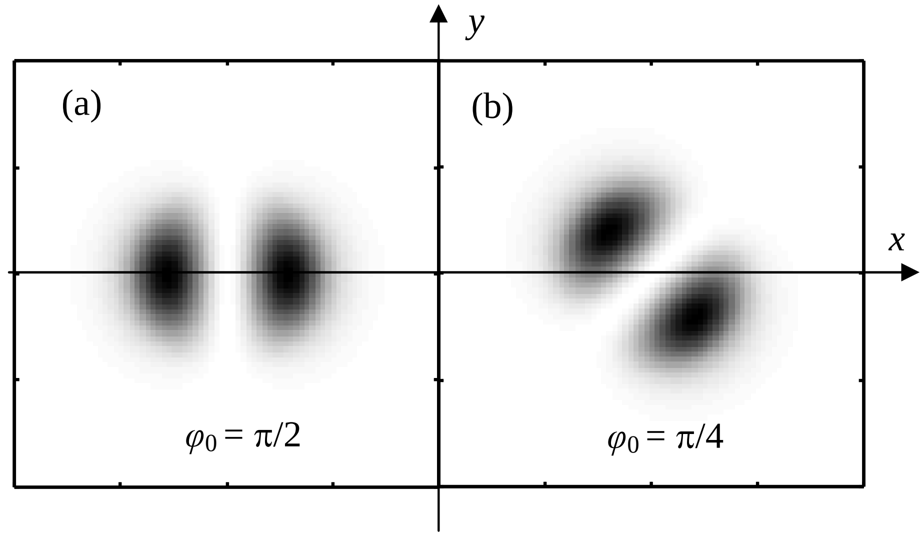

Figure 4.6: Mode field profile of $\mathrm{LP}_{1,1}$ mode of a SI-MMF. $\varphi_0 = \pi/2$, (a); $\varphi_0 = \pi/4$, (b).

between mode ϕ'_k and ϕ_k at the coupling plane R_1 . For mode ϕ'_k that is misaligned by a wedge angle $\delta\theta$, the field can be described by

$$\phi'_{k,\delta\theta}(x, y) = \phi'_k(x - 2d\tan\theta, y)\exp[jk_0 x\tan(2\delta\theta)]. \tag{4.48}$$

Thus mode coupling coefficient η_k is obtained by substituting Eq. (4.48) into Eq. (4.43).

Note that from Eqs. (4.31) and (4.34), the field profiles of the LP modes supported by a weakly-guiding MMF fiber with $\alpha \neq 0$ are not circularly symmetric as the mode field profiles are dependent of the initial azimuthal angle φ_0. This is illustrated in Figure 4.2.3(a) and (b) which show the $\mathrm{LP}_{1,1}$ mode of a SI-MMF calculated by Eq. (4.31) for different initial azimuthal angles of $\varphi_0 = \pi/2$ and $\varphi_0 = \pi/4$, respectively. The two lobes are in different positions at the same x-y reference frame for the two cases. As a result, the mode field has different distributions along a specific direction. Eq. (4.48) indicates that, for a given wedge, for example, the one shown in Figure 4.2.3, its effect is to introduce a phase shift and displacement only along x-direction. Therefore, the effect of the wedge angle is different between the mode fields shown in Figure 4.2.3(a) and (b), even though they represent the same mode. The mode-lobe position effect is further investigated in Section 4.7.

4.2.4 Mode power distribution

So far, we have elaborated on the calculations of the mode profiles ϕ_k, thus the mode coupling coefficient η_k can be obtained by combining Eq.(4.44) and Eq. (4.43). From Eq. (4.29), the mode power distribution (MPD) parameters, $|p_k|^2$, are required before the spectral fringes can be calculated. A uniform MPD is assumed in many reports [20][30]. However, if it is assumed that the mode coupling through the propagation along the MMF is negligible, which may be a reasonable assumption for a fiber length no longer than several hundred meters [34], $|p_k|^2$ may be calculated by the initial conditions and is given by

$$|p_k|^2 = B \left| \int \int_{R'_i} \phi_s \phi_k^* dxdy \right|^2 , \tag{4.49}$$

where ϕ_s is the field profile transmitted to the MMF input plane R_i from the light source that excites the multimode fiber, and B is a normalization coefficient determined by Eq. (4.24).

In our simulation, besides the assumption of the uniform MPD, we also study the case in which the MMF is illuminated by a SMF output, as shown in Figure 4.7. In our simulation, the SMF has a core refractive index of 1.445, a cladding refractive index of 1.440 and a core diameter of 9 μm. There is only one mode, $\text{LP}_{1,1}$ mode (ϕ_0), propagating along the SMF and the calculated mode field diameter, defined by the diameter of the mode profile at which the light intensity drops to $1/e$ of its maximum value, is 10.04 μm. From Eq. (4.49), only those modes with the same azimuthal number as ϕ_0 ($\alpha = 0$ in Eqs. (4.31) or (4.34)) can be excited in the MMF. Thus, only a portion of guided modes are excited. It is worth noting that the modes excited by a SMF output are all circularly symmetric. Therefore, the mode-lobe position effect is not present in this case. The MPD coefficient of each mode, $|p_k|^2$, is given by Eq. (4.49).

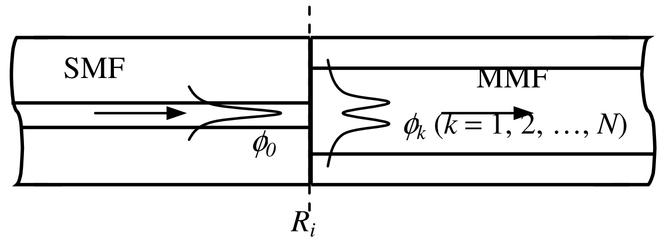

Figure 4.7: Schematic of a multimode fiber illuminated by a single mode fiber output.

4.3 Fringe visibility of SI-MMF-EFPI sensors

Due to its simplicity in the calculation of the mode field profiles, in this section, we take the weakly-guided SI-MMF as an example to analyze the fringe visibility of MMF-EFPI sensors. The effect on the visibility of MMF-EFPI sensors of key parameters including fiber parameters, sensor head structures and imperfections, and MPD of the lead-in/out MMFs, are studied. From Eq. (4.29), the fringe visibility of the sensor, which is defined by Eq. (2.3.1), can be expressed as

$$V_b = \frac{2}{1+\eta_{R_2}}|\eta_{eff}|, \tag{4.50}$$

In this section, first the effect on the fringe visibility of the gap length of a sensor is studied in Subsection 4.3.1. Then the effect of a typical imperfection in a MMF-EFPI sensor, namely, the wedge of the sensor head, is studied theoretically in Subsection 4.3.2. In the analysis, the light wavelength is set to $\lambda = 1.55\ \mu$m. Three different types of weakly-guided SI-MMFs are chosen as the lead-in/out fiber in the MMF-EFPI, the parameters of which are shown in Table 4.1. The fiber parameters of numerical aperture ($\mathtt{NA}$) and V number are defined by

$$\mathtt{NA} = (n_1^2 - n_2^2)^{1/2}, \tag{4.51}$$

and

$$V = 2\pi a(n_1^2 - n_2^2)^{1/2}/\lambda, \tag{4.52}$$

respectively. Fiber 1 has a much larger core diameter ($2a$) than Fiber 2. However their core and cladding refractive indices, n_1 and n_2, are chosen to support the same total LP mode

Table 4.1: Fiber Parameters Used in the Simulation

	Fiber		
Parameters	1	2	3
$2a(\mu\text{m})$	100	50	50
n_1	1.448	1.448	1.448
n_2	1.440	1.416	1.440
NA	0.15	0.30	0.15
V number	30.80	30.68	15.40
N	127	127	33

number N in both fibers. Fiber 3 is chosen to have the same core diameter as Fiber 2 and the same n_1 and n_2 as Fiber 1. Thus Fiber 3 has the same NA as Fiber 1, but a smaller V number and supports much less modes than Fiber 1 and Fiber 2. In the calculation of mode field profiles of these MMFs using Eq (4.31), different selections of φ_0 only lead to a slightly different result of visibility for the above three MMFs (this will be shown in Section 4.7). Therefore, for simplicity, it is assumed $\varphi_0 = \pi/2$ throughout the simulation.

4.3.1 Fringe visibility vs. gap-length

Here an ideal MMF-EFPI sensor, with reflection surfaces R_1 and R_2 perfectly parallel to each other and both perpendicular to the fiber axis z, is assumed. First, we consider the case in which all the propagation modes in the MMFs are equally excited, which leads to $|p_k|^2 = 1/N$ according to Eq. (4.24). The fringe visibility as a function of the gap length for Fibers 1, 2 and 3 is shown in Figure 4.8(a). The fringe visibility for all the three fibers starts from the same maximum (100%) at $d = 0$, and decreases as the gap length increases, with sidelobes appearing at the tail of the curves. However, the visibility of Fiber 2, which has

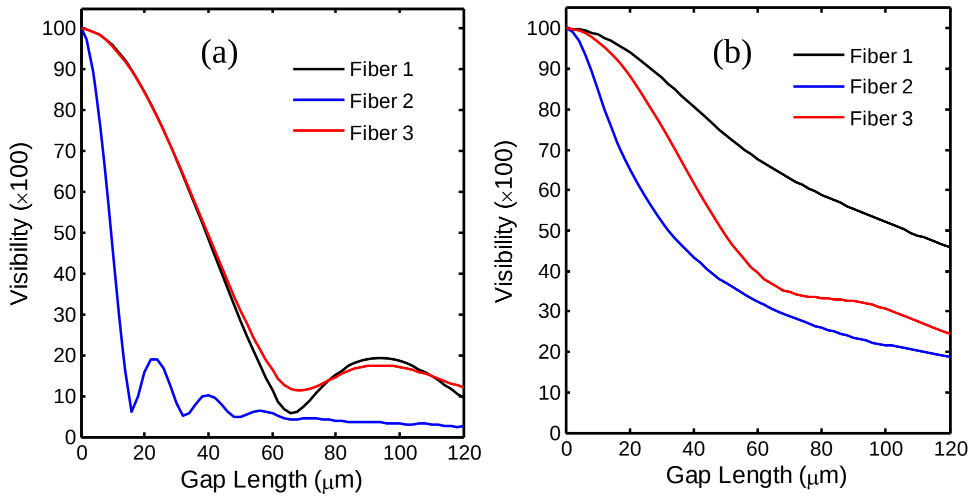

Figure 4.8: Fringe visibility versus gap length for fibers 1, 2 and 3. All modes in the multimode fibers are equally excited, (a); The multimode fibers are illuminated by a single mode fiber output, (b).

a larger NA than fiber 1 and Fiber 3, drops much more quickly down to the first minimum as the gap-length increases to 16 μm. The visibility of Fiber 1 and Fiber 3, which have the same NA, drops to its first minimum almost at the same gap length in spite of their difference in core diameter and the mode numbers. This is in agreement with the conclusion obtained by the geometric-optics theory that the gap length d_{min}, where minimum fringe visibility occurs, is determined by the NA of the fiber; and a smaller NA leads to a larger d_{min} [20].

Next the effect on the fringe visibility of the MPD of the Lead-in/out MMF is considered. Instead of a uniform MPD, we consider the case in which the MMF is illuminated by a SMF output, as illustrated in Section 4.2.4. The light power of the MMF has a heavier distribution on the lower order modes as only $\mathrm{LP}_{0,m}$ modes in the MMF can be excited and the calculated fringe visibility as a function of gap-length is shown in Figure 4.8(b). A comparison of Figure 4.8(b) and (a) shows that, for a given gap length, the MMF-EFPI excited by a SMF has a larger fringe visibility compared to a uniform mode excitation. For example, Fiber 2 illuminated by a SMF output still has a fringe visibility of 71.8% at the gap-length of 16 μm, where it would drop to only 6.0% if all the modes were uniformly excited. Also note that the

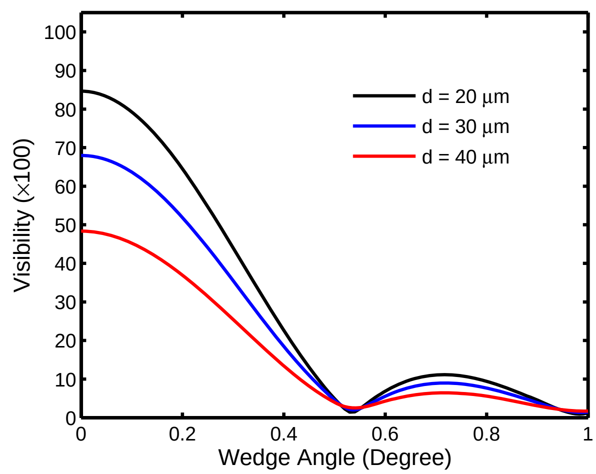

Figure 4.9: Fringe visibility versus wedge angle for fiber 1 at gap length d = 20, 30 and 40 μm. All modes in the multimode fibers are equally excited.

fringe visibility of Fiber 1 drops slower than that Fiber 3 in Figure 4.8(b), while they have almost the same response to the gap-length when all the modes are uniformly excited. This indicates that reducing the number of modes propagating along the fiber is more efficient for larger core fibers to increase the fringe visibility.

4.3.2 Fringe visibility vs. wedge angle

Again it is assumed that all modes supported by the MMF are equally excited in the fiber. The fringe visibility of Fiber 1 as a function of the wedge angle is plotted in Figure 4.9 for different gap-lengths of $d = 20$, 30 and 40 μm. Fringe visibility curve decreases as the wedge angle is increased and it also exhibits sidelobe structures at the tail of the curve. It is also shown that, even with different starting visibilities, the three curves corresponding to various gap-lengths drop to the first minimum, which is around 4%, at the same wedge angle of 0.54°. Thus the effect on the fringe visibility of the wedge angle does not depend on the gap-length. The fringe visibility for the three fibers at selected gap-lengths is plotted in Figure 4.10(a). The gap-lengths used for Fibers 1 and 3 are 30 μm, while 10 μm gap-length

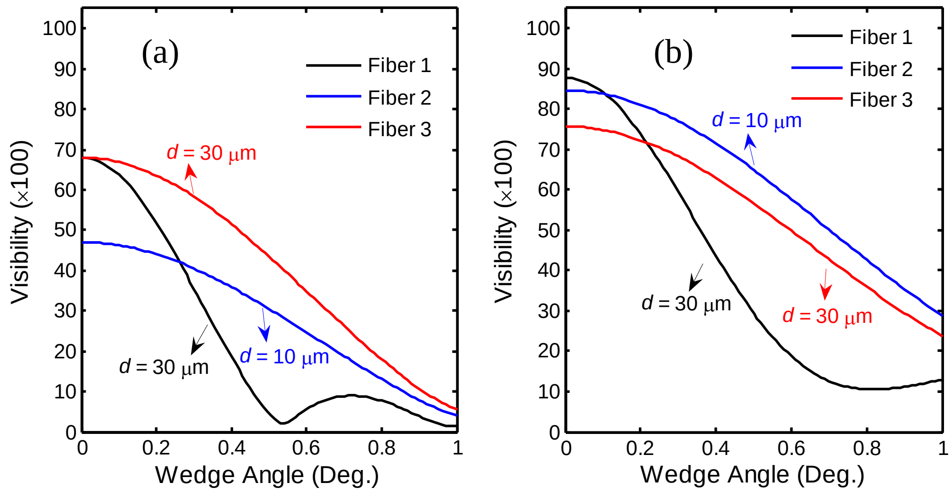

Figure 4.10: Fringe visibility versus wedge angle for fibers 1, 2 and 3. All modes in the multimode fibers are equally excited, (a); The multimode fibers are illuminated by a single mode fiber output, (b).

is used for Fiber 2 in order to clearly show the trend of fringe visibility changes. Apparently, the fringe visibility curve of Fiber 1 drops more quickly than Fibers 2 and 3; while the fringe visibility of Fiber 2 and Fiber 3 shows a similar response to the wedge angles. Thus it is concluded that the sensitivity of fringe visibility to the wedge angle depends on the fiber core diameter. A MMF-EFPI with bigger core diameter fibers is more vulnerable to imperfections on the parallelism of the two cavity reflection surfaces.

Now we consider the case in which the MMF is illuminated by a SMF output. The parameters of the SMF are all the same as those in subsection 4.3.1. The results for Fibers 1, 2 and 3 are shown in Figure 4.10(b) and compared to the result shown in Figure 4.10(a). The comparison shows that even though the fringe visibility is significantly increased at each wedge angle in the case of SMF output excitation, the sensitivity of the fringe visibility to the wedge angle is not significantly effected by the reduction of the modal volume in the sense that the drop rate of the percentage visibility with the increasing wedge angle is almost the same for the two mode power distribution conditions. This is so because the sensitivity is mainly dependent on the spacial spread of the light field. For SI-MMFs, the light field for all the modes spreads all over the fiber core regardless of their mode numbers. Therefore, the fringe visibility sensitivity to the wedge angle is mainly determined by the core size of the MMF.

4.4 Fringe visibility of GI-MMF-EFPI sensors

GI-MMFs are more common and less expensive than their step-index counterpart due to the fact that the MMFs used in optical fiber communications are mostly graded-index owning to their much smaller modal dispersion than SI-MMFs which are important for high-capacity signal transmission. As shown in Section 4.2, the spectral fringes from the MMF-EFPI sensors are independent of the modal dispersion of MMF. However, the fringe visibility of sensors fabricated by GI-MMF is slightly different from those fabricated by SI-MMF with the same core diameter and modal volume owing to the differences between the mode profiles of a SI-MMF and a GI-MMF.

In the simulation, it is assumed that the GI-MMF has an unlimited cladding and its refractive index profile can be described by Eq. (4.33), in which $n_1 = 1.476$, $n_2 = 1.4624$, and $a = 25$ μm. Since $n_1 - n_2 << 1$, the weakly-guiding approximation applies and the mode profile of each LP mode supported by the fiber can be calculated as illustrated in Section 4.2.2. Compared to Fiber 3 in Table 4.1, the core diameter of the GI-MMF (25μm) used in the simulation is the same and the number of the supported modes, which is 30, is also close to Fiber 3. Therefore, the fringe visibility of EFPI sensors constructed by these two MMFs are compared.

Figure 4.11 shows the intensity profiles of the first order mode (LP_{01}) and a higher order mode (LP_{34}) from the GI-MMF and the SI-MMF. The mode profile of the SI-MMF generally has a wider spread than the GI-MMF for modes with the same order numbers. This is more evident for the LP_{01} modes, the profile of which can be approximated as a Gaussian function for both fibers. The mode field diameter of the GI-MMF is much smaller than that of the

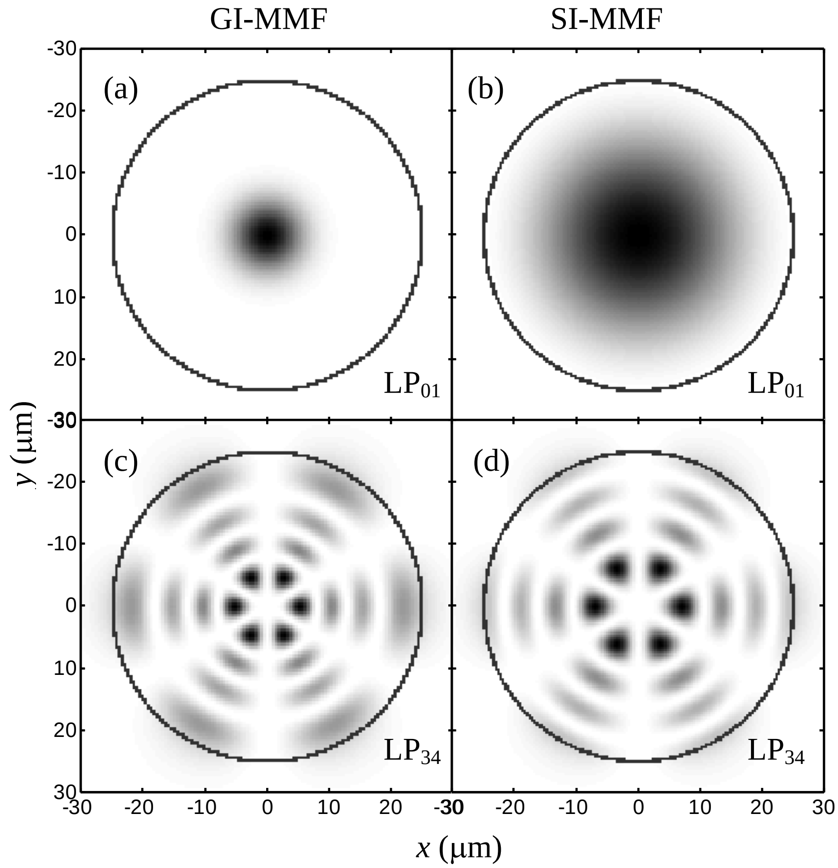

Figure 4.11: The profiles of LP_{01} and LP_{34} modes from the GI-MMF considered here and the SI-MMF of Fiber 3 in Table 4.1.

SI-MMF, as shown in Figure 4.11(a) and (b). In fact, the mode profile of the LP_{01} mode of the GI-MMF is close to that of a standard SMF as shown in Figure 2.3(a), even though the GI-MMF has a much larger core size than the SMF [51][52]. Note that due to the match between these two mode profiles, it is expected that most of the light power is coupled into the LP_{01} mode of the GI-MMF when it is illuminated by a SMF output. For higher order modes, the differences between the mode profiles of the GI-MMF and the SI-MMF are not as evident as for the low order modes.

The fringe visibility as a function of gap-length for the GI-MMF is shown in Figure 4.12(a) for three different mode power distributions. The black curve corresponds to the case where all the modes supported by the fiber are equally excited. Comparing to the

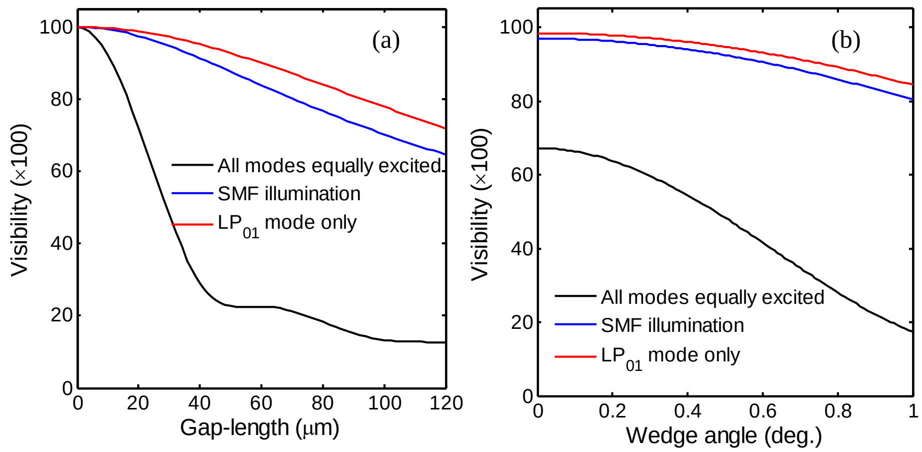

Figure 4.12: Fringe visibility versus gap-length,(a), and wedge angle (b) for the GI-MMF at three different mode field distributions.

case of Fiber 3 as shown in Figure 4.8(a) (red curve), the fringe visibility of the GI-MMF-EFPI sensor is slightly degraded in the sense that the first minimum of the visibility occurs at gap-length $d \approx 45$ μm, while the fringe visibility of the SI-MMF-EFPI sensor reaches its first minimum at $d \approx 65$ μm, which is much larger. Another difference is that the sidelobe structure is less evident for the GI-MMF case than for the SI-MMF case. The blue curve in Figure 4.12(a) is the case that the fiber is illuminated by a SMF output, the visibility sensitivity to the gap-length for the GI-MMF is much smaller than for the SI-MMF. For example, the visibility for the GI-MMF is still as large as 65% at gap-length $d = 120$ μm, while the visibility for Fiber 3 decreases to 25% for the same gap-length as shown in Figure 4.8(b). This is because, as mentioned earlier, most of the light power is coupled to LP_{01} mode of the GI-MMF when it is illuminated by the SMF output, therefore, the number of the excited modes is much less than the case of the SI-MMF. The dominance of LP_{01} mode excitation in the GI-MMF when illumniated by the SMF output can be confirmed by the small difference in the fringe visiblity curves between the cases of “SMF illumnation” and “LP_{01} mode only” in Figure 4.12(a).

For the unparallelism imperfection of the sensor head, Figure 4.12(b) plots the visibility as a function of wedge angles at gap-length $d = 30$ μm for the three abovementioned MPDs.

In the case of all the modes supported by the MMFs are equally excited, the fringe visibility for the GI-MMF is less sensitive to the wedge angle variations than for the SI-MMF of Fiber 3 as shown in Figure 4.10 (red curve). For example, the fringe visibility drops to 18% at the wedge angle of 1° for the GI-MMF case, while the visibility is only 5% at the same wedge angle for the SI-MMF case. However, the sensitivity to wedge angles is significantly reduced in cases where the GI-MMF is illuminated by a SMF output and only LP_{01} mode is exited. This is expected because, as shown in Section 4.9, the fringe visibility sensitivity to the wedge angle is mostly related to the spacial spread of light field in the fiber and the light field of LP_{01} mode in the GI-MMF is confined to a small area in the core, therefore the sentivity is reduced. Actually, the visiblity sensitivity to the wedge angle for the GI-MMF case when only LP_{01} mode is excited is similiar to the SMF case as shown in Figure 2.7.

In summary, the simulation results show that when the modes supported by the MMF are all equally excited, the fringe visibility of a GI-MMF-EFPI sensor is close to a SI-MMF-EFPI sensor the MMF of which has the same number of modes and core size. However, if the GI-MMF is illuminated by a SMF output or only the LP_{01} mode is excited, the fringe visibility is similar to that of a SMF-EFPI sensor.

4.5 SMF-EFPI and MMF-EFPI sensors Comparison

In this section, theoretical results of MMF-EFPI sensors are compared to SMF-EFPI sensors in terms of fringe visibility variations related to gap-lengths changes and sensor imperfections. The analysis presented in Section 4.3 has shown that the fringe visibility of a MMF-EFPI sensor is much more sensitive to the gap-length and the unparallelism of the two reflectors in the FP cavity compared to that of a SMF-EFPI sensor. For example, the fringe visibility of a perfect MMF-EFPI sensor fabricated by a MMF with core size 100 μm and $\mathtt{NA} = 0.15$ quickly reduces to 10% when the gap-length is as small as 60 μm at wavelength 1550 nm if all the modes supported by the fiber are equally excited (see Figure (4.8)). The fringe visibility reduces even more quickly for a MMF with a smaller core-size. However, a perfect SMF-EFPI sensor constructed by a standard SMF still has a visibility of 80% when the gap-length increases to 100 μm at the same wavelength (see Figure (2.6)). The requirement for the parellelism of the two reflectors in the FP cavity is also much more stringent for a MMF-EFPI sensor than for a SMF-EFPI sensor. The fringe visibility of the 100 μm core MMF-EFPI sensor reduces to its first minimumm ($\approx 5\%$) when the second reflector is tilted by an angle of only 0.55° with respect to the first reflector. However, a SMF-EFPI fiber with a gap-length of 20 μm still maintains its visibility above 35% even when the wedge angle is as large as 5°. This situation suggests that a MMF-EFPI sensor require a much more stringent fabrication accuracy and have less freedom of gap-length selections in order to achieve a similar visibility performance as that of a SMF-EFPI sensor. The fiber end-face processed by a commercially available fiber cleaver, which usually has an average angle of about 1° with respect to the plane vertical to the fiber axis, might not be adequate to function as a reflector for a MMF-EFPI sensor with reasonable fringe visibility. The previous analysis has assumed that the light wavelength is 1550 nm, while the popular CCD-based spectrometers in today's market are all designed for wavelengths below 1000 nm. When the wavelength is reduced, the fiber supports more modes. For example, the V number of a fiber is almost doubled when the wavelength is changed from 1550 to 850 nm and the number of modes supported by the fiber will be quadrupled as it is proportional to the square of the V number. This will lead to a much stronger sensivity to gap-length changes. Therefore, one key issue in the wide spread use of MMF-EFPI sensors is to develop high-accuracy and low cost sensor fabrication methods so that sensors with desired fringe visibility can be mass-produced.

4.6 Mechanisms limiting the performance of MMF-EFPI sensors

In order to understand the fundamental mechanism that limits the fringe visibility of a MMF-EFPI sensor and its essential difference from a SMF-EFPI sensor under the modal theory, Eqs. (4.22) and (2.16), which describe the fringe patterns output from a SMF-EFPI and a MMF-EFPI sensor, respectively, are rewritten to (with a little modification)

$$I_{SMF} = 1 + |\eta_1| \cos(4\pi d/\lambda + \pi - \theta_1); \tag{4.53}$$

and

$$I_{MMF} = 1 + \frac{2}{1+\eta_{R_2}} \sum_{k=1}^{N} |p_k|^2 |\eta_k| \cos(4\pi d/\lambda + \pi - \theta_k). \tag{4.54}$$

Eq. (4.53) is for the SMF-EFPI sensor and Eq. (4.54) is for the MMF-EFPI sensor. Recall that, in the above equations, d is the gap-length, λ is the wavelength, $|p_k|^2$ represents the modal power distribution, η_{R_2} is the power coupling coefficient of the the lead-in fiber from an identical fiber placed at a distance of $2d$, and η_k is the complex coupling coefficient between the mode k propagating along $-z$ direction and the same mode propagating along $+z$ direction but reflected back by the second reflector of the F-P cavity. The coupling occurs at the first reflector of the F-P cavity. Note that $k = 1, 2, ..., N$ for MMF-EFPI sensors, where N is the mode number in the MMF, and $k = 1$ for SMF-EFPI sensor, where only one mode is present. In Eq. (4.54), $|p_k|^2$ is related to the MPD in the MMF; We have assumed $\eta_k = |\eta_k| \exp(i\theta_k)$. Therefore θ_k is defined as the *coupling-induced phase-shift* of mode k. For convenience, we define $|\eta_k|$ as *the amplitude coupling coefficient* of mode k.

A comparison of Eqs. (4.53) and (4.54) shows that, a significant difference between a SMF-EFPI sensor and a MMF-EFPI sensor is that the visibility of a SMF-EFPI sensor is only dependent on the amplitude coupling coefficient, while both the amplitude coupling coefficient and the coupling-induced phase-shift play important roles in the visibility performance of a MMF-EFPI sensor. The second term of Eq. (4.54) is a superposition of N

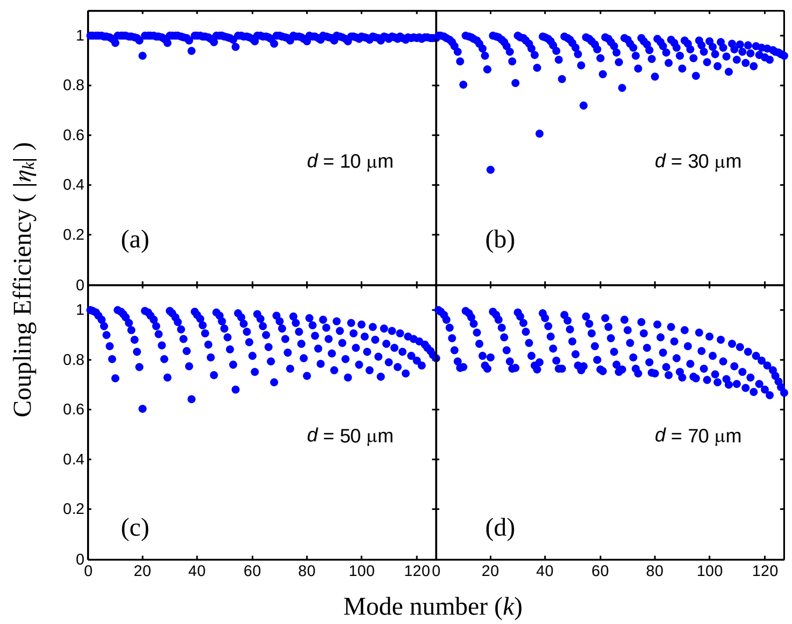

Figure 4.13: Amplitude coupling coefficient of all modes in the fiber for perfect MMF-EFPI sensors at different gap-lengths.

cosine waves with different phase θ_k and weighed by factors that are related to the amplitude coupling coefficients and the MPD coefficients. Constructive and destructive interferences between the cosine waves, which depend on the relationship between their phases of θ_k, might occur. Obviously, the destructive interference causes a reduction in the fringe visibility of a MMF-EFPI sensor.

In order to illustrate the different effects of the amplitude coupling coefficient and the coupling-induced phase-shift on the fringe visibility of a MMF-EFPI sensor, Fiber 1 in Table 4.1, which has a core radius of 50 μm, a `NA` of 0.15, and supports $N = 127$ LP modes at wavelength 1550 nm, is chosen as an example. The mode order number k is counted in such a way as $k = 1$ for $LP_{0,1}$ mode, ..., $k = 10$ for $LP_{0,10}$ mode, $k = 11$ for $LP_{1,1}$ mode, $k = 12$ for $LP_{1,2}$ mode, ..., and $k = 127$ for $LP_{26,1}$ mode. The case of a perfect sensor (wedge angle = 0) is first considered. Figures 4.13 and 4.14 show the amplitude coupling coefficient and the coupling-induced phase-shift of all the modes in the fiber for sensors with different gap-lengths. A comparison between Figures 4.13(a), (b), (c) and (d) indicates that,

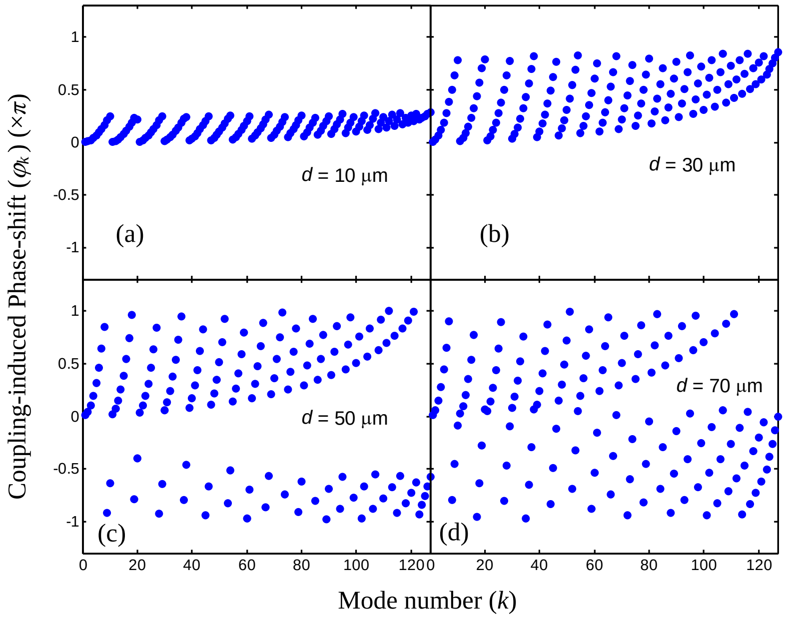

Figure 4.14: Coupling-induced phase-shift of all modes in the fiber for perfect MMF-EFPI sensors at different gap-lengths.

although the average amplitude coupling efficiency decreases as the gap-length increases, generally speaking, the amplitude coupling coefficient is not sensitive to the gap-length variations. Most ($\approx 80\%$) modes maintain their amplitude coupling coefficients above 80% for gap-lengths used in the simulations. Figure 4.14 reveals that it is the dependence of the coupling-induced phase-shift on the gap-length that is responsible for the quick reduction of the fringe visibility as the gap-length increases. At small gap-lengths, the coupling-induced phase-shifts of all the modes are distributed in a small portion of range $[-\pi, +\pi]$. Therefore the interference among all the modes are generally constructive. As shown in Figure 4.14 (a), (b), (c), and (d), when the sensor has a gap-length of 10 μm, the coupling-induced phase-shift is roughly uniformly distributed in the range $[0, 0.3\pi]$; As the gap-length increases to 30 μm, the distribution range expands to $[0, 0.8\pi]$; the coupling-induced phase-shift is in the range $[-\pi, 0]$ for approximately one third of the modes when the gap-length increases to 50 μm, at which the destructive interference between some of the modes has occured; Finally, more modes will show in the $[-\pi, 0]$ range when the gap-length is 70 μm; The coupling-

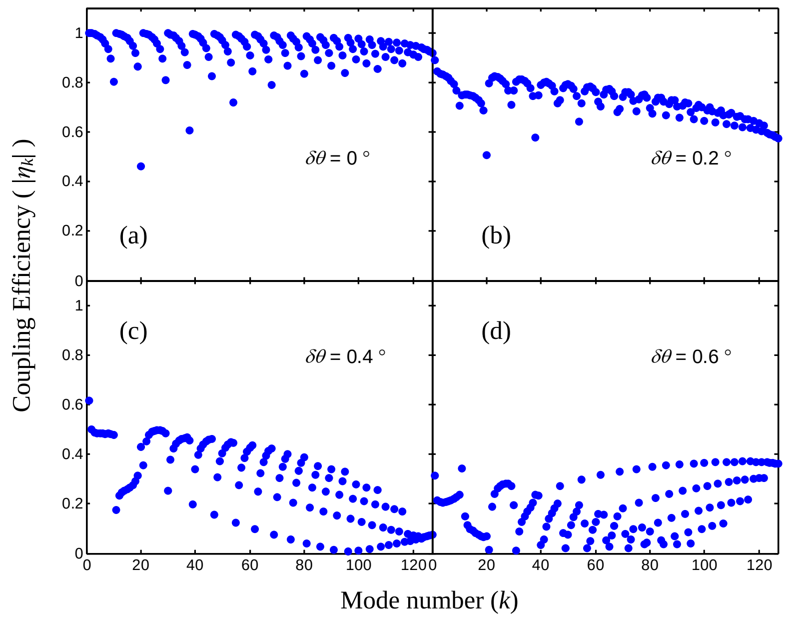

Figure 4.15: Amplitude coupling coefficient of all modes in the fiber for MMF-EFPI sensors at different wedge angle. The gap-length is 30 μm.

induced phase-shift is roughly uniformly distributed in the range of $[-\pi, +\pi]$. Therefore the constructive and destructive interference among all the modes in general cancel each other and the fringe visibility of the sensor is minimum.

The visibility reduction owing to wedge angles is studied in a similar way. The amplitude coupling efficient and the coupling-induced phase-shift of all the modes for a sensor with a gap-length of 30 μm at different wedge angles are plotted in Figures 4.15 and 4.16, respectively. It is shown that the average amplitude coupling coefficient of all the modes decreases quickly when the wedge angle increases from 0 to 0.4° (see Figure 4.15(a), (b), (c)). However, the coupling-induced phase-shift is not sensitive to the wedge angle variations in this range. From Figure 4.16(a), (b), and (c), the distributions of coupling-induced phase-shift are similar, and are roughly uniform in the range $[0, \pi]$. However, as the wedge angle further increases, the decrease of the average amplitude coupling coefficient becomes slower (see Figure 4.15(d)) and the coupling-induced phase-shift starts to be responsible for the visibility reduction as its distribution range expands to $[-\pi, 0]$ (see Figure 4.16(d)).

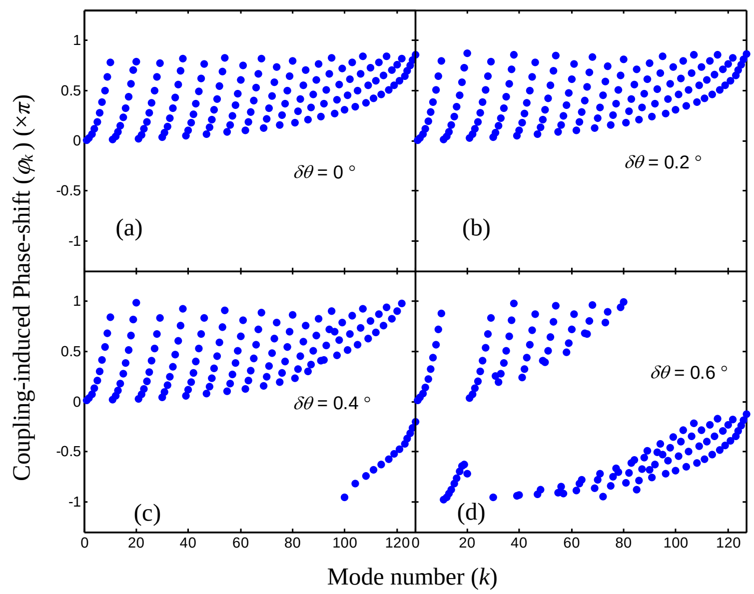

Figure 4.16: Coupling-induced phase-shift of all modes in the fiber for MMF-EFPI sensors at different wedge angle. The gap-length is 30 μm.

4.7 Mode-lobe position effect

As mentioned in Section 4.2.3, depending on the mode-lobe positions, a given wedge angle might have different effect to a circularly non-symmetric mode of a MMF in the calculation of the mode coupling coefficient. In this section, this effect is analyzed for two types of MMFs. The first is the conventional MMFs that support a large number of modes and the second is the MMFs that only support two lowest order modes.

4.7.1 Conventional MMFs

As an example, the Fiber 1 in Table 4.1 which supports 127 LP modes at wavelength 1550 nm is considered. It is assumed that the MMF-EFPI sensor has a wedge angle of 0.4° and a gap-length of 50 μm. The mode field profiles are obtained from Eq. (4.31). Figure 4.17(a) shows the amplitude mode coupling coefficient as a function of the initial azimuthal angle φ_0 for different circularly non-symmetric modes of $\mathrm{LP}_{\alpha,m}, (\alpha = 1, 2, ..., \text{ and } m = 1, 2, ...)$.

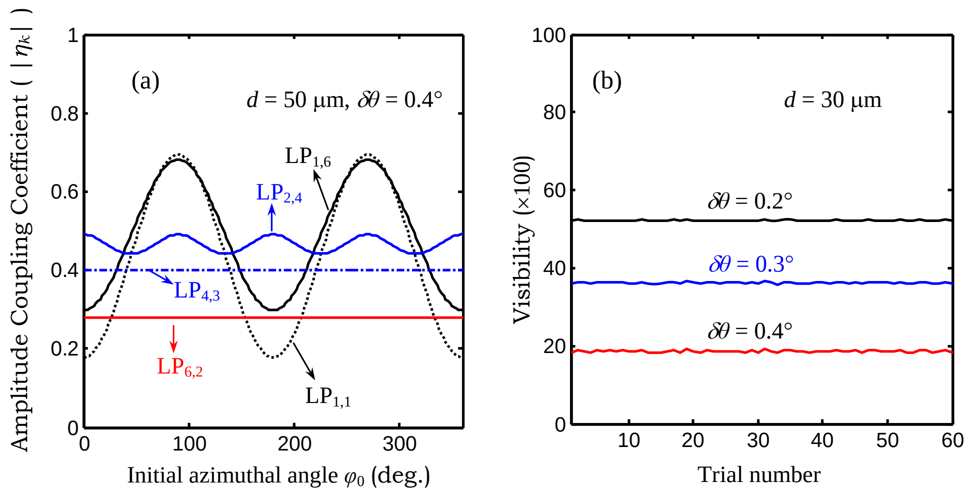

Figure 4.17: Mode coupling coefficients of different modes as a function of initial azimuthal angle φ_0, (a); and visibility of the MMF-EFPI sensor when all modes in the MMF is equally excited and the initial azimuthal angle φ_0 of each mode is randomly chosen from [0, 360°] at each trial, (b).

The amplitude mode coupling coefficient can also be viewed as the fringe visibility of the MMF-EFPI sensor when only the corresponding mode is excited in the MMF. It is clear that the mode-lobe position effect is most evident for the modes with $\alpha = 1$ and rapidly wears out as α number increases. For example, the peak-to-peak variations of the amplitude mode coupling coefficients are 0.52 and 0.38 for $LP_{1,1}$ and $LP_{1,6}$ modes, respectively. While the peak-to-peak variations decrease to 0.05 for $LP_{2,4}$ mode and become invisible in the figure for those modes with $\alpha \geq 4$.

In practice, the number of excited modes in a conventional MMF of a MMF-EFPI sensor is usually large. In order to investigate the overall effect of the mode-lobe positions on the fringe visibility of a MMF-EFPI sensor, it is assumed that the modes supported by the MMF are all equally excited and the initial azimuthal angles φ_0 of all the modes are uncorrelated and each of them is uniformly distributed in the range of [0, 360°]. Figure 4.17(b) shows the fringe visibility of a MMF-EFPI sensor with a gap-length of d = 30 μm for 60 simulation trials at wedge angles of $\delta\theta$ = 0.2°, 0.3°, and 0.4°. Each simulation trial uses a different set of initial azimuthal angles φ_0 for all the modes each of which is randomly selected from [0, 360°]. It is clear that the variations of the fringe visibility increase as the wedge angle becomes larger. However, the standard deviations of the variations are all small ($< 0.5\%$ for all three cases). Therefore, it is concluded that the fringe visibility of such a MMF-EFPI sensor is not sensitive to the mode-lobe positions. There are two reasons that are responsible for the insentivity to mode-lobe positions of such a sensor. The first is that only the modes with $\alpha = 1$ are sensitive to mode-lobe positions and these modes only constitute a small portion of the modes that are excited in the fiber. The second is that even for those modes with $\alpha = 1$, the mode-lobe effect on these modes partially cancels each other as the initial azimuthal angles φ_0 for all these modes are uncorrelated and uniformly distibuted in the range of [0, 360°].

4.7.2 Two-mode MMFs

As the number of the modes supported in a MMF decreases, the mode-lobe position effect on the fringe visibility of the MMF-EFPI sensor might become significant. Here the case that the MMF only supports the two lowest order modes which are the LP_{01} and LP_{11} modes is considered. The analysis is also practically important because in the 850 nm wavelength window which is also the working wavelength range of the most popular CCD-based spectrometers, the conventional standard SMFs start to support the two abovementioned modes as these fibers usually have cutoff wavelengths larger than 850 nm (around 1200 nm).

In the simulations, a conventional SMF (Corning SMF-28) which works at wavelength $\lambda = 850$ nm is considered. The parameters of the fiber are $a = 4.5$ μm, $n_1 = 1.448$, and $n_2 = 1.444$. The V-number of the fiber is 3.99, therefore it supports the two lowest order modes (LP_{01} and LP_{11}). It is assumed that the two modes are equally excited. Figure 4.18(a) shows the fringe visibility of a sensor with gap-length $d = 50$ μm as a function of the initial azimuthal angle φ_0 of $LP_{1,1}$ mode at wedge angles of $\delta\theta = 0.2°$, $0.5°$, and $1°$. The mode-lobe position effect on the fringe visibility is evident especially when the wedge angle is large. For

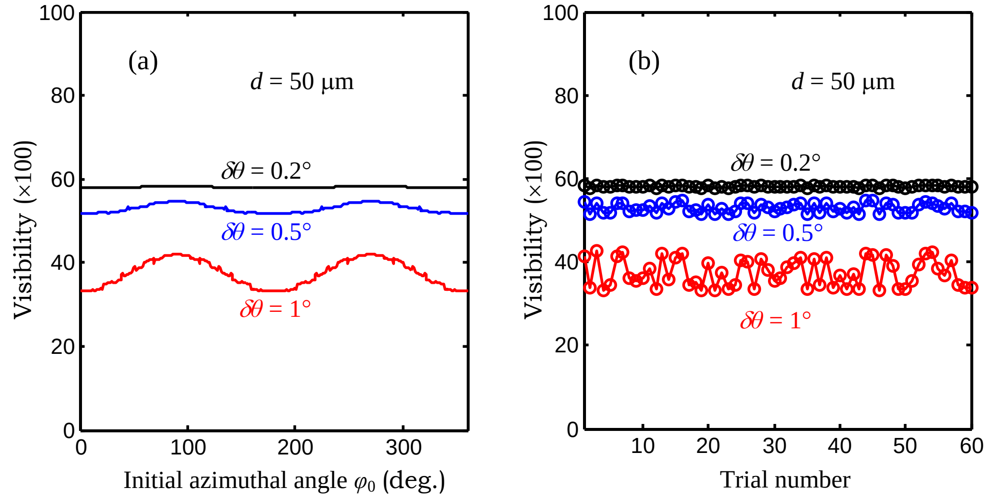

Figure 4.18: Fringe visibility as a function of the initial azimuthal angle φ_0 of $LP_{1,1}$ mode, (a); and fringe visibility when the initial azimuthal angle φ_0 of $LP_{1,1}$ mode is randomly chosen from [0, 360°] at each trial, (b).

example, the peak-to-peak variations of fringe visibility is almost 10% for the wedge angle of 1°. To simulate such a fiber with randomly changed mode-lobe positions, Figure 4.18(b) shows the fringe visibility of 60 simulation trial for each of the same three wedge angles, in which initial azimuthal angle φ_0 of $LP_{1,1}$ mode is randomly chosen from [0, 360°] for each trial.

Different from a conventional MMF, the $LP_{1,1}$ mode, which is most sensitive to the mode-lobe position effect, could carry significant power in a two-mode fiber. The mode-lobe position is not stable in such a fiber. For example, it can be changed simply by touching the fiber. As many EFPI sensor systems use the standard SMF and the light sources of 850 nm, special care must be taken to suppress the $LP_{1,1}$ mode to achieve stable spectral fringes in practice.

The above analysis has assumed that a specific circularly non-symmetric mode whose profile is described by Eq (4.31) has a fixed azimuthal phase of φ_0. This might be the case if the MMF is excited by a light source with a spatial coherence length much larger than the size of the fiber core. However, if a spatially incoherent or semi-coherent light source whose spatial coherence length is much smaller than the size of the fiber core, such as a light-emitting diode (LED) or a thermal light, the same LP mode with different initial azimuthal phases can be independently excited at the same time. In such a case the visibility fluctuations caused by the mode-lobe effect can be significantly reduced as lobes average and the power of the mode is distributed more uniformly over the fiber cross-section.

4.8 Mode-mixing effect

As described in Section 4.2.1, in a MMF-EFPI sensor, a particular mode reflected by surface R_1 can only couple its power to the same mode that transmits along the $-z$ direction in the lead-in/out fiber. However, the same mode reflected by the surface R_2 can couple its power to the modes with different mode numbers owing to the separation between the two reflection surfaces. On the other side, a particular mode transmitting along $-z$ have contributions from different modes that are reflected by surface R_2. There mode-mixing occurs. The analysis in Section 4.2.1 has assumed that the contributions to specific mode from modes with different mode numbers are negligible because their interferences with the reflection from the surface R_1 tend to cancel out owing to the random phase relationship between different modes. Apparently, it has been assumed that the mode number is sufficiently large so that the perturbations to the fringe visibility owing to the mode-mixing effect is negligible. In many cases, this mode-mixing effect cannot be ignored and it is analyzed in this section,

The equation that describes the spectral fringes of a MMF-EFPI sensor with the consideration of the mode-mixing effect is Eq. (4.22), which is rewritten here:

$$\begin{aligned} I &= \sum_{k=1}^{N}(|p_k|^2 + |\eta_k|^2|p_k|^2 + |c_k|^2) + 2\sum_{k=1}^{N}|\eta_k||p_k||c_k|\cos(\theta_k' - \theta_k - \varphi_k) \\ &\quad +2\sum_{k=1}^{N}|p_k||c_k|\cos(\phi_0 - \theta_k' + \varphi_k) + 2\sum_{k=1}^{N}|\eta_k||p_k|^2\cos(\phi_0 - \theta_k). \end{aligned} \tag{4.55}$$

The definitions of parameters η_k, p_l, ϕ_0, and c_k can be found in Eqs. (4.16)−(4.19). As an example, a MMF-EFPI sensor that is constructed by Fiber 3 in Table 4.1 is considered. It is further assumed that all modes supported by the MMF are excited. As shown in Table 4.1, the MMF supports 33 LP modes. However, it must be noted that LP modes are not really true modes; rather they are "pseudo" modes constructed by "degenerate" HE and EH modes. The relationships of the $\mathrm{LP}_{\alpha,m}$ modes with the conventional modes are [33]

$$\begin{cases} \mathrm{LP}_{0,m}: & \mathrm{HE}_{1,m} \\ \mathrm{LP}_{1,m}: & \mathrm{TE}_{0,m}, \mathrm{TM}_{0,m}, \mathrm{HE}_{2,m} \\ \mathrm{LP}_{\alpha,m}: & \mathrm{HE}_{\alpha+1,m}, \mathrm{EH}_{l-1,m}. \end{cases} \tag{4.56}$$

Moreover, each mode with $\alpha \neq 0$ has the degeneracy of order two due to the freedom to choose two orthogonal initial phases of φ_0 in Eq (4.31) (for example, $\varphi_0 = 0$ and $\varphi_0 = \pi/2$ represent two independent modes). Considering that the Fiber 3 support 5 $\mathrm{LP}_{0,m}$ $(m = 1, 2, 3, 4, 5)$ modes, 4 $\mathrm{LP}_{1,m}$ $(m = 1, 2, 3, 4)$, and 24 other LP modes, the number of the conventional modes it supports is $5 \times 1 + 4 \times 6 + 24 \times 4 = 125$. As the mode-mixing effect is very sensitive to the number of modes that is excited in the MMF, in the case that the modes in the MMF is fully excited, it should be more meaningful to use the number of the conventional modes. In order to illustrate the mode-mixing effect, it is assumed in the simulation that the phases of all the modes are independent on each other and the phase, $\phi_k' - \varphi_k$, is uniformly distributed in the phase range of $[-\pi, \pi]$. To simulate the 125 conventional modes in the MMF, Eq. (4.55) is modified to

$$\begin{aligned} I &= \sum_{k=1}^{N}(|p_k|^2 + |\eta_k|^2|p_k|^2 + |c_k|^2) + 2\sum_{k=1}^{N}|\eta_k||p_k||c_k|\cos(\theta_k' - \theta_k - \varphi_k) \\ &\quad +2\sum_{k=1}^{N}\sum_{n=1}^{q(k)}\frac{1}{q(k)}|p_k||c_k|\cos(\phi_0 - \theta_{k,n}{}' + \varphi_{k,n}) \\ &\quad +2\sum_{k=1}^{N}|\eta_k||p_k|^2\cos(\phi_0 - \theta_k). \end{aligned} \tag{4.57}$$

where

$$q(k) = \begin{cases} 1, & \mathrm{LP}_{0,m} \quad (k = 1, 2, \cdots, 5) \\ 6, & \mathrm{LP}_{1,m} \quad (k = 6, 7, \cdots, 9) \\ 4, & \mathrm{LP}_{1,m} \quad (k = 10, 11, \cdots, 33) \end{cases}; \tag{4.58}$$

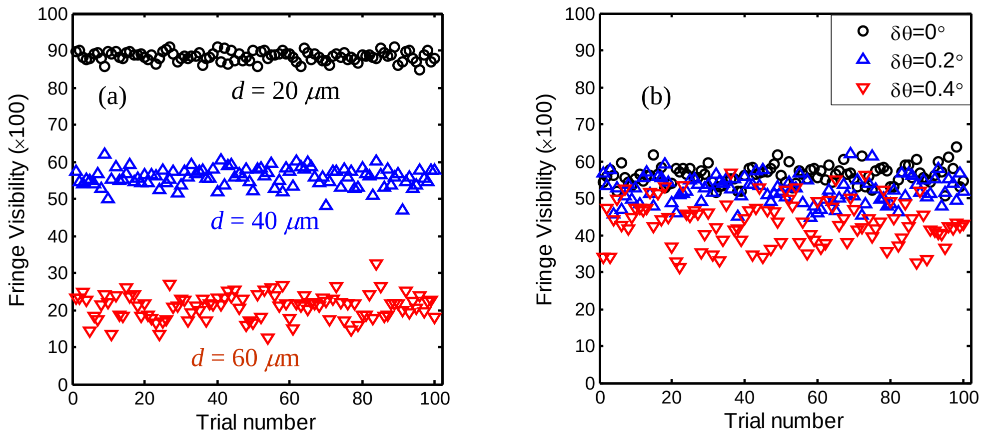

Figure 4.19: Fringe visibility fluctuations caused by mode-mixing effect in a MMF-EFPI sensor.

The phases terms, $\phi_k' - \varphi_k$ and $\phi_{k,n}' - \varphi_{k,n}$, are randomly picked from range $[-\pi, \pi]$ for each k and for each trial of simulation; And $|p_k| = 1/N$ is used because of the assumption that all modes are equally excited.

Figure 4.19(a) shows the fringe visibility fluctuations of 60 simulation trials owing to the mode-mixing effect for a MMF-EFPI sensor constructed by Fiber 3 for gap-lengths of 20, 40, and 60 μm. It is assumed that the two reflection surfaces of the FP cavity in the sensor head is parallel to each other. It is evident that as the gap-length increases, the fringe visibility fluctuations become larger. This is so because more power of a mode transmitting along $-z$ direction in the MMF is from modes with different mode numbers reflected by surface R_2. Therefore, the mode-mixing effect is more significant. The calculated standard deviations are 1.3%, 2.4%, and 3.6% for gap-lengths of 20, 40, and 60 μm, respectively.

Figure 4.19(b) is the result for the case that the FP reflection surfaces of the MMF-EFPI sensor have wedge angles. The gap-length of the sensor remains 40 μm for all wedge angles. The fringe fluctuations become larger as mode-mixing becomes more significant when the wedge angle increases. The calculated standard deviations are 2.8%, 4.2%, and 5.5% for wedge-angles of 0°, 0.2°, and 0.4°, respectively. The standard deviations for the gap-length of 40 μm and the zero wedge angle calculated in Figure 4.19(a) and (b) are slightly different

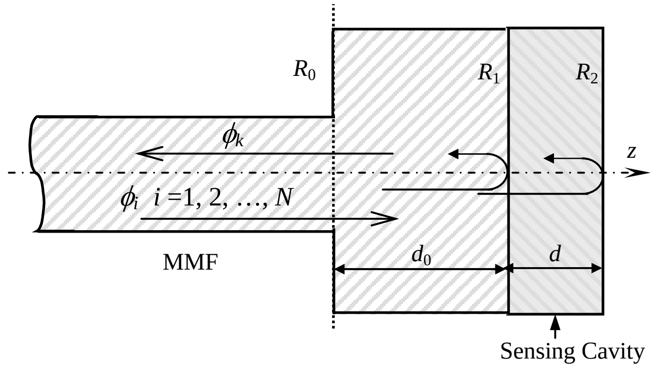

Figure 4.20: A general configuration of MMF-EFPI sensors: the FP cavity is illuminated by a MMF.

(2.4% vs. 2.8%). This is because different sets of randon numbers are used in these two cases.

4.9 FP cavity illuminated by a MMF

The mathematical model used in previous analysis has assumed that one of the two surfaces of the sensing FP cavity is the end-face of the MMF which is perpendicular to the fiber axis. This assumption greatly simplifies the analysis as modes with different mode numbers have no coupling at the reflection of this end-face. However, many MMF-EFPI sensors do not use the fiber end-face to form the FP cavity. The MMF is used only as a lead-in/out fiber to deliver the light to and collect the reflected light from a separate FP cavity which is placed close or at a distance to the MMF end. A more general MMF-EFPI sensor configuration is shown in Figure 4.20, in which each mode in the MMF propagates in a free-space of optical distance d_0 before it reaches the sensing FP cavity with optical thickness d. Examples of such a configuration include thin polymer films as FP sensing interferometers illuminated by MMFs for the detection of acoustic and thermal signals [53][54][55][56] and sapphire diaphragms illuminated by sapphire fibers for extremely high temperature measurement [8]. The previous configuration of using the end-face of the MMF as an reflection surface can be considered as a special case of $d_0 = 0$ in the configuration shown in Figure 4.20. Therefore, theoretical analysis of such sensor configurations is of great interest not only for the fabrication and application of such sensors, but also for a more general modal theory of MMF-EFPI sensors.

4.9.1 Spectral fringe representation

Similar to the analysis in Section 4.2.1, it is assumed that the MMF supports N eigenmodes ($\phi_i,\ i = 1, 2, \cdots, N$). Each mode that propagates along $-z$ direction in the MMF arises from the reflections of surfaces R_1 and R_2. For example, we consider the k^{th} mode (ϕ_k) propagating along $-z$ direction in the fiber. Not only the k^{th} mode, but also any other mode that propagate along $+z$ direction in the fiber could contribute to mode ϕ_k after they are reflected back by surfaces R_1 and R_2 as both of these two surfaces have a distance to the fiber end. Therefore, the k^{th} mode propagating along $-z$ direction in the MMF can be expressed as

$$q_k\phi_k = \sum_{l=1}^{N} p_l\xi_{lk}\phi_k \exp[-j(4\pi d_0/\lambda)] + \sum_{l=1}^{N} p_l\zeta_{lk}\phi_k \exp[-j(4\pi d_0 + d/\lambda) + \pi], \tag{4.59}$$

in which p_i is related to the mode power distribution; ξ_{lk} and ζ_{lk} are the coupling coefficients to the k^{th} mode propagating along $-z$ direction of the l^{th} mode propagating along $+z$ direction that is reflected by surfaces R_1 and R_2, respectively; $4\pi d_0/\lambda$ and $4\pi(d_0 + d)/\lambda$ are phase shifts related to the free space transmission of distances d_0 and $d_0 + d$, respectively, while the extra phase shift π arises from the reflection of light incident from an optically less dense medium to an optically denser medium. Similar to the derivation of Eq. (4.21), the light intensity of the k^{th} mode can be expressed as

$$\begin{aligned} I_k &= \langle q_k q_k^* \rangle \\ &= \langle \left\{ \sum_{l=1}^{N} p_l \xi_{lk} \exp[-j(4\pi d_0/\lambda)] + \sum_{l=1}^{N} p_l \zeta_{lk} \exp\{-j[(4\pi(d_0+d)/\lambda]\} + \pi] \right\} \\ &\quad \times \left\{ \sum_{l=1}^{N} p_l^* \xi_{lk}^* \exp[j(4\pi d_0/\lambda)] + \sum_{l=1}^{N} p_l^* \zeta_{lk}^* \exp\{j[4\pi(d_0+d)/\lambda + \pi]\} \right\} \rangle \\ &= \left(\sum_{l=1}^{N} p_l \xi_{lk} \right) \left(\sum_{l=1}^{N} p_l^* \xi_{lk}^* \right) + \left(\sum_{l=1}^{N} p_l \zeta_{lk} \right) \left(\sum_{l=1}^{N} p_l^* \zeta_{lk}^* \right) \\ &\quad + \left(\sum_{l=1}^{N} p_l \xi_{lk} \right) \left(\sum_{l=1}^{N} p_l^* \zeta_{lk}^* \right) \exp[j(4\pi d/\lambda + \pi)] + c.c \\ &= \sum_{l=1}^{N} \sum_{m=1}^{N} p_l p_m^* \xi_{lk} \xi_{mk}^* + \sum_{l=1}^{N} \sum_{m=1}^{N} p_l p_m^* \zeta_{lk} \zeta_{mk}^* \\ &\quad + \sum_{l=1}^{N} \sum_{m=1}^{N} p_l p_m^* \xi_{lk} \zeta_{mk}^* \exp[j(4\pi d/\lambda + \pi)] + c.c.. \end{aligned} \tag{4.60}$$

Then the total light intensity of the reflected light in the MMF is

$$\begin{aligned} I &= \sum_{k=1}^{N} I_k \\ &= \sum_{k=1}^{N} \sum_{l=1}^{N} \sum_{m=1}^{N} p_l p_m^* \xi_{lk} \xi_{mk}^* + \sum_{k=1}^{N} \sum_{l=1}^{N} \sum_{m=1}^{N} p_l p_m^* \zeta_{lk} \zeta_{mk}^* \\ &\quad + \sum_{k=1}^{N} \sum_{l=1}^{N} \sum_{m=1}^{N} p_l p_m^* \xi_{lk} \zeta_{mk}^* \exp[j(4\pi d/\lambda + \pi)] + c.c. \end{aligned} \tag{4.61}$$

Using the fact that the phase of coefficients p_l is uncorrelated and assumed to be uniformly distributed in the range of $[-\pi,\ \pi]$, and further assuming that the mode number is large enough, similar to the analysis in Section 4.2.1, those terms with $l \neq m$ thus cancel each other out and Eq. (4.61) is then reduced to

$$\begin{aligned} I &= \sum_{k=1}^{N} \sum_{l=1}^{N} |p_l|^2 |\xi_{lk}|^2 + \sum_{k=1}^{N} \sum_{l=1}^{N} |p_l|^2 |\zeta_{lk}|^2 \\ &\quad + \sum_{k=1}^{N} \sum_{l=1}^{N} |p_l|^2 \xi_{lk} \zeta_{lk}^* \exp[j(4\pi d/\lambda + \pi)] + c.c. \end{aligned} \tag{4.62}$$

By defining

$$\eta_{R_1} = \sum_{k=1}^{N} |p_i|^2 \left(\sum_{i=1}^{N} |\xi_{ik}|^2 \right), \tag{4.63}$$

$$\eta_{R_2} = \sum_{k=1}^{N} |p_i|^2 \left(\sum_{i=1}^{N} |\zeta_{ik}|^2 \right), \tag{4.64}$$

and

$$\eta_i = \sum_{i=1}^{N} \xi_{ik}^* \zeta_{ik} = |\eta_i| \exp(j\theta_i), \tag{4.65}$$

Eq. (4.62) is simplified to

$$\begin{aligned} I &= \eta_{R_1} + \eta_{R_2} + \\ &\quad \sum_{i=1}^{N} |p_i|^2 \eta_i^* \exp[j(4\pi d/\lambda + \pi)] + c.c. \\ &= \eta_{R_1} + \eta_{R_2} + 2\sum_{i=1}^{N} |p_i|^2 |\eta_i| \cos(4\pi d/\lambda + \pi - \theta_i). \end{aligned} \tag{4.66}$$

Eq. (4.66) can be further simplified by defining

$$\eta_{eff} = |\eta_{eff}| \exp(j\theta_{eff}), \tag{4.67}$$

which reduces Eq. (4.66) to

$$I \propto 1 + \frac{2}{\eta_{R_1} + \eta_{R_2}} |\eta_{eff}| \cos(4\pi d/\lambda + \pi - \theta_{eff}). \tag{4.68}$$

Note that η_{R_1} and η_{R_2} are actually the light coupling losses between the MMF and its mirror image fiber with respect to surfaces R_1 and R_2, respectively. The result of Eq. (4.66) is similar to that of Eq. (4.26) which is the case where the fiber end-face is used as one of the reflection surfaces except that the calculation of η_i in Eq. (4.66) is much more complicated and yet more general. Provided the mode profile of each mode supported by the MMF is known, the coupling coefficients ξ_{ik} and ζ_{ik} can be calculated following the same procedure as shown in Section 4.2.3 and then η_{R_1}, η_{R_2}, and η_i can be obtained through Eqs. (4.63−4.65). With the knowledge of the mode power distribution ($|p_i|^2$) of the MMF, the spectral fringes are then obtained by either of Eqs. (4.66) and (4.68).

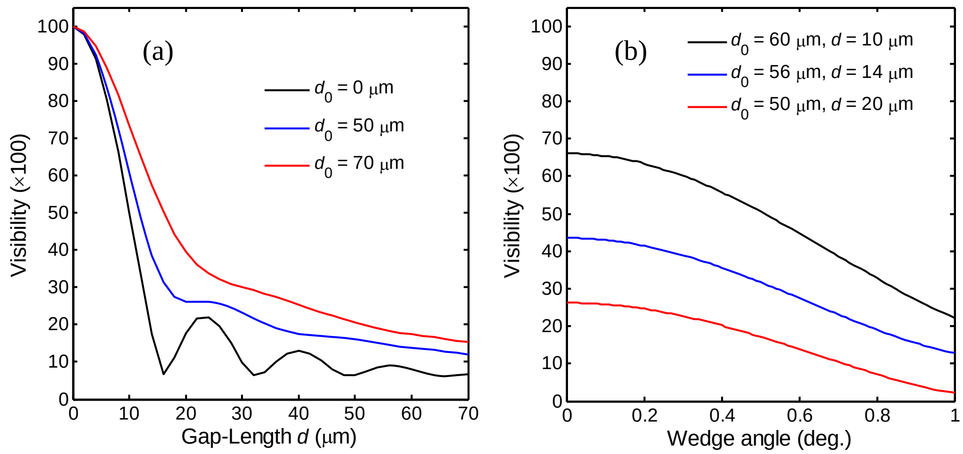

Figure 4.21: Visibility changes as a function of gap-length, (a); and visibility changes as a function of the sensing cavity wedge angle, (b).

4.9.2 Visibility analysis

The visibility, V_b, of the spectral fringes from a MMF-EFPI sensor is readily obtained from Eq. (4.68), which is given by

$$V_b = \frac{2}{\eta_{R_1} + \eta_{R_2}} |\eta_{eff}|. \tag{4.69}$$

As an example, the MMF used here is Fiber 2 in Table 4.1. We analyze the fringe visibility with respect to d_0 which is the distance between the lead-in/out MMF end-face and the FP sensing interferometer. Figure 4.21(a) shows the visibility changes as a function of gap-length d when the MMF is placed at different distances of $d_0 = 0$, 50, and 70 μm to the FP cavity. It is assumed that the two surfaces of the FP cavity are perfectly parallel to each other. The $d_0 = 0$ curve reduces to the case where the MMF end-face is used as one of the reflection surfaces of the FP cavity. It is clear that by placing the MMF at a distance to the FP cavity, the visibility is slightly improved and the sensitivity to the gap-length is reduced. For example, the $d_0 = 0$ curve reduces to its first minimum of less than 10% at gap-length $d \approx 16$ μm, while the visibilty still remains larger than 50% at the same gap-length if the MMF is placed 70 μm away from the FP cavity.

For the case that the FP cavity is not perfectly parallel, Figure 4.21(b) plots the visibility change as a function of the wedge angle between the two FP reflection surfaces. Compared to the result $d_0 = 0$ for the same fiber which conforms to the result shown in Figure (4.10) (blue curve), the visibility sensitivity to wedge angle is also slightly reduced.

Note that though the fringe visibility is improved by the distance between the FP cavity and the MMF that illuminates the cavity, the total power output from the MMF is also reduced due to the increased power coupling loss of the reflected light from the FP cavity to the lead-in/out MMF. However, it might still be advantageous in some cases where the light power is not a concern while the desirable visibility is difficult to achieve. A good example of such a case is a sapphire diaphragm illuminated by a sapphire fiber for extremely high temperature measurement, in which the thickness of the diaphragm is at least tens of micrometer and optical thickness is almost double the thickness because of the high refractive index of the sapphire.

4.10 Experimental validation of MMF-EFPI theory

To validate the theory and the analysis, the fringe visibility as a function of the wedge angle was measured to compare with the theoretical results. The experimental setup is shown in Figure 4.22(a).

To maximally excite the modes of the MMF, the light from a fiber optic light system (Model: MKII, Nikon, Inc.) was directly coupled into one meter long SI-MMF with a core diameter of 105 μm and a cladding diameter of 125 μm. A 3-dB SI-MMF coupler was used to separate the input and output light from the EFPI. The core and cladding diameters of the fiber used for the coupler were 100 μm and 140 μm respectively. Another one meter long 105/125 μm SI-MMF was used to transmit the input light to and output light from the interferometer. The detail of the interferometer is shown in Figure 4.22(b). To ensure that the two reflection surfaces are flat, instead of using a cleaved fiber end as the reflection surface, a 50 μm thick optically flat fused silica substrate was attached to the fiber end. Thus the side S_1 of the substrate formed one reflection surface of the EFPI. The other reflection surface was formed by the side S_2 of a 170 μm thick optically flat fused silica substrate, which is mounted onto a 5-dimensional positioner to allow the adjustment of the wedge angle $\delta\theta$. Index matching gel was applied to the fiber end and the sides of the diaphragms where reflections are undesirable. An optical spectrum analyzer (OSA) (Model: AQ-6315A, Ando Electric Co., Ltd) was used to measure the interference fringes from the EPFI and monitor the gap length d. The resolution of the OSA was set to 2 nm during the measurement. The wedge angle was changed from $-0.3°$ to $+0.5°$, and the gap length was maintained 16 μm during the measurement, which was achieved by maintaining the number of fringes present in the 250 nm (1425-1575 nm) wavelength range of measurement during the experiment. The position of the positioner corresponding to zero wedge angle was set to the position where maximum fringe visibility occurs. Therefore the wedge angle could be accurately monitored with the help of a fixed Helium-Neon laser and a mirror attached onto the 5-dimensional positioner which reflects the red laser light onto a screen 1 meter away from the positioner. The wedge angle was calculated simply by formula $\delta\theta = L_p/L_0$, where L_p is the distance that the laser point on the screen moves form its position corresponding to the zero wedge angle and L_0 is the distance between the screen and the positioner.

The blue line in Figure 4.23(a) shows the light spectral fringes output from the lead-

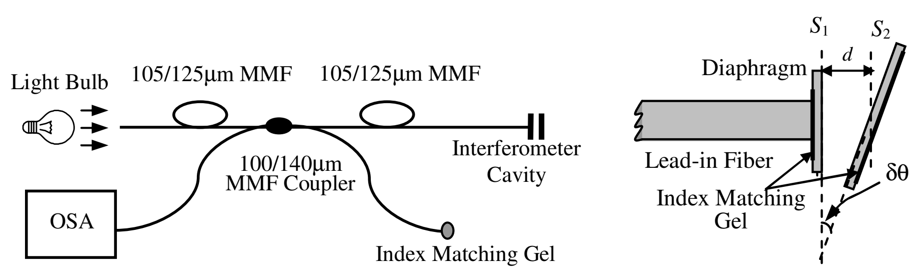

(a) (b)

Figure 4.22: Experimental setup to measure the fringe visibility as a function of wedge angle (a), and details of FP interferometer (b).

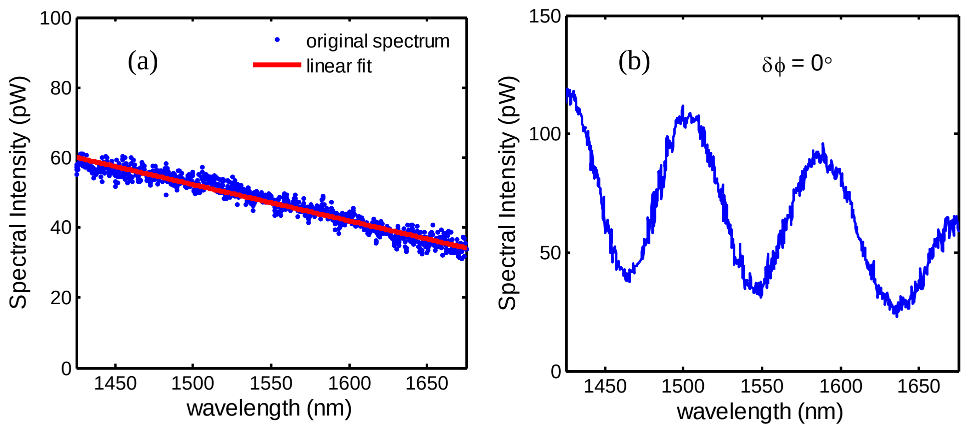

Figure 4.23: Original spectrum output from lead-in fiber and its least square linear fit (a); and a typical spectral fringe pattern obtained by the OSA (b).

in/out fiber and the red line is its LSE linear fitting, which was used to normalize the spectral fringes obtained by the OSA. Figure 4.23(b) shows a typical fringe pattern that the OSA measured before normalization. Figure 4.24 shows the normalized spectral fringes at wedge angles of 0°, 0.12°, 0.29°and 0.44°.

The normalization is necessary in the calculation of the fringe visibility in the frequency domain, which is given by $V_b = (I_{\lambda,max} - I_{\lambda,min})/(I_{\lambda,max} + I_{\lambda,min})$, where $I_{\lambda,max}$ and $I_{\lambda,max}$ are the maximum and minimum spectral intensities of the normalized spectral fringes. From Figure 4.24, the reduction of the fringe visibility due to the wedge angle increase is evident, and the fringe pattern is barely visible when the wedge angle is as small as 0.44°. Since the fiber parameters are unknown, the mode profiles in the MMF and consequently the absolute value of fringe visibility are difficult to predict. However, as shown in Section 4.9, when a SI-MMF is used for the MMF-EFPI sensor, the drop rate of the fringe visibility as the wedge angle increases is mainly determined by the core size of the MMF. Therefore it is more meaningful to compare the experimental and theoretical results of the percentage change instead of the absolute values of the fringe visibility as a function of the wedge angle. The comparison is shown in Figure 4.25. The modal theory and the analysis of the MMF-EFPI sensors have been validated by the good agreement between the experimental and theoretical

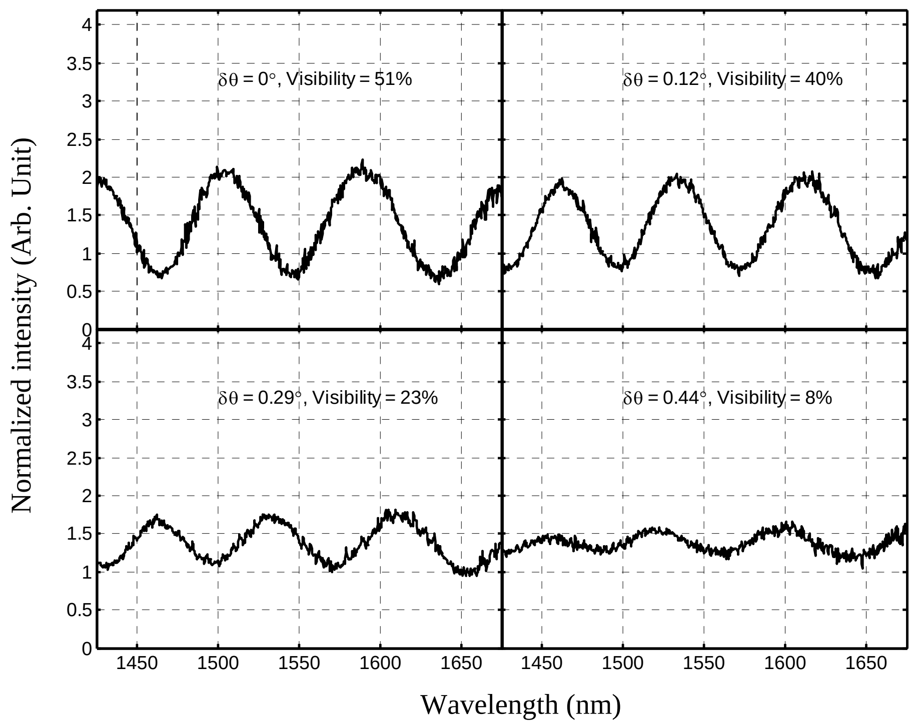

Figure 4.24: Normalized spectrum from the interferometer at different tilt angles.

results.

4.11 Conclusion

A modal theory is developed for low-finesse MMF-EFPI sensors. Comparing with geometric optics, the modal theory is more universal and accurate. Theoretically the modal theory can accurately predict the output spectral fringes for a MMF-EFPI sensor fabricated by any MMF provided the mode profiles and mode field distribution are known, and is literally free of any limitations imposed by geometric-optics-based theory.

Based on the modal theory, the fringe visibility variations as functions of the gap-length of the sensing FP interferometer and the wedge angles between the two reflection surfaces of the FP cavity are analyzed for different types of MMFs and different MPDs

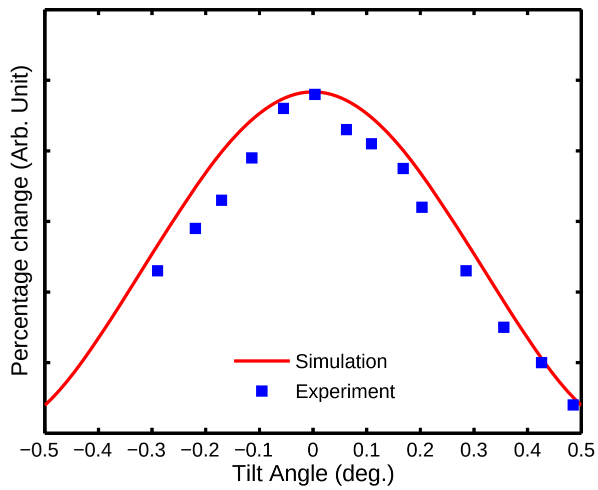

Figure 4.25: Comparison between the theoretical result and the experimental result on the percentage change of fringe visibility as a function of wedge angle.

of the MMFs. It is shown that, in general, the fringe visibility of MMF-EFPI sensors is much more sensitive to the gap-length and wedge angle variations than SMF-EFPI sensors. Therefore the fabrication process for the MMF-EFPI sensors could involve more complexity to ensure the fabrication accuracy owing to the great sensitivity of fringe visibility on sensor gap-length and imperfections.

We have revealed the mechanism that is responsible for the sensitivity to the gap-length and sensor imperfections of MMF-EFPI sensors from the view of modal coupling. The coupling-induced phase-shift variations owing to gap-length changes is responsible for the gap-length sensitivities; On the other hand, the phase coupling coefficient variations owing to wedge angles is responsible for the wedge angle sensitivity at small angles; while at large angles, both the coupling-induced phase-shift and amplitude coupling coefficient become responsible.

It is possible to reduce the visibility sensitivities to gap-lengths and wedge angles in a MMF-EFPI sensor by selectively exciting those modes whose coupling-induced phase-shift and amplitude coupling coefficient are less sensitive to the gap-length and wedge angle variations.

We also reveal that the mode-lobe positions of the circularly non-symmetric modes in a MMF may have significant effect on the fringe visibility of a MMF-EFPI sensor with wedge angles, especially for MMFs with significant amount of power carried by $\mathrm{LP}_{1,m},\ (m = 1, 2, ...)$ modes.

Finally, we develop a more general mathematical description of the fringes from a FP cavity illuminated by a MMF at a distance to the sensing FP cavity. The fringe visibility of MMF-EFPI sensors with such a configuration is also analyzed. We have shown that by placing the MMF at distance instead of closely to the FP cavity, the fringe visibility can be improved. This technique could be useful in cases where FP thickness is difficult to reduce for a desired fringe visibility.

Chapter 5

Signal processing for white-light MMF-EFPI sensor systems

5.1 Motivation

As discussed in Chapter 4, the visibility performance of MMF-EFPI sensors is usually limited by their gap-length and sensor imperfections. This limited fringe visibility makes their white-light version more favorable in many applications because the signal demodulation for a white-light EFPI sensor system is much less sensitive to the fringe visibility than for an intensity-based EFPI sensor system in which the output SNR is proportional to the fringe visibility. Surprisingly, very few work has been done for the signal processing of white-light MMF-EFPI sensor systems. One might expect that the signal processing methods used in SMF-EFPI sensor systems can be directly carried over to the MMF-EFPI sensor systems. This is true for most of them such as the methods of Type 2 and Type 3 curve fitting, Fourier Transform, two-point interrogation, and wavelength-tracking. However, Type 1 curve-fitting method presented in Chapter 3, which has been successfully applied in SMF-EFPI sensors and proved to have large dynamic ranges and the best measurement resolution, in principle is not valid for white-light MMF-EFPI sensor systems because the required accurate predication of the coupling-induced phase-shift of the spectral fringe pattern output from a white-light MMF-EFPI sensor system is difficult, as the coupling-induced phase-shift could vary greatly for different fiber types. Even for a given type of fiber, the variation of mode power distribution (MFD) in the MMF that could be varied by changes of light launch conditions and fiber operation conditions can cause significant variations in the coupling-induced phase-shift. The method proposed by Qi [37] *et al.* is invalid either because the assumption of an arbitrary constant phase shift is not valid in MMF-EFPI sensor systems and the variation of the coupling-induced phase-shift caused by gap-length changes could be large enough to cause errors in the calculation of the fringe number K. In fact, a signal processing method for MMF-EFPI sensor systems that could simultaneously achieve a large dynamic range and an ultra-high measurement resolution is, if not impossible, extremely difficult to develop. Even for some of the methods that could be directly carried over to the MMF-EFPI sensor systems from SMF-EFPI sensor systems, their performance may vary significantly in practice owing to the MFD effect. In this Chapter, we take the fringe peak-tracking method as an example and analyze its performance in MMF-EFPI sensor systems.

The rest of the chapter is constructed by the following three parts: In Section 5.2, the MPD effect on the performance of the fringe peak-tracking method is theoretically analyzed. In Section 5.3, experiments are carried out to validate the MPD effect. Finally comments and conclusions are given in Section 5.5.

5.2 MPD effect in wavelength-tracking method

As we have known, the wavelength-tracking method uses the wavelength position of a particular fringe peak (or valley) to map the parameters being measured and is shown to have an ultra-high measurement resolution in a white-light SMF-EFPI sensor system [36]. Even though this method has a limited dynamic range and is not capable of absolute measurement, it is still widely used in SMF-EFPI sensors due to its advantages of signal processing simplicity and ultra-high measurement resolution. However, in this section, we show that the measurement resolution of this method might be significantly affected by MPD variations in the MMF when it is applied to a white-light MMF-EFPI sensor system.

The modal theory developed in Chapter 4 tells that the spectral fringes from a MMF-EFPI sensor can be described by a single cosine function of

$$I(d,\lambda) = 1 + \frac{2}{1+\eta_{R_2}}|\eta_{eff}|\cos(4\pi d/\lambda + \pi - \varphi_{eff}). \tag{5.1}$$

The wavelength positions of the fringe peaks are found by solving

$$4\pi d/\lambda_m + \pi - \varphi_{eff} = 2m\pi, \tag{5.2}$$

where λ_m is the wavelength position of the fringe peak and m is a positive integer number denoting the order number. The solution of Eq. (5.2) is given by

$$\lambda_m = [(2m-1)\pi + \varphi_{eff}]/4\pi d. \tag{5.3}$$

Suppose the wavelength-tracking method uses variations of the wavelength position of a fringe peak with a particular number of m to map the measurand-induced gap-length changes. Note that, from Eq. (4.28), besides the dependence on the coupling phase coefficients η_k, which are determined by the fiber parameters only, η_{eff} is also a function of the MPD of the MMF which is difficult to measure in practice. MPD could vary owning to many factors. The initial MPD in a MMF is determined by light launching conditions; The MPD could evolve as light propagates along the fiber simply because the intrinsic fiber loss is different for different modes; Light power coupling between different modes that changes the MPD could occur owing to fiber core size variations, fiber bending, fiber deformation and environmental perturbations [34][57]. Optical components that are necessary in a sensor system such as the fiber couplers and the fiber connectors, could also significantly modify the MPD as light propagates through them [58]. Any MPD variations during the measurement could cause measurement errors in the wavelength-tracking method because these variations could cause the changes of φ_{eff} in Eq. (5.3) which is erroneously translated into

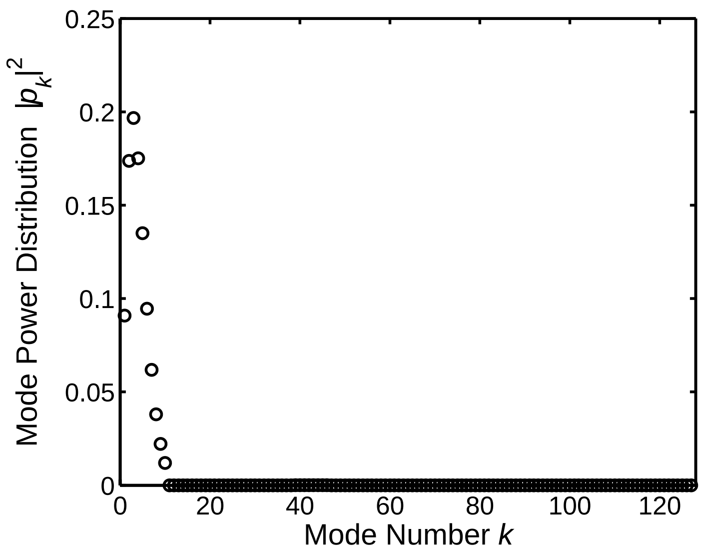

Figure 5.1: Mode power distribution of Fiber 1 in Table 4.1 illuminated by a SMF output.

the measurand-induced gap-length changes. In order to analyze the MPD effect on the wavelength-tracking method, the simulation uses a MMF-EFPI sensor that is constructed by Fiber 1 in Table 4.1 which supports $N = 127$ modes at central wavelength $\lambda_0 = 1550$. Three different MPDs are considered: In the first one, only one lowest order mode ($LP_{0,1}$) in the MMF is excited; in this case $|p_k|^2$ is equal to 1 for $k = 1$, and is equal to 0 for other k values. The second distribution corresponds to the case that the MMF is illuminated by a standard SMF. As discussed in Section 4.3.1, only $LP_{0,n}$ modes ($n = 1, 2, ..., 11$), which correspond to the lowest 11 modes ($k = 1, 2, ..., 11$) supported by the MMF, are excited and the $|p_k|^2$ values for mode number k are shown in Figure 5.1. The third MPD is the case that all modes supported by the MMF are equally excited; therefore $|p_k|^2 = 1/N$ for all k values.

Figure 5.2 shows the phase-shift φ_{eff} for the three MPDs as a function of the gap-length of the MMF-EFPI sensor. The phase-shift φ_{eff} increases as the gap-length d increases from the same starting point ($d = 0,\ \varphi_{eff} = 0$). However, the increasing rate varies greatly for different MPDs. The "$LP_{0,1}$ mode excited only" case gives the least phase-shift of 0.01π

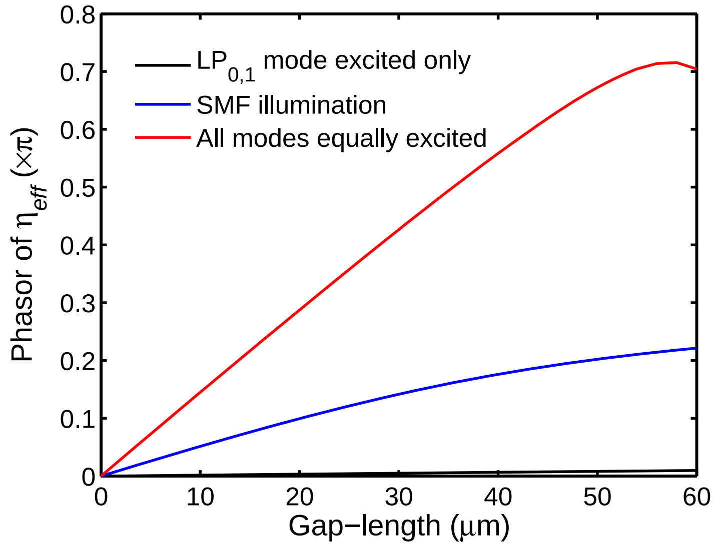

Figure 5.2: Phase-shift η_{eff} as a function of gap-lengths of a MMF-EFPI sensor with different mode power distributions.

for a gap-length change from 0 to 60 μm; while for the same gap-length range, the "SMF-illumination" case gives a phase-shift of 0.22π which corresponds to 0.11 fringe period; and the "all modes equally-excited" case gives a phase-shift of 0.7π corresponding to 0.35 fringe period.

The fringe pattern changes owing to different MPDs in the MMF of a MMF-EFPI sensor with gap-length $d = 30$ μm are shown in Figure 5.3. As expected, the dependence of fringe visibility on the MPD is evident with the single-mode excitation case having the best fringe visibility. More importantly, the wavelength positions of both fringe peaks and valleys vary significantly owing to the MPD differences. For example, the fringe peak located at wavelength $\lambda = 1519$ nm for the case of only $LP_{0,1}$ excited in the MMF would shift to $\lambda = 1522$ nm for the case of SMF-illumination, and to $\lambda = 1527$ nm for the case of all modes equally-excited. Any fringe peak position variations would be translated into the measurand-induced gap-length variations in the fringe peak-tracking signal processing method; Therefore the MPD variations might reduce measurement resolutions and/or cause measurement errors. In the worst case of our analysis, the mode power distribution is changed from "SMF output

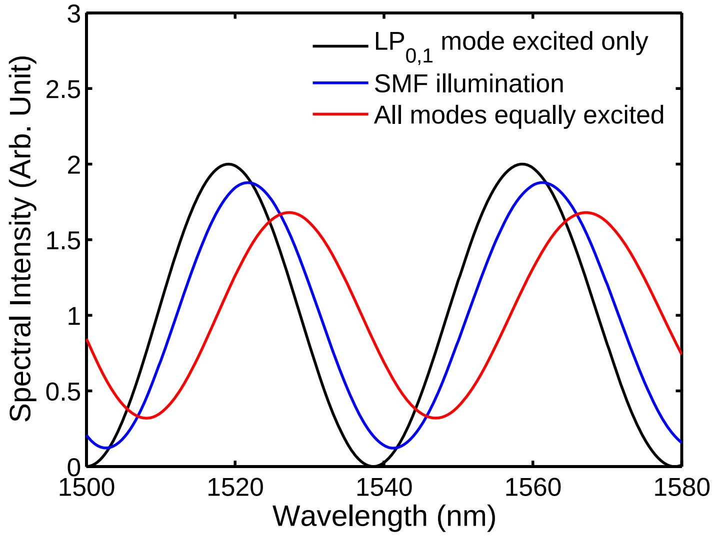

Figure 5.3: Fringe pattern changes owning to different mode power distributions for a MMF-EFPI sensor with gap-length $d = 30$ μm.

excitation" to "all modes equally excited", and the fringe peak position is shifted by 8 nm (1519-1527 nm). Considering that the spectral fringe pattern has a period of 40 nm and a central wavelength of 1550 nm, this phase-shift would cause an error of 310 nm of the gap-length measurement. Although this extreme conditions are not likely to occur in practice, MPD variations caused by unexpected fiber bendings or environmental perturbations in a practical white-light MMF-EFPI sensor system is of great concern in the performance of the wavelength-tracking signal processing method.

5.3 Experimental verification of MPD effect

An experiment was carried out to verify the dependence of fringes patterns on the MPD in MMF-EFPI sensors. The schematic of the experimental setup is shown in Figure 5.4(a). The FP cavity was formed by two surfaces of a 50 μm thickness fused silica diaphragm as shown in the inset of Figure 5.4(b). The inherent parallelism between the two surfaces ensured the best achievable fringe visibility. The diaphragm was closely attached to the MMF end which

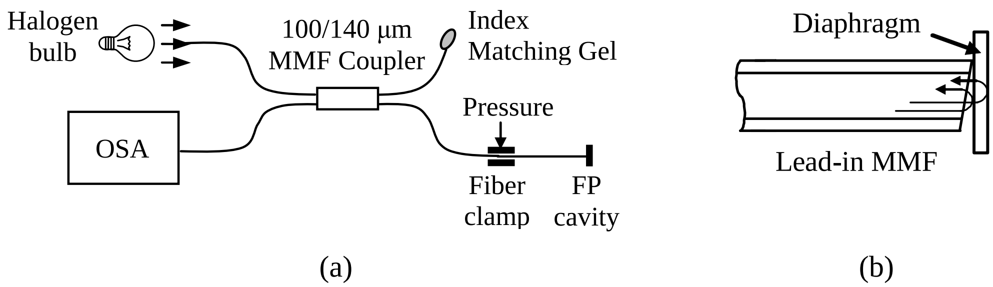

Figure 5.4: Experimental setup to verify the MPD effect on fringe patterns of a white-light MMF-EFPI sensor system,(a); and the detail of the FP cavity, (b).

was cleaved to an angle of around 2° to eliminate the interferences between the fiber end and the diaphragm surfaces. Graded-index multimode pigtail fibers from the ports of the coupler were used as lead-in/out MMF and fibers transmitting light to and from the FP cavity. The pigtail fibers were approximately 1 meter long each and have core and cladding diameters of 100 and 140 μm, respectively. A Halogen bulb was used as a large-area incoherent source to directly launch the light into the fiber. Since the coherent area of the Halogen bulb is much larger than the core size of the fiber, it is expected that all modes supported by the fiber were equally excited [59]. To generate different MPDs in the fiber, a fiber clamp was placed on the lead-in/out fiber to introduce lateral load on a 1 cm length of the fiber. It is known that the lateral pressure in the fiber causes greater loss to higher order modes than to lower order modes [60]. The overall effect of the lateral pressure is to force the MPD toward equilibrium where most of the light power is carried by lower order modes. We also observed that when pressure was applied, slight fiber bending was introduced which might cause MPD variations as well through mode-coupling and mode-mixing. An optical spectrum analyzer (OSA) was used to record the interferometric fringes from the FP cavity.

Figure 5.5 shows the spectrum of the light that illuminated the diaphragm which was measured directly at the output of the lead-in/out fiber. The spectrum is not uniform with the wavelength. A 10 order polynomial function is then used to fit the measured spectrum as a function of wavelength. The fitted curve was then used to normalize the obtained fringes. Figure 5.6 shows the fringe patterns recorded by the OSA for three fiber operation

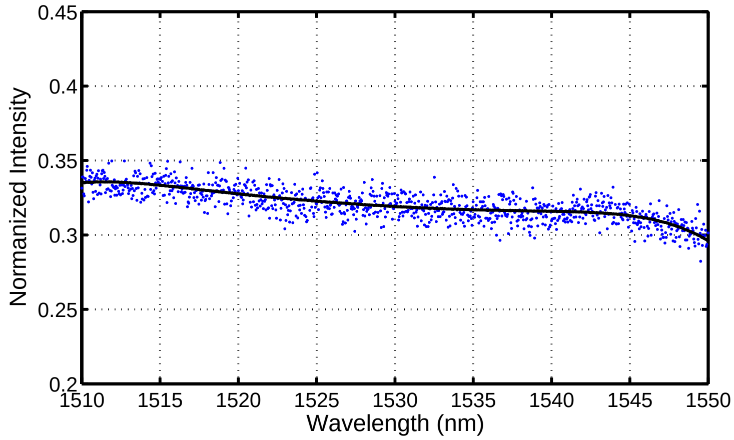

Figure 5.5: The spectrum of the light that illuminated the FP cavity (blue dot); and its 10 order polynomial fit (black line).

conditions. The positions of the valleys of each fringe are found using the same method in Section 3.4.4 and are marked by the vertical curves with the same color of the corresponding fringe curve. The black fringe is the case that the fiber was undisturbed and therefore all modes in the fiber were equally excited. When a small pressure was applied, it is expected that the light power was distributed heavier on lower order modes so we observed the fringe (blue curve) shifted around 0.7 nm toward the shorter wavelength from the undisturbed case. As the pressure was increased and more percentage of light power was carried by lower order modes, the total shift toward shorter wavelength of the fringe (red curve) was around 1.3 nm with respect to the undisturbed case. Considering the period of the fringes is 15 nm, a wavelength shift of 1.3 nm is equivalent to a phase shift of 0.17π. And this phase shift would be erroneously translated into the gap-length changes of the FP cavity by signal demodulations such as the wavelength-tracking method. For example, a change of 63 nm in the FP cavity gap-length would yield the same phase-shift in this case.

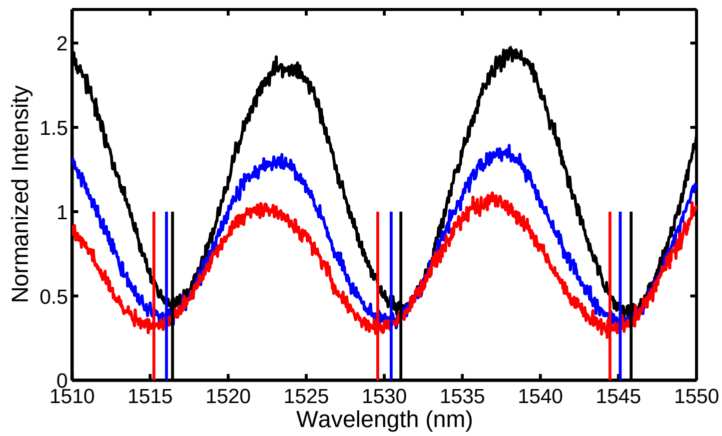

Figure 5.6: Fringe patterns obtained by the OSA. The black, blue, and red fringes correspond to fiber conditions of no perturbation, smaller and larger lateral pressure, respectively. The wavelength positions of the fringes valleys are marked by the vertical lines of corresponding colors.

5.4 Mode-mixing effect

It has been shown in Section 4.8 that the mode-mixing in a MMF-EFPI sensor that occurs as the light reflected by Surface R_2 is coupled back to the lead-in/out MMF can cause random variations of the fringe visibility as the phase relationship between different modes is random. There is no surprise that this mode-mixing effect can also cause random changes in spectral fringe phases in a white-light MMF-EFPI sensor system.

Similar to the analysis in Section 4.8, it is assumed that Fiber 3 in Table 4.1 is the lead-in/out MMF of the sensor and all modes (in the sense of conventional modes) are equally excited in the MMF. The interference signal is thus given by Eq. (4.57). In order to calculate the spectral fringe phase variations, it is convenient to reduce Eq. (4.57) to a single cosine function of variable φ_0 which is defined by $\varphi_0 = 4\pi d/\lambda$. Let

$$\begin{aligned}\gamma &= |\gamma| \exp(j\theta_\gamma) \\ &= \sum_{k=1}^{N} \sum_{n=1}^{q(k)} \frac{1}{q(k)} |p_k||c_k| \exp[j(\theta_{k,n}{}' - \varphi_{k,n})] + \sum_{k=1}^{N} \eta_k |p_k|^2 \end{aligned} \tag{5.4}$$

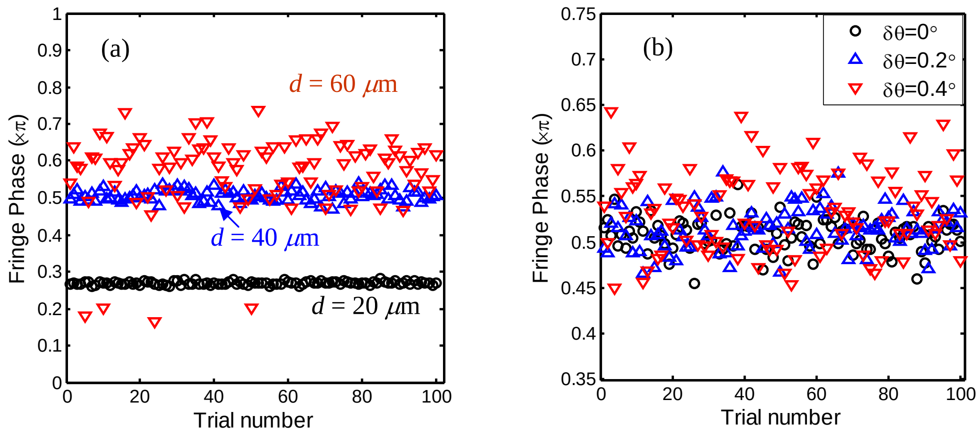

Figure 5.7: Phase variations owing to the mode-mixing effect of a MMF-EFPI sensor.

and after some straightforward algebra, Eq. (4.57) is reduced to

$$
\begin{aligned}
I &= \sum_{k=1}^{N}(|p_k|^2 + |\eta_k|^2|p_k|^2 + |c_k|^2) + 2\sum_{k=1}^{N}|\eta_k||p_k||c_k|\cos(\theta_k' - \theta_k - \varphi_k) \\
&\quad + |\gamma|\cos(\varphi_0 - \theta_\gamma).
\end{aligned} \tag{5.5}
$$

Therefore, the coupling-induced phase-shift can be obtained through Eq. (5.4) when the mode-mixing effect is considered. In the simulation, the random variables of $\theta_k' - \varphi_k$ are chosen the same way as in Section 4.8.

Figure 5.7(a) shows the phase variations (ϕ_γ) owing to the mode-mixing effect for different gap-lengths of a MMF-EFPI sensor constructed by Fiber 3. It is assumed that the sensor head has no wedge angle. When the gap-length increases, the mode-mixing effect becomes more significant and the phase variations become larger. For example, the standard deviations of the phase variations are 0.004π, 0.02π, and 0.07π for gap-lengths $d = 20$, 40, and 60 μm, respectively. Figure 5.7(b) is the comparison of the mode-mixing effect for different wedge angles of 0°, 0.2°, and 0.4°of the sensor and the corresponding standard deviation of the phase variations are 0.014π, 0.022π, and 0.044π, respectively. As expected, the standard deviations is larger when the mode-mixing is more significant at larger wedge-angles.

Similar to the MPD effect, the phase variations of the spectral fringes could cause measurement error in a signal processing method that uses the phase information of the spectral fringes, such as the wavelength-tracking method.

It should be noted that, as shown in Section 4.7, when the MMF is excited by a semi-coherent or incoherent light source whose spatial coherence length is much smaller than the core size of the MMF, the effective mode number could be much larger than the number of the modes that the MMF can support as each mode with different azimuthal angles can be excited independently. Therefore, we expect that the mode-mixing effect can be reduced by using a thermal light or a LED that have small spatial coherence lengths.

5.5 Conclusions

It is revealed that the phase of the fringe patterns from a white-light MMF-EFPI sensor system could be significantly changed by the variations of the MPD of light in the MMF. In practical applications of the MMF-EFPI sensors, the change of the MPD in the MMF, and consequently the phase variations of the fringe patterns, could occur due to various uncontrollable factors such as the ambient perturbations on the MMFs. An experiment was performed to verify the MPD effect predicted by the modal theory. In the experiment, by purposely applying lateral pressure on the MMF, a phase variation of 0.17π was observed in a FP cavity with essentially unchanged cavity length. Because of this uncertainty in the fringe phase, the Type 1 curve-fitting and wavelength-tracking methods, which show the best measurement resolutions among all the methods being discussed for a white-light SMF-EFPI sensors, can not be applied to MMF-EFPI sensors because the required assumption that the fringe phase is solely dependent on their gap-lengths is invalid for a MMF-EFPI sensor in which the MPD of the MMF is not stable and unpredictable.

One might speculate that by placing a mode scrambler in the MMF right before the sensor head would help to stabilize the the spectral fringe patterns as the MPD in the MMF is stabilized by the mode scrambler before the light is launched into the sensor head. However, the MPD effect is not alleviated because the spectral fringes is sensitive to MPD variations that occur anywhere along the fiber, not only to the local MPD at the sensor head.

Another effect that is unique to the MMF-EFPI sensors is the mode-mixing effect, which arises from the fact that different modes with random phase relationship could couple their power into the same modes in the lead-in/out MMF when they are reflected by the reflection surface that is placed at a distance to the end of the lead-in/out MMF. Simulations have shown that mode-mixing effect could cause random phase variations of the spectral fringes, and consequently, cause measurement error in wavelength-tracking method. The mode-mixing effect is closely related to the effective number of modes excited in the MMF and can be reduced by using a light source with small spatial coherence length.

As shown in Eq. (5.1), the period of the spectral fringes from a MMF-EFPI sensor is related to the gap-length the same way as in a SMF-EFPI sensor. Therefore, other methods including the Two-point interrogation, Fourier transform, and Type 2 and 3 curve-fitting methods, which do not require the knowledge of the fringe phase, are still applicable in MMF-EFPI sensor systems. We expect these methods would show similar performances in MMF-EFPI sensors as they do in SMF-EFPI sensors provided the SNR of the fringes is similar in both types of sensors. As shown in Section 3.5, the resolution of these methods are at least one order of magnitude worse than the Type 1 curve-fitting method and wavelength-Tracking method.

Chapter 6

Summary and future work

A detailed and systematic analysis on EFPI fiber optic sensors is performed in this dissertation to provide a better understanding of the fundamental principles of the sensor operations. More importantly, the analysis is useful in the design, fabrication, optimization, and application of EFPI fiber optic sensor systems. This chapter summarizes the main conclusions obtained from the research. Future research tasks that could lead to a more complete work are outlined.

6.1 Summary

In the analysis of SMF-EFPI sensors, the light transmitted in the fiber is approximated by a Gaussian beam and the obtained spectral transfer function of the sensors includes an extra phase shift due to the light coupling into the fiber end-face. This extra phase shift has not been addressed by previous researchers and is of great importance for high accuracy and high resolution signal processing of white-light SMF-EFPI systems. Fringe visibility degradation due to gap-length increase and unparallelism of the two reflection surfaces in a sensor, which is one of the most common sensor imperfections, is studied. The results indicate that the fringe visibility of a SMF-EFPI sensor is relatively insensitive to the gap-length change and sensor imperfections.

Based on the spectral fringe pattern predicated by the theory of SMF-EFPI sensors, a novel curve fitting signal processing method (Type 1 curve-fitting method) is presented for white-light SMF-EFPI sensor systems. Other spectral domain signal processing methods including the methods of wavelength-tracking, Type 2-3 curve fitting, Fourier transform, and two-point interrogation, are reviewed and systematically analyzed. An experiment was carried out to compare the performance of these signal processing methods. In the experiment, the spectral fringes of a SMF-EFPI sensor at different gap-lengths were measured and recorded by a spectrometer with high accuracy and high measurement resolution. The abovementioned signal processing methods were then implemented to the measured spectral fringes to obtain the gap-length. The results show that the methods of Type 1 curve-fitting and wavelength-tracking exhibit the highest measurement resolution of 0.2 nm, which is at least one order of magnitude higher than any of the other methods. However, the wavelength-tracking method is not capable of absolute measurement. Therefore, it is concluded that the novel Type 1 curve-fitting method has the most superior performance in terms of measurement resolution and capability of absolute measurement. Disadvantages of the Type 1 curve-fitting as well as the other two curve-fitting methods are their low-speed and stringent requirement on the SNR of the fringes.

Previous mathematical models for MMF-EFPI sensors are all based on geometric-optics; therefore their applications have many limitations. In this dissertation, a modal theory is developed that can be used for any MMFs in any situations and is more accurate. The mathematical description of the spectral fringes of MMF-EFPI sensors is obtained by the modal theory of the MMF. Effect on the fringe visibility of system parameters including the sensor head structure, the fiber parameters, and the mode power distribution (MPD) in the MMF of the MMF-EFPI sensors is analyzed. It is shown that the sensitivity of the fringe visibility to the gap-length is mainly determined by the number of modes that are present in the MMF, while the visibility sensitivity to the wedge angle is mainly related to the spatial spread of the light field in the MMF. It is also found that comparing to SMF-EFPI sensors, the MMF-EFPI sensors are generally much more sensitive to the gap-length changes and the unparallelism between the two reflection surfaces of the FP cavity, which is responsible for the fabrication difficulty we have experienced for many years. It is shown that, in some situations at which fringe visibility is important and difficult to achieve, a simple method of launching the light into the MMF-EFPI sensor system from the output of a SMF could be used to improve the fringe visibility and to ease the fabrication difficulties of MMF-EFPI sensors. Experiments was carried out to validate the theory. Fundamental mechanism that causes the fringe visibility degradation in MMF-EFPI sensors are revealed under the presented modal theory. The modal theory also predicates that the mode-lobe positions could have significant effect on the fringe visibility of a two-mode fiber EFPI sensors in which the two reflection surfaces of the FP cavity are not parallel with each other. Moreover, the modal theory for a more general MMF-EFPI sensor configuration, in which a FP cavity is illuminated by a MMF that is placed at a distance to the cavity, is presented. The fringe visibility performance of sensors with such a configuration is analyzed.

Signal processing methods that are well-understood in white-light SMF-EFPI sensor systems may exhibit new aspects when they are applied to white-light MMF-EFPI sensor systems. In this dissertation, it is revealed that the variations of the MPDs in the MMF could cause phase variations of the spectral fringes from a MMF-EFPI sensor and introduce measurement errors for a signal processing method in which the phase information is used. This MPD effect on the wavelength-tracking method in white-light MMF-EFPI sensors is theoretically analyzed. The fringe phases changes caused by MPD variations as predicted by the proposed modal theory were experimentally confirmed.

6.2 Contributions and publications

The major contributions of this dissertation include

- For the first time, the coupling-induced phase-shift is included in the mathematical description of the spectral fringes from SMF-EFPI sensors.
- A novel spectral-domain curve-fitting method is presented and experimentally verified for white-light SMF-EFPI sensors that achieves high accuracy, high resolution, large dynamic range, and absolute measurement at the same time. The measurement resolution is at least one order of magnitude higher than the currently absolute measurement signal processing methods.
- For the first time, a modal theory is developed for MMF-EFPI sensors. The modal theory is general and has no limitations that are present in a geometric-optics-based theory.
- For the first time, the mode-lobe position effect in MMF-EFPI sensors is theoretically predicted.
- For the first time, it is theoretically predicted and experimentally verified that the mode power distribution variations in the MMF of a MMF-EFPI sensor could significantly vary the spectral fringe patterns from the sensor.

The major publications by the author during the dissertation work include

1. **M. Han** and A. Wang, “Mode power distribution effect in white-light multimode fiber extrinsic Fabry-Perot interferometric sensor systems,” Optics Letters. **31**, 1202-1204 (2006).
2. **M. Han**, X. Wang, J. Xu, K. L. Cooper, and A. Wang, “Diaphragm-based extrinsic Fabry-Perot interferometric optical fiber sensor for acoustic wave detection under high background pressure,” Optical Engineering, **44**, 060506 (2005).

3. **M. Han** and A. Wang, "Analysis of a loss-compensated recirculating delayed self-heterodyne interferometer for laser linewidth measurement," Applied Physics B-Lasers & Optics, **81**, 53 (2005).

4. **M. Han** and A. Wang, "Exact analysis of low-finesse multimode fiber extrinsic Fabry-Perot interferometers," Applied Optics, **43**, 4659 (2004).

5. **M. Han**, Y. Zhang, F. Shen, G. R. Pickrell, and A. Wang, "Signal-processing algorithm for white-light optical fiber extrinsic Fabry-Perot interferometric sensors," Optics Letters, **29**, 1736 (2004).

6.3 Recommendations for future work

Based on the research that has been done in this dissertation, future work is recommended here. We believe the following work could provide deeper understanding of SMF-EFPI and MMF-EFPI sensors and accelerate the movement of these sensors toward wider applications.

1. **Experiment to verify the predicted couping-induced phase-shift in a SMF-EFPI sensor**

   In the analysis of SMF-EFPI sensors, we have predicted that the phasor of spectral fringe pattern includes a term of coupling induced phase-shift. This phase shift occurs when the reflected light from the second surface of the FP cavity is coupled to the lead-in fiber after propagating a distance in the free-space. However, there has been no experimental observation of this phase shift. Therefore it is of great interest to design and carry out an experiment to verify the existence of this term and measure the value of the phase-shift as a function of the free-space transmission distance.

2. **Study of mode power distributions in MMFs**

   We have shown that the MPD variations in a MMF can cause significant change of the spectral fringes in a white-light MMF-EFPI sensors. Furthermore, the spectral fringe from a MMF-EFPI sensor is a cosine function of the wave number only if the MPDs of light at all wavelengths of interest are consistent. However, this assumption has not been throughly checked. If the MPDs in the MMF were different for different wavelengths, the spectral fringes would be a cosine function with random phase which could distort the spectral fringes and jeopardize the effectiveness of many spectral domain signal processing methods for MMF-EFPI sensors that are based on the cosine spectral fringes.

3. **Performance study of spectral domain signal processing methods for white-light MMF-EFPI sensors**

   The available spectral processing methods for white-light MMF-EFPI sensors that are immune to MPD effect include Type 2-3 curve-fitting methods, two-point interrogation method, and Fourier transform method. However, the performance of these methods has not been studied yet. Therefore research should be performed to study and compare the measurement resolution, measurement accuracy, and robustness to ambient perturbations for all these methods. This is of great importance for the wide-spread use of the MMF-EFPI sensors.

4. **Effect of mode coupling and mode mixing in MMFs**

   It is inevitable that the coupling and mixing among different modes in a MMF occur as the light propagates along the fiber,especially when the light passes through some optical components such as a fiber coupler that are necessary to comprise the sensor system. For example, we consider the case that a SMF is spliced to an input port of a MMF coupler. We have observed that the spectrum from output port of the MMF coupler is significantly deformed from the spectrum measured at the SMF output. This can be only explained by the mode coupling and mixing occurring along the fiber and at the coupler. The effect of the mode coupling and mixing on the output of a MMF-EFPI sensor system needs to be studied in order to optimize its performance.

Bibliography

[1] B. Culshaw, “Optical Fiber Sensor Technologies: Opportunities andPerhapsPitfalls,” J. Lightwave Technol. **22,** 39-50 (2004).

[2] D. A. Jackson, “Monomode optical fibre interferometers for precision measurement,” J. Phys. E: Sci. Instrum. **18,** 981-1001 (1985)

[3] D. A. Jackson, “Recent progress in monomode fibre-optic sensors,” Meas. Sci. Technol. **5,** 621-638 (1994).

[4] D. W. Stowe, D. R. Moore, and R. G. Priest, “Polarization fading in fiber interferometric sensors,” IEEE J. Quantum Electron., **QE-18,** 626-665 (1982).

[5] A. D. Kersey, “A Review of recent developments in fiber optic sensor technology,” Opt. Fiber Technol. **2,** 291-317 (1996).

[6] C. E. Lee and H. F. Taylor, “Interferometric optic fibre sensors using internal mirrors,” Electron. Lett., **24,** 193-194 (1988).

[7] K. A. Murphy, “Extrinsic Fabry Perot optical fiber sensor,” in Proc. OFS- 8, Monterey, CA, 193 (1992).

[8] Y. Zhu, Z. Huang, F. Shen, and A. Wang, “Sapphire-fiber-based white-light interferometric sensor for high-temperature measurements,” Opt. Lett.**30,** 711-713 (2005).

[9] H. Xiao, J. Deng, Z. Wang, W. Huo, P. Zhang, M. Luo, G. R. Pickrell, R. G. May, and A Wang, “Fiber optic pressure sensor with self-compensation capability for harsh environment applications,” Opt. Eng. **44,** 54403-1-10 (2005).

[10] Y. Zhu and A. Wang, “Miniature fiber-optic pressure sensor,” IEEE Photon. Technol. Lett. **17,** 447-449 (2005).

[11] H. Xiao, J. Deng, G. R. Pickrell, R. G. May, and A. Wang, “Single-crystal sapphire fiber-based strain sensor for high-temperature applications,” J. of Lightwave Technol. **21,** 2276-2283 (2003)

[12] M. Schmidt, B. Werther, N. Fuerstenau, M. Matthias, and T. Melz, “Fiber-optic extrinsic Fabry-Perot interferometer strain sensor with ¡50 pm displacement resolution using three-wavelength digital phase demodulation,” Opt. Express **8,** 475-480 (2001).

[13] K. D. Oh, A. Wang, and R. O. Claus, “Fiber-optic extrinsic Fabry-Perot dc magnetic field sensor,” Opt. Lett. **29,** 2115-2117 (2004).

[14] W. Peng, G. R. Pickrell, Z. Huang, J. Xu, D. Kim, B. Qi, and A. Wang, “Self-Compensating Fiber Optic Flow Sensor System and its Field Applications,” Appl. Opt. **43,** 1752-1760 (2004).

[15] M. Han, X. Wang, J. Xu, K. Cooper, and A. Wang, ”A diaphragm-based extrinsic Fabry-Perot interferometric optical fiber sensor for acoustic wave detection under high background pressure,” Opt. Eng. **44,** 060506 (2005).

[16] Y. Zhang, H. Shibru, K. L. Cooper, and A. Wang, ”A miniature fiber optic Multi-cavity Fabry-Perot interferometric biosensor,” Opt. Lett. **30,** 1021-1023 (2005).

[17] W. Peng, G. R. Pickrell, F. Shen, and A. Wang,“Experimental Investigation of Optical Waveguide-based Multigas Sensing,”, IEEE Photon. Technol. Lett., **16,** 2317-2319 (2004).

[18] A. K. Murphy, M. F. Gunter, A. M. Vengsarker, and R. O. Claus, "Quadrature phase-shifted, extrinsic Fabry-Perot optical fiber sensors," Opt. Lett. **16,** 273-275 (1991).

[19] V. Arya, M. J. de Vries, K. A. Murphy, A. Wang, and R. O. Claus, "Exact analysis of the EFPI optical fiber sensor using Kirchhoffs diffraction formalism," Opt. Fiber Technol. **1,** 380-384 (1995).

[20] F. Pérennès, P. C. Beard, and T. N. Mills,"Analysis of a low-finesse Fabry-Perot sensing interferometer illuminated by a multimode optical fiber," Appl. Opt. **38,** 7026-7034 (1999).

[21] A. Wang, H. Xiao, J. Wang, Z. Wang, W. Zhao, and R. G. May, "Self-Calibrated Interferometric/Intensity-Based Optical Fiber Sensors," J. of Lightwave Technol. **19,** 1495-1501 (2001).

[22] C. Belleville, and G. Duplain, "White-light interferometric multimode fiber-optic strain sensor ," Opt. Lett. **18,** 78-80 (1993)

[23] T Liu, D Brooks, A Martin, R Badcock, B Ralph, and G F Fernandoy, "A multi-mode extrinsic FabryPerot interferometric strain sensor," Smart Mater. Struct. **6,** 464469 (1997).

[24] V. Bhatia, K. A. Murphy, R. O. Claus, T. A. Tran, and J. A Greene, "Recent developments in optical-fiber-based extrinsic Fabry-Perot interferometric strain sensing technology," Smart. Mater. Struct. **4,** 246-251 (1995).

[25] M. Born and E. Wolf, *Principles of optics*, 6th ed., (Pergamon Elmsford, NY, 1988).

[26] P. P. Banerjee and T. C. Poon, *Principles of applied optics*, (Irwin, IL, 1991)

[27] D. T. Neilson, "Tolerance of optical interconnections to misalignment," Appl. Opt. **38,** 2282-2290, (1999).

[28] E. Hecht, *Optics*, 2nd ed. (Addison-Wesley, Reading, Mass.,1987), pp. 364366.

[29] J. L. Santos, A. P. Leite, and D. A. Jackson, "Optical fiber sensing with a low-finesse Fabry-Perot cavity," Appl. Opt. **31,** 73617366 (1992).

[30] C. M. Miller, S. C. Mettler, and I. A. White, *Optical Fiber Splices and connectors: theory and methods*, (Marcel Dekker Inc., New York, 1986).

[31] G. Keiser, *Optical Fiber Communications*, (McGraw-Hill, Boston, MA, 2000).

[32] T. C. Poon, P. P. Banerjee, *Contemporary optical image processing with MATLAB*, (Elsevier Science Ltd., New York, 2001).

[33] A. Safaaii-Jazi, *Optical Waveguides*, Lecture Notes, ECE Department, Virginia Polytechnic Institute and State University, (2002)

[34] J. N. Kutz, J. A. Cox, and D. Smith, "Mode mixing and power diffusion in multimode optical fibers," J. Lightwave Technol. **16,** 1195-1202, (1998).

[35] W. Pulliam, P. Russler, R. Mlcak, K. Murphy, and C. Kozikowski, "Micromachined, SiC fiber optic pressure sensors for high temperature aerospace applications," SPIE Proc. **4202,** 21-30 (2000).

[36] V. Bhatia, M.B. Sen, K.A. Murphy, and R.O. Claus, "Wavelength-tracked white light interferometry for highly sensitive strain and temperature measurement," Electron. Lett. **32,** 247-248 (1996).

[37] B. Qi, G. R. Pickrell, J. Xu, P. Zhang, Y. Duan, W. Peng, Z. Huang, W. Huo, H. Xiao, R. G. May, and A. Wang, "Novel data processing techniques for dispersive white light interferometer," Opt. Eng. **42,** 3165-3171 (2003).

[38] J. Schwider and L. Zhou, "Dispersive interferometric profilometer," Opt. Lett. **19,** 995-997 (1994).

[39] D. Marcuse, "Microdeformation losses of single-mode fiber," Appl. Opt. **23,** 1082-1091 (1984).

[40] A. Bjarklev, "Microdeformation losses of single-mode fibers with step-index profiles," J. Lightwave Technol. **LT-4,** 341-346 (1986).

[41] J. Kuffel, T. McComb, and Malewski, "Comparative evaluation of computer methods for calculating the best fit to sinusoid to the high purity sine wave," IEEE. Trans. On Instrumentation and Measurement, **IM-36,** 418-422 (1987).

[42] T. R. McComb, J Kuffel, and B. C. Le Roux, "A comparative evaluation of some practical algorithms used in the effective bits test of waveform recorders," IEEE. Trans. On Instrumentation and Measurement, **38,** 37-42 (1989).

[43] *IEEE Standard for digitizing waveform recorders*, IEEE Standard 1057 (1994).

[44] D. Marcuse, "*Light Transmission Optics*", 2nd ed. (Van Nostrand Reinhold, New York, 1982), Chap. 11, p.466.

[45] T. Okoshi and K. Okamoto, "Analysis of Wave Propagation in Inhomogeneous Optical Fibers using a Variational Method," IEEE Trans. Microwave Theory Tech. **MTT-22,** 938-945 (1974).

[46] K. Okamoto and T. Okoshi, "Analysis of Wave Propagation in Optical Fibers Having Core with a-Power Refractive Index Distribution and Uniform Cladding," IEEE Trans. Microwave Theory Tech. **MTT-24,** 416-421 (1976).

[47] M. Geshiro, M. Matsuhara, and N. Kumagai, "Truncated Parabolic-Index Fiber with Minimum Mode Dispersion," IEEE Trans. Microwave Theory Tech. **MTT-26,** 115-119 (1978).

[48] K. Okamoto and T. Okoshi, "Vectorial Wave Analysis of Inhomogeneous Optical Fibers using Finite Element Method," IEEE Trans. Microwave Theory Tech. **MTT-26,** 109-114 (1978).

[49] M. Hasimoto, S. Nemoto, and T. Makimoto, “Analysis of Guided Waves Along the Cladded Optical Fiber: Parabolic-Index Core and Homogeneous Cladding,” **MTT-25,** 1-17 (1977).

[50] B. K. Garside, T. K. Lim, and J. P. Marton, “Propagation characteristics of parabolic-index fiber modes: linearly polarized approximation,” J. Opt. Soc. Am., **70,** 395-400 (1980).

[51] D. Donlagić and M. Zavrŝnik, “Fiber optic microbend sensor structure,” Opt. Lett. **22,** 837-839 (1997)

[52] D. Donlagić and B. Culshaw, “Microbend sensor structure for use in distributed and quasi-distributed sensor systems based on selective launching and filtering of the modes in graded index multimode fiber,” J. Lightwave Technol. **17,** 1856-1868 (1999)

[53] P. C. Beard and T. N. Mills, “A miniature optical fibre ultrasonic hydrophone using a Fabry Perot polymer film interferometer,” Electron. Lett. **33,** 801-803 (1997).

[54] A. J. Coleman, E. Draguioti, R. Tiptaf, N. Shotri, and J. E. Saunders, “Acoustic performance and clinical use of a fibreoptic hydrophone,” Ultrasound Med. Biol. **24,** 143-151 (1998).

[55] P. C. Beard and T. N. Mills, ”Extrinsic optical fiber ultrasound sensor with a thin polymer film as a low-finesse Fabry Perot interferometer,” Appl. Opt. **35,** 663-675 (1996).

[56] P. C. Beard, F. Pérennès, E. Draguioti, and T. N. Mills, “Optical fiber photoacoustic photothermal probe,” Opt. Lett. **23,** 1235-1237 (1998).

[57] D. Gloge, “Bending loss in multimode fibers with graded and ungraded core index,” Appl. Opt. **11,** 2506-2513 (1972).

[58] M. Ikeda, Y. Murakami, and K. Kitayama, “Mode scrambler for optical fibers,” Appl. Opt. **16,** 1045-1049 (1977).

[59] D. Marcuse, "Excitation of parabolic-index fibers with incoherent sources," Bell Syst. Tech. J. **54,** 1507-1530 (1975).

[60] S. Sumida, H. Murata, and Y. Katsuyama, "A new method of optical fiber loss measurement by the side-illumination technique," J. Lightwave Technol. **LT-2,** 642-646 (1984).

Vita

Ming Han was born in Shandong, China on July 6, 1975. He received his B.S. degree and M.S. degree in Electrical Engineering in 1998 and 2000, respectively, both from Tsinghua University, Beijing, China. From 1997 to 2000, he was a Research Assistant in the National Key Laboratory of Integrated Optoelectronics of China , where he worked on fiber optical communications and nonlinear fiber optics.

In 2000, Ming Han started his Ph.D. study in the Bradley Department of Electrical Engineering of Virginia Polytechnic Institute and State University (Virginia Tech). He was a Graduate Research Associate in the Center for Photonics Technology (CPT) at Virginia Tech, where he worked on numerous projects on fiber optic sensors, laser characterization, high speed spectrometers, and constancy test of physical constants. He has authored and co-authored more than 10 journal papers.

As of May 2006, Ming Han started a new position as a Research Associate at CPT.